Finite Element Modeling of the Mitral Valve and Mitral Valve Repair

Iain Baxter

A thesis submitted to the Faculty of Graduate and Postdoctoral Studies in partial fulfillment of the requirements for the degree of

MASTER OF APPLIED SCIENCE
in Mechanical Engineering

Ottawa-Carleton Institute for Mechanical and Aerospace Engineering
University of Ottawa
Ottawa, Canada

Abstract

As the most commonly diseased valve of the heart, the mitral valve has been the subject of extensive research for many years. Prior research has focused on the development of surgical repair techniques and mainly consists of in vivo clinical studies into the efficacy and long-term effects of different procedures. There is a need for a means of studying the mitral valve ex vivo, incorporating patient data and the effects of different repair techniques on the valve prior to surgery.

In this study, a method was developed for reconstructing the mitral valve from patient-specific data. Three-dimensional transthoracic and transesophageal echocardiography (3D-TTE and 3D-TEE) were used to obtain ultrasound images from a normal subject and a patient with mitral valve regurgitation. Geometric information was extracted from the images defining the primary structures of the mitral valve and a special program in MATLAB was created to automatically construct a finite element model of a valve. A dynamic finite element analysis solver, LS-DYNA 971, was used to simulate the dynamics of the valves and the non-linear, anisotropic behaviour of biological tissue. The two models were successful in simulating the dynamics of the mitral valve, with the subject model displaying normal function and the patient model showing the dysfunction displayed in the ultrasound images.

A method was then developed to modify the original patient model, in a way that maintains its patient-specific nature, to model mitral valve repair. Four mitral valve

repair techniques were simulated using the patient model: the annuloplasty ring, the double-orifice Alfieri stitch, the paracommissural Alfieri stitch, and the quadrangular resection. The former was coupled with the other three techniques, as is standard protocol in mitral valve repair. The effects of these techniques on the mitral valve were successfully determined, with varying degrees of improvement in valve function.

Acknowledgements

I would like to express my gratitude to those who made this thesis possible. I am very thankful to my supervisor, Dr. Michel Labrosse, for his expertise and guidance in completing this work, as well as for the opportunities it has provided. I would also like to thank Drs. Thierry Mesana, Mark Hynes, and Kathryn Ascah, of the University of Ottawa Heart Institute, for their collaboration in obtaining the necessary clinical data.

I am eternally grateful to my parents, Dr. Alan Baxter and Corinne Baxter, for being so supportive and encouraging throughout my studies. Thanks also go to my inspirational and supportive girlfriend, Rachel Clewley, and to my friends and colleagues, who have all helped me along the way.

Table of Contents

List of Figures

List of Tables

Chapter 1

Introduction

1 Introduction

The mitral valve is an important and complex component of the heart; it is also the most commonly diseased valve of the heart. In this chapter, an introduction to the anatomy and physiology of the heart and the mitral valve is provided for a better understanding of the function of the valve. Common mitral valve diseases are reviewed, as well as several methods for the surgical repair of diseased mitral valves. The potential of the present work, the modeling and dynamic analysis of the mitral valve, as an aid in cardiac surgery is discussed, in addition to the objectives of this study.

1.1 Anatomy & Physiology of the Heart and the Mitral Valve

The heart consists of four chambers: the right and left ventricles and the right and left atria, as shown in Figure 1. Blood flow through the heart is regulated by four valves: the mitral, aortic, tricuspid, and pulmonary valves. The cardiac cycle consists of diastole, in which the heart relaxes, and systole, the contraction of the heart. In diastole, blood flows from the body through the superior and inferior vena cava, passes through the right atrium and the open tricuspid valve into the right ventricle. At the same time, blood flows into the left atrium from the pulmonary vein, passing through the open mitral valve and filling the left ventricle. During systole, the ventricles contract, causing the tricuspid and mitral valves to close and the pulmonary and aortic valves to open. Blood is pumped through the open valves and out of the heart.

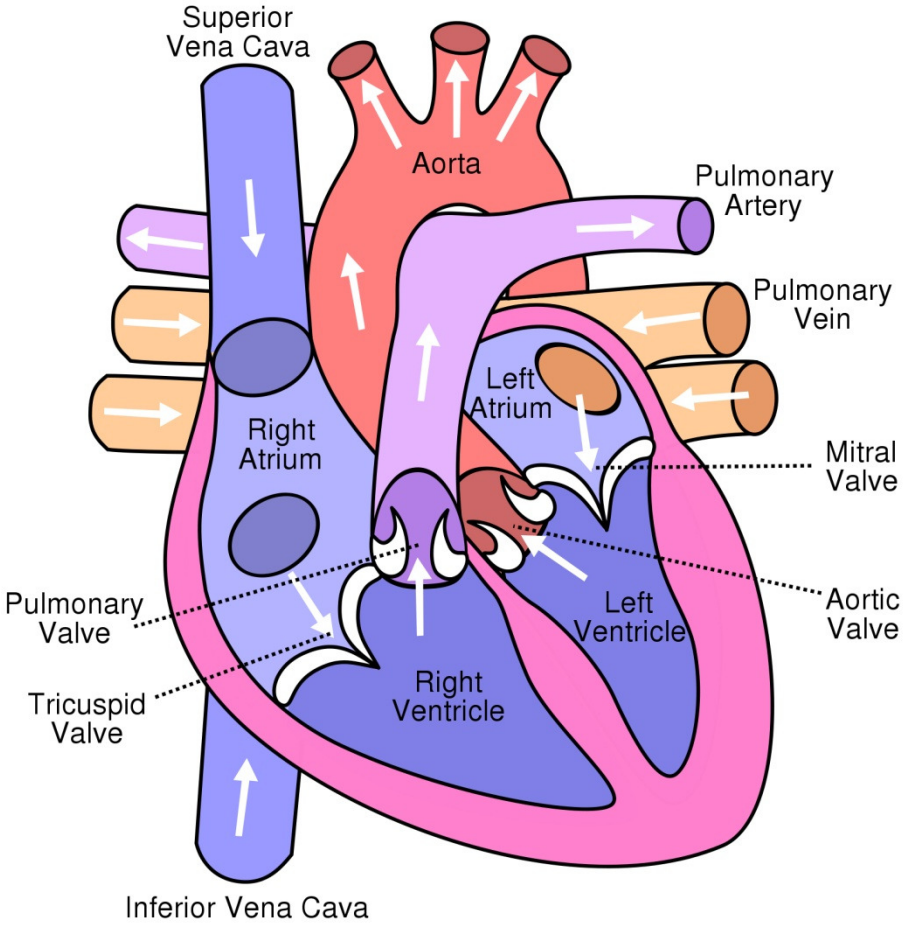

Figure 1 - The Heart [1]

The mitral valve consists of two thin, asymmetrical leaflets (anterior and posterior leaflets) attached to the left ventricle at the annulus. The anterior leaflet is typically larger in area than the posterior leaflet. The leaflets are suspended by the chordae tendinae, which are string-like structures. The chordae tendinae attach to the free margin (moving edges) of the leaflets and are anchored to two papillary muscle heads originating from the bottom and sides of the left ventricle (Figure 2).

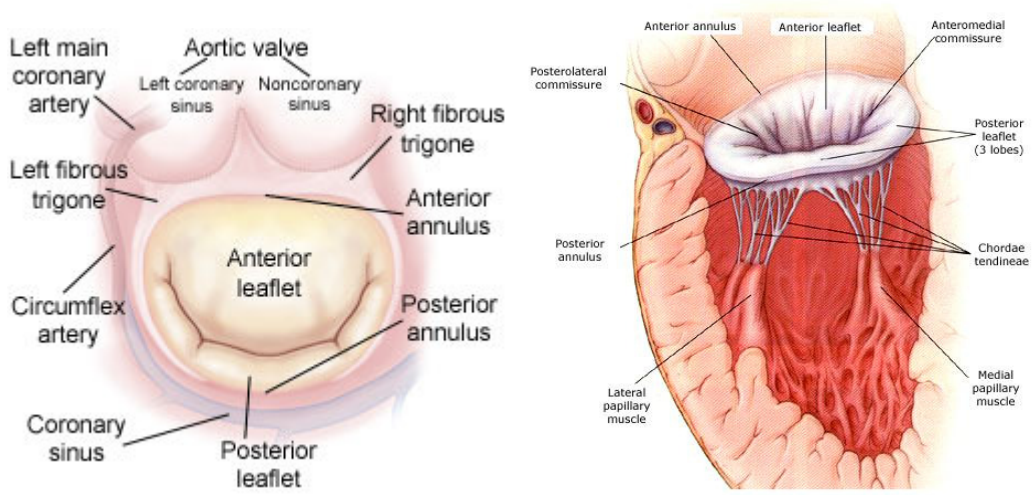

Figure 2 – Top view (left) and side view (right) of the mitral valve, showing its anatomical structure [2].

The function of the mitral valve is to let blood into the left ventricle during diastole and to prevent backflow of blood into the left atrium during systole (Figure 3). When the ventricles contract, the mitral valve closes, the annulus dilates, and the chordae tendinae prevent the leaflets from entering the left atrium. The chordae support the leaflets under high pressure, allowing the valve to form a seal during systole. Prolapse of the valve occurs if the leaflets bulge into the atrium as the valve closes.

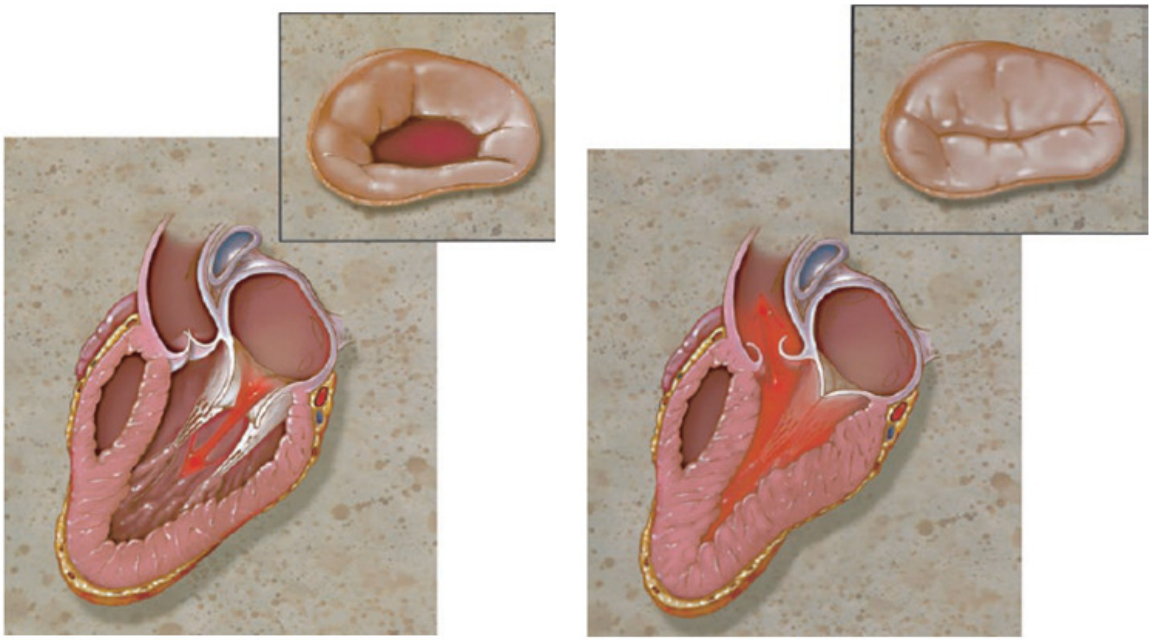

Figure 3 – The mitral valve in diastole (left) and systole (right) [3].

1.2 Mitral Valve Disease and Surgery

A disease of the mitral valve is any condition which results in diminished valve function, typically from elongation or rupture of the chordae, dilation of the annulus, and/or leaflet dysfunction. The two main classifications of mitral valve disease are stenosis and regurgitation, both of which are caused by a wide variety of conditions. There are several medical interventions which may be utilized for treatment, such as valve replacement, valve repair, and the use of medications. In mitral valve replacement the valve is removed and replaced with a mechanical or bioprosthetic valve. Mitral valve repair is a more desirable treatment because it has a much lower risk of mortality and of reoperation, although it is much more complex and less prevalent than mitral valve replacement [3]. There are several valve repair techniques, of which four are investigated in this study: annuloplasty rings, double-orifice and paracommissural Alfieri stitches, and quadrangular resection. In this section, an overview of mitral valve diseases and surgical repair techniques is presented.

1.2.1 Mitral Valve Stenosis

Stenosis of the mitral valve is a narrowing or obstruction of the valve orifice [4]. There are several causes of stenosis, such as rheumatic fever, annular or leaflet calcification, and congenital valve deformities. Rheumatic fever after an untreated bacterial infection can cause a thickening of the annulus and leaflets, as shown in Figure 4, which leads to obstruction of blood flow through the valve [4]. A build-up of calcium along the annulus or on the leaflets can also lead to a narrowing of the orifice, as shown in Figure 4. Congenital defects can obstruct blood flow, such as having only one papillary muscle

instead of two, which can cause thickening of the chordae and obstructs blood flow below the orifice area of the valve [4]. Mitral valve stenosis is relatively uncommon, except in developing countries with limited access to antibiotics [4].

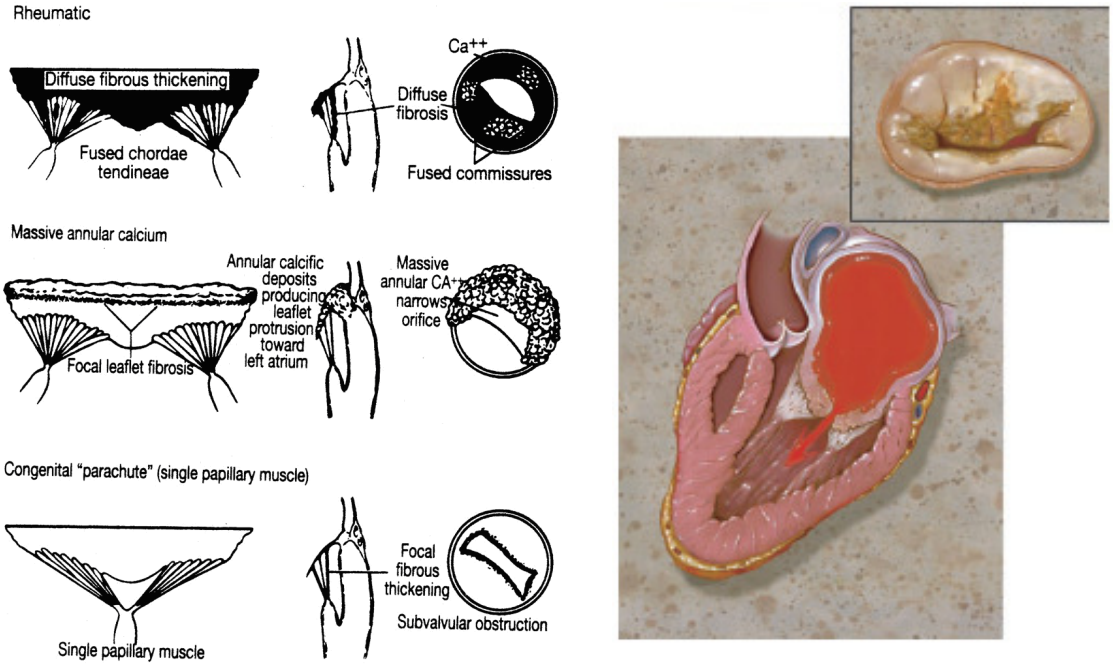

Figure 4 – (a) Examples of Mitral Valve Stenosis [4]; (b) Rheumatic Mitral Valve Stenosis [3].

1.2.2 Mitral Valve Regurgitation

Mitral valve regurgitation is a disease in which the valve leaks: blood flows back through the valve into the left atrium during systole [3]. It typically occurs due to a dysfunction of the valve geometry, papillary muscle alignment, or the chordae tendinae [4]. This dysfunction prevents coaptation of the leaflets, allowing backwards blood flow (Figure 5-a). The most common cause is myxomatous degeneration, also known as floppy mitral valve or valve prolapse (Figure 5-b), and is characterized by increased leaflet area, annular dilation, and/or chordae rupture [4]. Some other causes are ischemic heart disease, rheumatic fever, annular calcification, and congenital defects [4]. These

degenerative diseases may result from one or more physical changes to the mitral valve complex, namely leaflet retraction, annular dilatation, chordal abnormalities, and papillary muscle dysfunction, resulting in regurgitation [4].

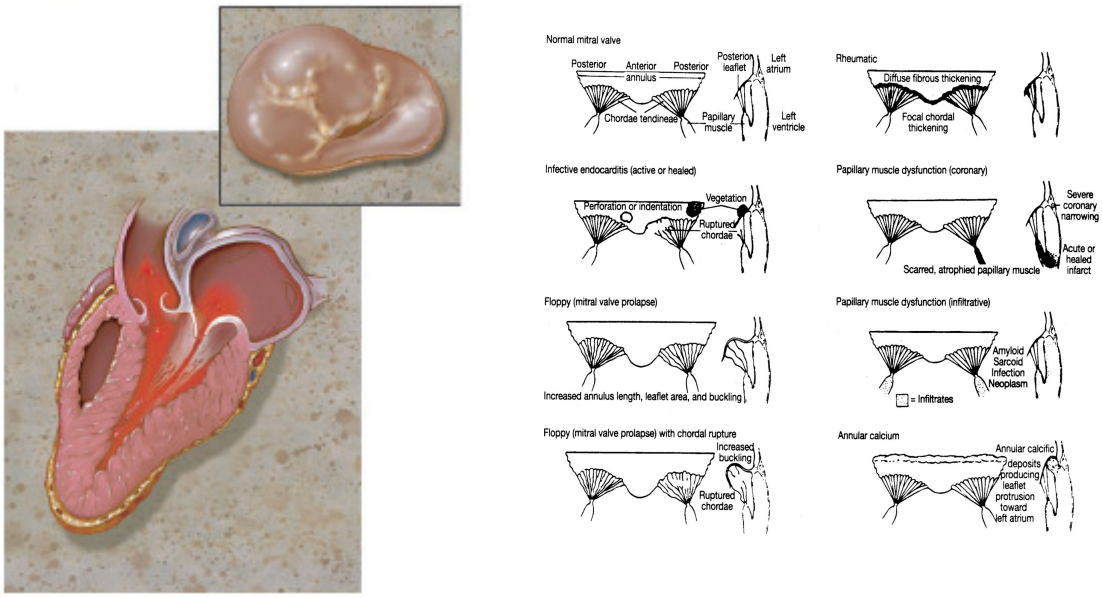

(a) **(b)**

Figure 5 – (a) Mitral Valve Regurgitation [3]; (b) Floppy Mitral Valve [4].

1.2.3 Mitral Valve Repair Techniques

Many surgical repair techniques have been developed for the treatment of degenerative mitral valve disease. Repair is possible in up to 90% of cases, provided the surgical skills are available and the valve is not too dysfunctional [5]. Depending on the specific valve dysfunction, a surgeon may shorten the annulus length, replace or relocate chordae tendinae, narrow the valve orifice, reposition a papillary muscle, or fix the annulus in position to prevent dilation. The repair techniques examined in this section are annuloplasty rings, double-orifice and paracommissural Alfieri stitches, and quadrangular resection, because they are among the most often used.

1.2.3.1 Annuloplasty Rings

An annuloplasty ring is a prosthetic ring in the generic shape of the mitral valve annulus which is sutured to the original annulus, preventing it from dilating during the cardiac cycle (Figure 6). A ring is typically installed in combination with a repair technique, such as those discussed previously. The ring is designed to reduce regurgitation by restoring normal annulus shape and prevent future dilatation of the annulus [6]. Also, it reduces the tension on sutures used in leaflet and chordal repairs [6]. The use of an annuloplasty ring has been shown to improve long term survival and reduce the need for reoperation [6]. There are many different ring designs, some form a full ring while others only form part of the annulus shape. Since the size of the mitral valve varies between patients, the rings come in multiple sizes and must be sized to fit the valve by the surgeon during the operation.

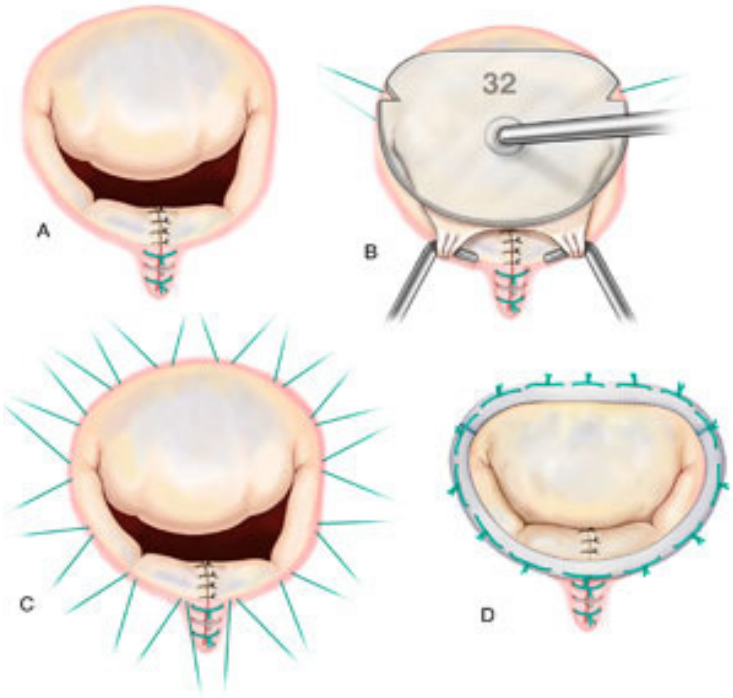

Figure 6 – An annuloplasty ring being sutured to the annulus of the mitral valve [7].

1.2.3.2 Alfieri Stitch

The Alfieri stitch involves suturing the free margin of leaflets together. There are two types of Alfieri stitch repairs shown in Figure 7: double-orifice stitch and paracommissural stitch. The double-orifice stitch involves suturing the leaflets in such a way as to create two orifices for blood to flow through [8]. In the paracommissural stitch the leaflets are sutured at the commissure, where the two leaflets join together, reducing the orifice area of the valve [8]. These techniques are used to treat regurgitation, typically due to prolapse, wherein the prolapsed leaflet is fixed to the other leaflet [8].

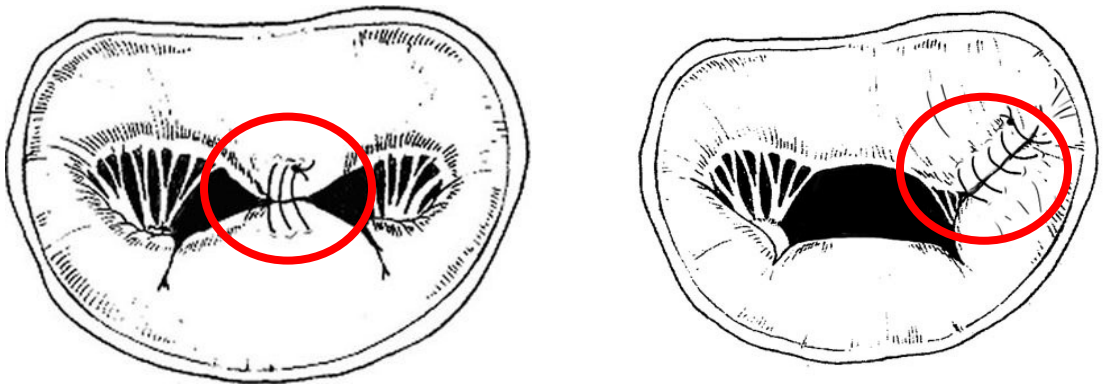

Double-orifice Stitch **Paracommissural Stitch**

Figure 7 - Double-orifice and Paracommissural Alfieri Stitches [8].

1.2.3.3 Quadrangular Resection

The quadrangular resection is the most common repair technique performed, used to eliminate a ruptured chordae tendinae or to repair prolapse of the posterior leaflet [9]. In doing so, it also shortens the annulus and decreases the leaflet area. As shown in Figure 8, the technique is performed by first removing the ruptured chordae along with a rectangular section of leaflet, at the location of the ruptured chordae. The annulus and

leaflet edges at the removed section are then sutured together and a rigid ring (annuloplasty ring) is sutured to the annulus.

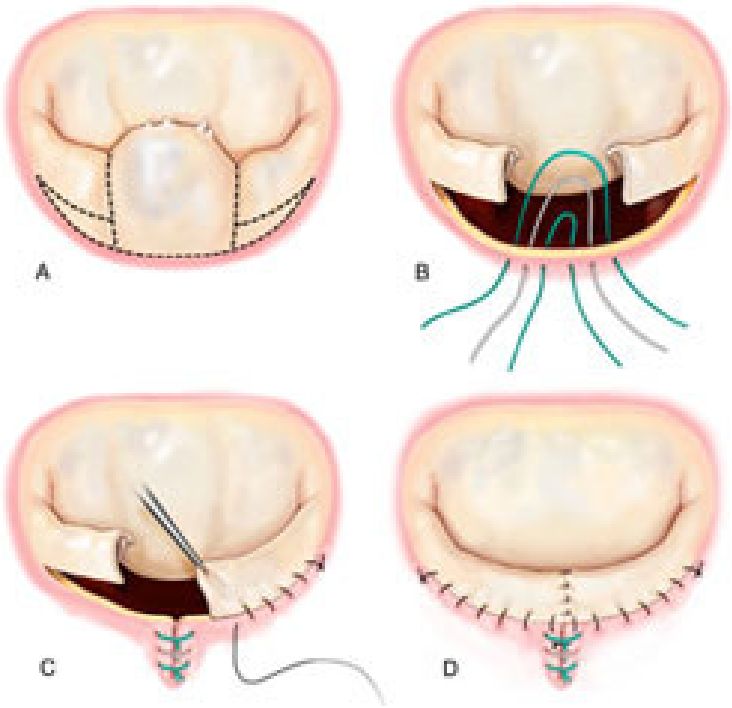

Figure 8 – An example of a quadrangular resection where (A) a section of the posterior leaflet is removed, (B) tissue adjacent to the valve is sutured, (C) the two leaflet edges are drawn together and sutured in place, and (D) a completed repair [7]**.**

1.3 Objectives of the study

As the most commonly diseased valve of the heart, the mitral valve has been the subject of extensive research for many years. Much of this research has focused on the development of surgical repair techniques and mainly consists of in vivo clinical studies into the efficacy and long-term effects of different procedures. Given the large number of parameters that come into play and that cannot be easily studied in the operating room, it is desirable to develop means of studying the mitral valve ex vivo, incorporating patient data and the effects of different repair techniques on the valve prior to surgery. The

objectives of this study are two-fold. First, a three-dimensional model of the mitral valve is developed from patient specific data and is analyzed using a finite element analysis software to determine its dynamics. Secondly, several models of mitral valve repair techniques are developed and examined, specifically the annuloplasty ring, the double-orifice stitch, the paracommissural stitch, and the quadrangular resection. These models are developed to determine the feasibility of simulating patient specific mitral valve dynamics and potential repair techniques.

1.4 Organization of the thesis

This thesis is organized into seven chapters, mainly focusing on the modeling of the mitral valve. Background information has been presented on the mitral valve and the repair techniques investigated in this study. A review of previous work in modeling the mitral valve is given in Chapter 2. The material models used for the leaflet and chordae tendinae tissues is presented next, along with verification and validation of their accurate implementation in the model. A thorough description is given for the method of constructing the finite element model of the mitral valve and the various techniques used in the process. The methods used to modify the model to simulate the four types of mitral valve repair are then presented. Finally, the analysis results for all models are discussed, followed by conclusions from the study.

Chapter 2

Literature Review

2 Literature Review

Numerous efforts have been made in the past to accurately model the mitral valve, which presents several unique challenges to the analyst. For efficiency, many simplifications have been used to describe valve geometry and material properties, often at the expense of accuracy. Significant progress has been made in modeling the mitral valve over the past twenty years, including the modeling of mitral valve repair methods. In the following, the various models and methods used previously are discussed.

2.1 Finite Element Models of the Mitral Valve

Finite Element Analysis (FEA) is a computational technique often used for approximating solutions to complex problems. It is used extensively in mechanical engineering for analysing complex structures, calculating the stresses and strains based on the applied loads. In FEA, the structure is broken down into many smaller parts, called elements, defined by points called nodes. A solution to the governing equations is then calculated over each element of the structure; looking at all elements as a whole, this gives an approximation of the solution to the given problem. There are three key aspects to FEA: the geometry, the material properties, and the load and boundary conditions, which are discussed in this section with regards to applying FEA to the mitral valve.

In the history of finite element modeling of the mitral valve there are two principal aspects which may distinguish models and through which models have been improved. The first aspect is the geometric characteristics of the model. The geometries used in various mitral valve models range from very idealistic geometries to patient specific

geometries. Another aspect is the material models used to describe the behaviour of the biological materials comprising the mitral valve, which range from simplistic linear models to more realistic non-linear models. Additionally, there have been variations in the analysis methods, such as simplifying assumptions, dynamic or static modeling, loading and boundary conditions, and the modeling of the interactions of blood flow with the valve. There are three main groups involved in mitral valve modeling, located in Seattle, Italy, and Norway, along with researchers in the United Kingdom and elsewhere in the USA. Their various attempts and advances in modeling the mitral valve are herein examined with respect to these three areas: model geometry, material modeling, and analysis methods and their results.

2.1.1 Mitral Valve Geometry

Accurately reconstructing the geometry of the mitral valve for analysis faces two challenges: the complex anatomical structure of the valve and the difficulty in examining and measuring this structure in its natural setting. Different approaches have been taken in the past with regards to modeling the various features which form the mitral valve, as described in Chapter 1. Sources of geometric data have varied from the idealized, general shape to more specific measurements from human and porcine mitral valves. Regardless of the data source, the data is then processed to reconstruct the mitral valve as a 3D model. In general, mitral valve models consist of all the main features of the natural valve, including the leaflets, chordae tendinae, and the papillary muscle heads.

The first technique used for reconstructing the valve geometry in three dimensions was developed in 1993, in Seattle, by Kunzelman *et al.* for the first finite element model of the mitral valve. Resin casts of porcine mitral valves in the open position were created, of which their cross-sections provided coordinates in the Cartesian-coordinate system for the leaflets and the attachment points of the chordae tendinae to the leaflets and papillary muscle heads [10]. The leaflets were defined using quadratic splines from the annulus to the free margin and given a uniform thickness [10]. The chordae were single, straight lines and the papillary muscle heads were single points to which the chordae attached [10]. The finite element model formed from this method was used for several studies of mitral valve dynamics and the authors assumed symmetry of the valve to reduce computation time [10-12]. In a 1997 study by Kunzelman *et al.* this assumption was eliminated, perhaps due to increased computing resources. Also, the authors increased the diameter of two chordae tendinae to represent the basal tendinae, which attach to the anterior leaflet [13]. These changes were intended to more accurately represent the shape of the mitral valve based on their observations [13].

In 1999, a research group in Italy, Maisano *et al.*, produced a new model of the mitral valve aimed at examining the effects of a repair procedure on mitral regurgitation. This model was developed for a hemodynamic study of the valve in a normal, single orifice state and after an Alfieri stitch procedure [14]. For this reason, the authors used a very idealized and simplified geometry of the valve in a static, open position, with no chordae tendinae, using data obtained from an echocardiogram study [14], [15]. The authors also assumed the orifice shape was circular, with a diameter significantly smaller than the

annulus [14]. Additionally, the annulus shape was defined as the shape of an annuloplasty ring [14]. Later, in 2002, this research group produced a new model to more accurately represent the mitral valve apparatus and simulate the stresses and dynamics during systole and diastole. Additions to the model were chordae tendinae, which were represented by straight lines from the leaflet free margin to the two points representing the papillary muscle head [16]. In a 2005 study by this group, the authors used literature data defining the geometry of the mitral valve to develop a new valve reconstruction [17]. The free margin of the leaflets was modeled using a sinusoidal function, using literature data to create idealized leaflets [17]. Three versions of the model were created: one with a circular annulus, and two with annuloplasty rings of different geometries [17]. In all three cases, the authors assumed symmetry along the plane parallel to the long axis of the valve and passing through the centres of the two leaflets [17]. The construction of the chordae tendinae remained unchanged from previous models, with fifty-two chordae included in the model. However, literature data was used to position the papillary muscles [17]. Of note is that both papillary muscle heads were positioned symmetrically relative to the valve, using an average of the asymmetric literature data [17]. In a later incarnation of this model, the authors incorporated the variable thickness feature implemented previously by the Kunzelman group [18].

In 2008, a new approach was used by the group in Italy to obtain the geometry for reconstructing the annulus and the papillary muscle heads. The authors used 3D transthoracic echocardiography to obtain ultrasound images of a subjects mitral valve

[19]. Images were used depicting the end of the diastole phase of the cardiac cycle [19], when the valve is open and pressure is minimal. Data points were selected from the images to define the annulus and the two papillary muscle heads [19]. The annulus data points were smoothed using sixth-order Fourier functions and the number of points was increased by a factor of approximately ten [19]. As with their previous models, literature data was used to define the leaflet free margins and the leaflet profile was defined in the same manner as before, using a sinusoidal function [19]. Also, the number of chordae tendinae attached to the free margin was increased to fifty-eight from the previous model's fifty-two and two basal chordae were connected to the anterior leaflet [19].

Another method of obtaining geometric data of the mitral valve from *in vivo* sources was introduced by the Italian group in 2011. The researchers implanted radiopaque markers in sheep hearts and used a fluoroscope to measure the geometric properties of the anterior leaflet [20]. This data was then used to form a three dimensional model of the anterior leaflet for finite element analysis. This model lacked the posterior leaflet, as the anterior leaflet was the focus of their research, but it did include the chordae tendinae, which were modeled in the same way as with their previous models [20]. This method should be applicable to the posterior leaflet and is possibly more accurate than other methods due to the radiopaque markers. However, it is much more involved as the markers must be surgically inserted.

A more recent method has been introduced by the Italian researchers in the past year which uses cardiac magnetic resonance imaging (CMR) to extract the valve geometry

from individual patients [21]. Their method involves taking cross-sectional images at ten degree intervals around the long axis of the valve, from which coordinates were determined for the defining features of the mitral valve apparatus [21]. The resulting model is distinct from models using idealized geometry, with a much more varied and uneven shape to the valve construct. By using patient-specific data the authors believe they are able to construct more accurate models, even to describe mitral valve dysfunction [21].

Another group, situated in Norway, introduced a method in 2009 for using 3D echocardiography and post-mortem measurements to reconstruct a porcine mitral valve. The echocardiography was performed by surgically opening the chest of the pig and position the ultrasound probe against the outer wall of the heart [22]. The annulus was modeled as a symmetric non-planar ellipse, which was fitted to the data points obtained from the ultrasound images at the beginning and peak of systole [22]. The non-planarity of the annulus was intended to more accurately represent the physiological geometry of the valve, wherein the anterior portion of the annulus curves upwards to a peak at the centre of the anterior leaflet, while the posterior leaflet is flat [22]. An additional feature of this approach was a variability of the peak height of the anterior annulus throughout the cardiac cycle, which is also more representative physiologically of the mitral valve [22]. The leaflets in this model were given an idealized geometry based on anatomical measurements of the leaflets during the post-mortem analysis and on the literature [22]. A novel addition to mitral valve modeling was the introduction of branched chordae tendinae. The tendinae, twenty in total, including two strut tendinae, attached to points

representing the papillary muscle heads, as with previous models [22]. However, at the mid-point of the tendinae, the tendinae split into three branches which attached to the free margin of the leaflets [22]. This feature was intended to represent the webbed nature of the chordae tendinae where they attach to the leaflets in the natural valve.

In another iteration of this model the researchers examined the effects of using two or more material layers to described the leaflet thickness. Previous research by others had found that the mitral valve leaflets were formed of three layers, each with different material properties [23], [24]. In previous models, the leaflets were assumed to be homogenous; however this study sought to determine the effects of using different material properties across the thickness of the valve. It is noteworthy that the researchers concluded this did not affect the dynamics of the valve in their analyses [23].

A variety of other models of the mitral valve have been created by researchers around the world. These models used idealized, symmetric geometry based on published geometric data from various sources in the medical literature [25-28]. The annulus and leaflets were constructed from the data using ellipsoids, splines, and sinusoids, with the annulus forming a D-shape [25-28]. One such model defined the annulus and leaflets using a set of parametric equations defining curves in three dimensions to represent a closed mitral valve [27]. Additionally, the chordae tendinae in several models were either not included in the model [25-27], represented using boundary conditions [27], or were modeled with short branches attaching them to the free margin [28]. In one model the location of the

papillary muscle heads was idealized, adjusted to ensure proper coaptation (or closure) of the valve [28].

2.1.2 Material Modeling

Material modeling of the soft-tissues comprising the mitral valve apparatus has seen significant development in the last twenty years [29-31]. At the microscopic level, the biological tissue forming the leaflets and chordae are constructed from cells and fibrous tissue. The orientations and types of fibres lead to a nonlinear, transversely isotropic, elastic behaviour of the tissue. The leaflets are transversely isotropic in that the leaflets have different material properties along two of their principal axes (radial and circumferential) and the third axis has the same properties as one of the other two. The material behaves nonlinearly such that, when under tensile load, the tissue initially undergoes large deformations at low loads until it reaches a point where deformation is significantly less for any increase in load. From the first finite element model, attempts have been made to accurately model this behaviour, with various approaches employed by researchers. The challenges encountered in modeling the mitral valve materials include limited sources of material data, mathematical models to describe the material behaviour, and the ability to implement the material model in a finite element model.

The first models developed by Kunzelman *et al*. in 1993 incorporated a linear model for the leaflet tissues. An assumption was made, based on medical literature, that the mitral valve functioned in the high load-low deformation region of the stress-strain curve, allowing the authors to assume linearity in the tissue. The authors performed uni-axial tensile testing of strips of leaflet tissue, presumably exised from porcine mitral valves, to

find elastic moduli for the two principal directions of the leaflets (radial and circumferential directions). This method was used for all mitral valve finite element models published prior to 1998 and was used by the Italian group up until 2007 [10-13], [17], [18]. A similar method was used by Dal Pan *et al*. in 2004 [27], however this model was based on uni-axial tensile test data obtained by Barber in 2001 [32]. A fluid-structure interaction (FSI) model published recently, in 2010 by Lau *et al.*, neglected the non-linear properties of the leaflets. As a first-generation FSI model, the materials were treated as linear elastic as a simplifying assumption since the focus was on the interaction between the blood and mitral valve [28]. The resulting mitral valve dynamics determined using the linear models varied in the degree of coaptation [10-13], [17], [18], or closure, of the leaflets, with some seeing limited, incomplete coaptation [17], [18].

In 1995, a study was performed by May-Newman *et al*. to determine more physiologically accurate stress-strain curves of the mitral valve leaflets. The authors performed biaxial tensile testing of leaflet specimens, which consists of stretching a square specimen in both principal directions concurrently [31]. This experiment resulted in non-linear, anisotropic stress-strain data and the observation that the behaviour in both directions was coupled, rather than entirely independent as was assumed in the first mitral valve models [31]. From this study, the authors developed a constitutive law describing the mitral leaflets' stress-strain characteristics using strain energy theory relating to hyperelastic materials [29], [33]:

$$W = c_0\left(e^{Q} - 1\right) \tag{0.1}$$

with

$$Q = c_1\left(I_1 - 3\right)^2 + c_2\left(\sqrt{I_4} - 1\right)^4 \tag{0.2}$$

In these equations, W is the strain energy, c_0, c_1, and c_2 are material constants, I_1 is the first invariant of the right Cauchy-Green strain tensor, and I_4 is a pseudo-invariant of the same tensor and that formed from the unit vector defining the preferred fiber direction of the material in the undeformed configuration. This work by May-Newman resulted in a change in the way the leaflet materials were modeling in finite element models.

The mitral valve data and constitutive law by May-Newman was successfully implemented by Einstein *et al*., in 2003, for use in finite element analysis [34]. This lead to the first successful implementation of non-linear material properties in a mitral valve finite element model by Einstein in 2004 [35], with a successive model in 2005 [36]. In 2007, Prot *et al*. implemented another non-linear material model for the mitral valve [37], based on the strain-energy function developed by Holzapfel *et al*. for modeling arterial walls [38]:

$$W\left(I_1, I_4\right) = c_0\left[e^{c_1\left(I_1-3\right)^2 + c_2\left(I_4-3\right)^2} - 1\right] \tag{0.3}$$

The notations in this equation are similar to those in Eqs. (2.1) and (2.2). This model was used in the authors' successive finite element modeling of the mitral valve [22], [23], [37]. In 2008, this non-linear material model was also implemented in the finite element model of Votta *et al*. Also in 2008, another constitutive model in the finite element software ABAQUS was used for the mitral valve by Avanzini in Italy:

$$W\left(\varepsilon\right) = \sum_{i=1}^{N} C_{i0}\left(\overline{I}_1 - 3\right)^i + \sum_{i=1}^{N} \frac{1}{D_i}\left(J^{e1} - 1\right)^{2i} \tag{0.4}$$

where C_{i0} and D_i are material parameters, $\overline{I}_1$ is the first strain invariant, and J^{e1} is the elastic volume strain ratio [26]. Avanzini used the material data obtained from Barber

[26]; as discussed above, this data was obtained from uni-axial testing, unlike the data used for other non-linear models. An improved FSI model was recently published by Lau which included the non-linear nature of the leaflets. The authors treated the leaflets as non-linear orthotropic, using the leaflet data of May-Newman and a material model in finite element software LS-DYNA called MAT_NONLINEAR_ORTHOTROPIC [39]. These non-linear material models, particularly the transversely isotropic models, were all able to better fit the stress-strain behaviour of the leaflet materials, thus improving the accuracy of the finite element models.

2.1.3 Analysis Methods

Another area of differentiation between finite element models is in the type of analysis, the load and boundary conditions of the models. The type of analysis mainly depends on the goal of the study and the assumptions the analysts have used to simplify the model. The three types of analysis employed in the mitral valve literature are structural analyses, fluid dynamics analyses, and fluid-structure interaction analyses. Structural analysis has been the most prevalent, in which case the authors neglect the blood flow through the valve. The fluid dynamics analyses neglect the deformations in the leaflets, keeping them static, while the FSI models combine the two types. The load and boundary conditions of the models depend to a large extent on the type of analysis being performed. Since the fluid-only models neglect movement of the leaflets, only the structural and FSI types of analysis are discussed herein.

In structural analyses of the mitral valve, the effect of blood flow has been simulated using pressure load curves based on the medical literature. The pressure loads were derived from the pressure difference between the left ventricle and the left atrium throughout the cardiac cycle, wherein the pressure difference typically reaches a peak of 120 mmHg during systole and a minimum of zero during diastole [10]. The specific load curve used in a model has depended on the preference of the analyst. Initial models simulated only the systolic phase of the cardiac cycle, with the pressure increasing from the minimum transvalvular pressure to the peak pressure of the cycle and applied uniformly to the leaflet surfaces [1-4,6-9,24,25]. The nature of the curves varied, with Maisano's group using a linear curve [15], [17-19] while other studies, such as those by Prot and Kunzelman, used curves which more accurately represented transvalvular pressure profile [1-4,11,12,24,26,29,30]. For instance, models by Kunzelman's group used a linear curve from 0 mmHg up to 70 mmHg and sinusoidal curve from 70 mmHg to 120 mmHg [10-13], [35]. Recent models have featured the end portion of systole, in which the pressure drops to the initial pressure, to simulate the opening of the leaflets [41].

Implementation and loading in fluid-structure interaction models has varied, depending on the purpose of the study. Two distinct approaches have been used: (1) pressure loads on both the fluid and the leaflets and (2) pressure loads applied to the fluid only. In the first approach, a pressure load is applied to the leaflet surfaces, as with the non-fluid analyses described above. Additionally, pressure load is also applied to the fluid from the ventricle side of the valve. This fluid pressure load models the initial systolic phase,

increasing from 0 kPa beginning at systole to 12 kPa at mid-systole, and holding at 12 kPa for the remainder of the simulation [28], [41]. In the other approach, a transvalvular pressure load is applied to the fluid domain describing the pressure gradient throughout the cardiac cycle. This load condition can also be used to simulate fluid flow through the valve during diastole, while neglecting the systolic phase [15], [39]. The second approach depends on the interaction between the fluid domain and solid domain to simulate the dynamics of the valve, requiring coupling of the two domains. In both cases, the solid model is immersed in a fluid volume, requiring attention be paid to the interface between solid and fluid elements and their coupling.

The boundary conditions used for FEA and FSI models of the mitral valve are fairly similar across all prior work and reflect the valve's physiological environment. Boundary conditions are applied at the two anchoring points of the mitral valve structure: the annulus and the papillary muscle heads. A typical simplifying boundary condition is a fixed or a hinged condition applied to nodes along the annulus and the nodes which make up the papillary muscles [10], [18], [26-28]. A more complex boundary condition, for both the annulus and the papillary muscles, combines a load and boundary condition to replicate the dynamics of the annulus and papillary muscles during the cardiac cycle. As the annulus dilates during diastole and contracts in systole, some analysts have applied loads to nodes along the annulus, either as displacements or as forces [17], [19], [39]. The load is constrained by a boundary condition which restricts movement of these nodes to the plane formed by the annulus. Similarly, vertical displacements have been applied to the nodes of the papillary muscle heads to approximate their motion during

systole. In this case, the nodal movement is constrained to the direction of the long axis of the valve, the axis perpendicular to the annulus plane. In FSI, additional boundary conditions surround the fluid domain, with fluid flow restricted to the direction of flow in a normal mitral valve [14], [15], [28], [39], [41].

Another boundary condition, that of contact between the leaflets, is required for analysing the dynamics of the mitral valve. In FEA models, contact between leaflets can be handled by settings within the commercial analysis software used by researchers, such as ABAQUS and LS-DYNA 971, while contact settings are not available for the beam elements used to model the chordae tendinae [11], [12], [24], [41].

2.2 Mitral Valve Repair Simulation

Several of the models discussed above have been intended or modified for modeling certain mitral valve repair procedures. The most common repair modeled has been the edge-to-edge repair, also known as the Alfieri stitch. Other models have included analysis of chordae tendinae replacement and annuloplasty ring prostheses.

The first model of an Alfieri stitch was of a double-orifice stitch in 1999 by the group in Italy which had actually introduced the repair technique itself [42]. This model had no structural component to it, intended only to determine the effects on fluid flow of the repair and did not accurately represent the mitral valve geometry [14], [15]. The first structural analysis of the Alfieri stitch was by Dal Pan *et al*. in 2005. The model geometry was from the literature, as described previously, with the addition of an element

representing one suture. The starting position of the valve was part way between open and closed, with the leaflet edges nearly in contact with each other [27]. Three parameters governed suture placement in their model: position along the posterior/anterior free margins, suture length or extension, and the effect of different annulus sizes with one suture in the centre. For the first parameter, suture position ranged from the centre, forming two orifices, to adjacent to a commissure, forming one orifice [27]. For the length parameter, the authors analysed the effect of using different lengths of suture, resulting in greater lengths of the leaflets being joined together [27]. The different annulus sizes used for the third case varied from larger than normal, as in a diseased state, to a contracted annulus, as if an annuloplasty ring had been applied [27].

The mitral valve model by Avanzini in 2008 used a very similar configuration, but the suturing was simulated a little differently. Two suture parameters were considered: suture position and suture extension. Suture positions included central, commissural, and half-way between the central and commissural positions and the suture length was the maximum length used in the Dal Pan model [26], [27].

The final Alfieri stitch model, created by Lau *et al.* in 2011, used a valve model with the leaflets initially in the open position to model a double-orifice Alfieri stitch. Thermal beam elements were applied to the edges of the idealized leaflets, at the valve centre, with a negative thermal load applied to draw the leaflet edges together [39]. The result of this analysis was used as part of a FSI analysis, with rigid beam elements simulating the sutures[39]. Additionally, two cases were analyzed, one with an annuloplasty ring and

one without, to determine the effects of the two conditions. In analyses of Alfieri stitches, the sutures can be given the material properties of actual sutures used in cardiac surgery for accuracy [26], [27].

In other analyses, chordal rupture was analysed along with subsequent replacement of the ruptured chordae with sutures [11], [12]. The ruptured chordae were simply removed from an existing model and then replaced with sutures [11], [12]. Another model analysed the effects of the shape of annuloplasty rings on valve function [18]. This study used two different rings: a Physio ring, which is of a idealized annulus shape, and a Geoform ring, which has a much more complex shape [18]. The Geoform ring was designed to alter the annulus shape to treat mitral valve regurgitation [18]. In both cases, the annulus of the model was fitted to the shape of the ring and fixed in position [18]. The rings themselves are not physically modeled, only as a geometrical and boundary condition [18].

2.3 Potential for Improvement in Mitral Valve Modeling

Finite element modeling has progressed substantially from the first model in 1993, with advances in material modeling and geometric reconstruction. The trend in geometric reconstruction is towards developing more advanced methods for acquiring mitral valve geometry to better represent its physiological nature. This has resulted in researchers using medical imaging technologies to acquire in vivo data from both porcine and human mitral valves. Reliable and accurate methods for modeling human mitral valves could be used as a tool in the medical setting to aid surgeons in their treatment of

mitral valve disease. In light of this, this thesis aims to improve the knowledge base for using medical imaging to reconstruct the mitral valve using patient data.

Further improvement is also possible in the modeling of mitral valve repair procedures. Although models have been created previously, improvements could be made in some cases to increase the accuracy of the model, such as modeling repairs using valve geometry at the peak of systole. Modeling of repair procedures could be an important tool to be used by surgeons for surgical planning and evaluating types of repairs, both for a specific and for novel techniques. Additionally, no previous attempt has been made to model a quadrangular resection. In terms of mitral valve repair, the aim of this thesis is to illustrate a technique for simulating annuloplasty, Alfieri stitches, and quadrangular resection, as discussed in Chapter 1, using patient data of a mitral valve during systole.

Chapter 3

Material Properties of the Mitral Valve

3 Material Properties of the Mitral Valve

As the mitral valve structure is comprised of various biological materials, it is important to understand the mechanical behaviour of these materials when attempting to model them. This chapter details the theoretical background for the material properties of mitral valve tissues and the modeling of their mechanical behaviour.

3.1 Leaflet Material Properties

3.1.1 Mechanical Behaviour and Modeling

As biological tissue, the leaflets of the mitral valve are formed of complex cellular and extracellular structures. The leaflets consist of three layers across their thickness: the ventricularis, the fibrosa, and the atrialis, formed of elastin fibres, collagen fibres, and glycosaminoglycans in varying amounts [29]. The ventricularis is very thin and is typically neglected in modeling the leaflets, whereas the thicker fibrosa and atriali are modeled as one homogenous layer. The elastin and collagen fibres in the atriali and the fibrosa, respectively, control the mechanical behaviour of the material [29]. Elastin fibres exhibit linear stress-strain behaviour under tension. Collagen fibres are wavy, undulated fibres exhibiting nonlinear material properties. Under tension, the collagen fibres initially undergo large deformations at low stress. As the fibres straighten, the material stiffens and the stress increases rapidly over a small deformation [43]. The combination of these two fibre types causes the leaflets to exhibit mechanical properties very similar to those of a rubber-like material. Previous work by May-Newman *et al*. has

shown that the leaflets can be modeled as a hyperelastic, transversely isotropic material using the principles of finite elasticity, using a strain-energy function *W*.

According to Humphrey [43], for an incompressible, isotropic material the strain-energy function must be of the form

$$W = W\left(I_C, II_C\right) - \tilde{p}\left(III_C - 1\right) \tag{0.5}$$

where the invariants of *C*, the right Cauchy-Green tensor, are given as

$$I_C = \mathrm{tr}C, \quad II_C = \tfrac{1}{2}\left[\left(\mathrm{tr}C\right)^2 - \mathrm{tr}C^2\right], \text{ and } \quad III_C = \det C \tag{0.6}$$

and $\tilde{p}$ is a Lagrange multiplier. Several strain energy different functions of this form have been developed for modeling cardiovascular tissue and, for instance, commercial FEA software LS-DYNA has implemented the Guccione strain-energy function into its material options. The Guccione model was initially developed to model heart muscle tissue [44], but has since been used successfully to model other types of heart tissue as well [45], [46]. The Guccione model is given as

$$W = \tfrac{c}{2}\left(e^Q - 1\right) + \tfrac{p}{2}\left(III_C - 1\right)^2 \tag{0.7}$$

where *c* is a constant, *p* is a Lagrange multiplier ensuring quasi-incompressibility, and *Q* is a function of the Green strains of the material:

$$Q = b_1 E_{11}^2 + b_2\left(E_{22}^2 + E_{33}^2 + E_{23}^2 + E_{32}^2\right) + b_3\left(E_{12}^2 + E_{21}^2 + E_{13}^2 + E_{31}^2\right) \tag{0.8}$$

The Green strains E_{ij} are in the circumferential (1), radial (2), and thickness (3) directions of the leaflet. Material constants b_i define the stress response of the material, along with constant *c*, based on experimental Green strain and Cauchy stress data for the material.

3.1.2 Experimental Material Properties

In order to apply the Guccione strain-energy model to the mitral valve leaflets, the mechanical behaviour of the leaflets must be known to determine the material constants used in the model. The results of a study by May-Newman *et al*. [31] on porcine mitral valves, which have very similar anatomy to human mitral valves, were used to determine these constants. In the May-Newman study, portions of leaflet were tested in a biaxial-tensile testing apparatus, in the manner shown in Figure 9a, from which the Cauchy stress and Green strain were calculated for the radial and circumferential directions of the leaflets.

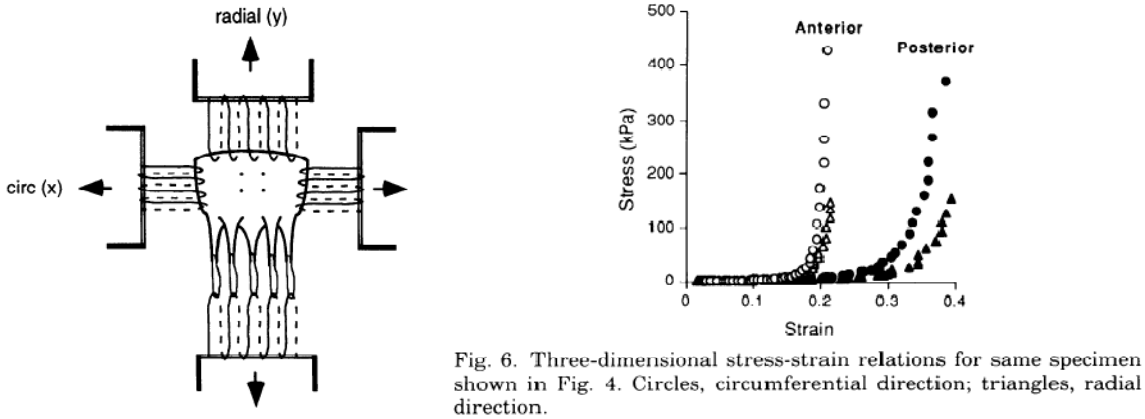

Fig. 6. Three-dimensional stress-strain relations for same specimen shown in Fig. 4. Circles, circumferential direction; triangles, radial direction.

(a) **(b)**

Figure 9 – (a) Biaxial tensile testing of leaflet tissue [31]; (b) Stress-strain behaviour of mitral valve leaflet tissue [31].

3.1.3 Material Constant Evaluation

The material constants used in the Guccione model were determined by fitting the model to the experimental data. An optimization method was used to minimize the error between theoretical Cauchy stress calculated with the Guccione model and the experimental Cauchy stress, for a given Green strain in the principal directions. The

Cauchy stress tensor is a function of the deformation gradient tensor $\overline{\overline{F}}$ and the 2nd Piola-Kirchoff stress tensor $\overline{\overline{S}}$:

$$\bar{t} = \frac{1}{J}\left(\overline{\overline{F}} \cdot \overline{\overline{S}} \cdot \overline{\overline{F}}^{T}\right) = \frac{1}{J}\left(\overline{\overline{F}} \cdot \frac{\partial W}{\partial E_{ij}} \cdot \overline{\overline{F}}^{T}\right) \tag{0.9}$$

where J is the determinant of $\overline{\overline{F}}$, a function of the stretch ratios $\lambda = l/L$ in the principal directions of the material, and "." represents the dot product between tensors. Considering only the principal directions, radial, circumferential, and thickness, the deformation gradient is

$$\left[\overline{\overline{F}}\right] = \begin{bmatrix} \lambda_1 & 0 & 0 \\ 0 & \lambda_2 & 0 \\ 0 & 0 & \lambda_3 \end{bmatrix}. \tag{0.10}$$

As an incompressible material, the determinant is $J = \lambda_1\lambda_2\lambda_3 = 1$, simplifying the Cauchy stress to

$$\bar{t} = \overline{\overline{F}} \cdot \frac{\partial W}{\partial E_{ij}} \cdot \overline{\overline{F}}^{T} \tag{0.11}$$

where the Cauchy stress in the principal directions is

$$t_{ii} = \lambda_i^2 \frac{\partial W}{\partial E_{ii}}, \text{ for } i = 1,2,3. \tag{0.12}$$

The equation can be written as a function of the Green strain, with Green strain defined by the right Cauchy stress tensor $\overline{\overline{C}} = \overline{\overline{F}}^{T} \cdot \overline{\overline{F}}$ as

$$\overline{\overline{E}} = \tfrac{1}{2}\left(\overline{\overline{C}} - \overline{\overline{I}}\right) = \tfrac{1}{2}\left(\overline{\overline{F}}^{T}\overline{\overline{F}} - \overline{\overline{I}}\right) \tag{0.13}$$

Applying the matrix form of $\overline{\overline{F}}$ and isolating for the stretch ratios gives

$$\lambda_i^2 = 2E_{ii} + 1, \text{ for } i = 1,2,3 \tag{0.14}$$

and substituting equation (0.14) into (0.12) gives the Cauchy stress as a function of the Green strain and the partial derivative of the strain energy function:

$$t_{ii} = \left(2E_{ii} + 1\right)\frac{\partial W}{\partial E_{ii}}, \text{ for } i = 1,2,3 \tag{0.15}$$

with

$$\frac{\partial W}{\partial E_{ii}} = \tfrac{1}{2} c \frac{\partial Q}{\partial E_{ii}} e^{Q} \tag{0.16}$$

The Cauchy stress across the thickness of the leaflet is considered negligible, so the Cauchy stress t_{33} is ignored, while the Cauchy stresses in the first and second principal directions are calculated, providing theoretical values based on the constants. The difference between the theoretical Cauchy stresses and the experimental values, for the two principal directions, is the error $e_{t_{ii}} = t_{ii_{theoretical}} - t_{ii_{\exp erimental}}$, for $i = 1,2$. The error for both directions is minimized using the Trust-Region-Reflective algorithm in MATLAB (`lsqnonlin`) for solving nonlinear least-squares problems. The function is used in optimization problems of the general form

$$\min_x \left\| f\left(x\right)\right\|_2^2 = \min_x \left(f_1\left(x\right)^2 + f_2\left(x\right)^2 + \ldots + f_x\left(x\right)^2 \right) \tag{0.17}$$

where $f\left(x\right)$ is a function returning the vector values of $f_i\left(x\right)$ for i = 1, 2, …, n. Given upper and lower bounds for x and a starting value, the function optimizes the value of x. The curve fitting algorithm in this case entailed solving for the Cauchy stress error, using equation (0.15), to optimize the material constants c, b_1, and b_2. The initial constants used as starting values were $\left(c = 0.01,\ b_1 = b_2 = 0.1\right)$ for the posterior leaflet and

$(c = 0.015,\ b_1 = b_2 = 0.1)$ for the anterior leaflet, with lower bounds of 0.001, 0.1, and 0.1 and upper bounds of 10, 20000, and 20000, respectively. The resulting material constants for the posterior and anterior leaflets were successfully determined and are given in Table 1. Figure 10 shows the Cauchy stress-Green strain curves for both the experimental data and the Guccione model with optimized constants, for both principal directions of the anterior and posterior leaflets.

Table 1 - Leaflet Material Constants

	Anterior Leaflet	Posterior Leaflet
c	0.0015	0.001
b_1	38.831	15.1
b_2	8.894	4.599

Figure 10 shows the stress-strain curves generated using these constants for both leaflets. The posterior leaflet's constants produce a better fit than the anterior leaflet's constants, but both are considered good fits due to the inaccuracy inherent in the experimental data. Testing of biological tissue is very difficult, with many variables which may affect the results, so there is a large margin of error in the experimental stress-strain curves.

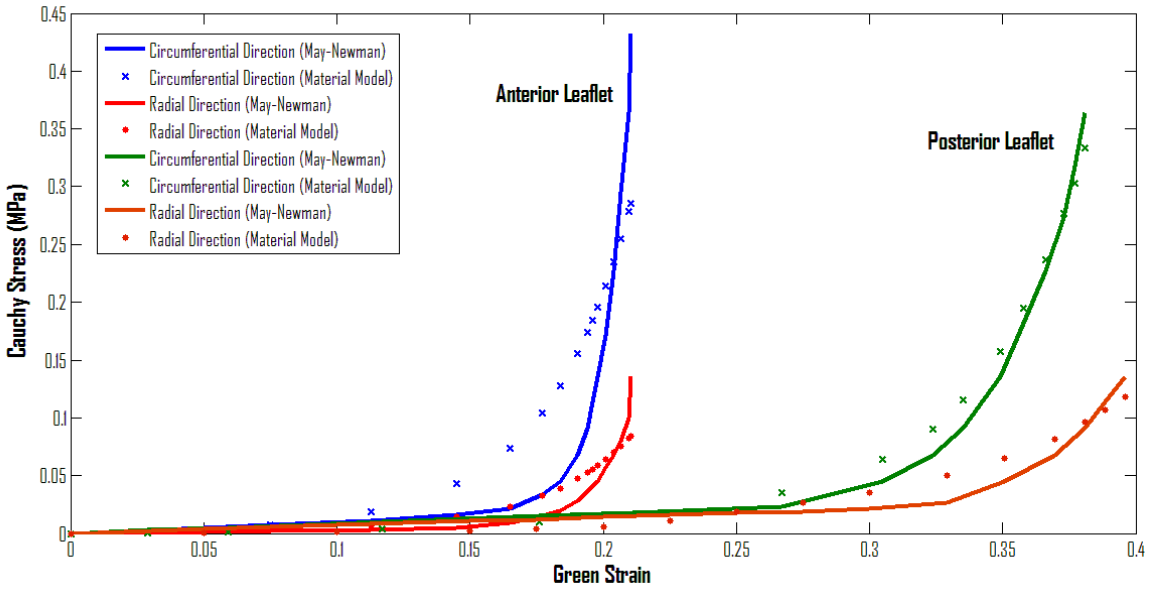

Figure 10 - Theoretical (Material Model) Cauchy stress from the optimized material constants plotted with the experimental data [31].

3.1.4 Simulated Biaxial Tensile Testing

The Guccione material model and the material constants given in Table 1 were validated by simulating a biaxial tensile test of a leaflet specimen using LS-DYNA 971. In the simulated test, two edges of the leaflet specimen are fixed in position and displacements are applied to the remaining two edges, as in the experiments performed by May-Newman *et al*. A model was created in FEA software ANSYS using brick elements in the shape of a leaflet specimen with a thickness of 0.55 mm, a length of 10 mm, and a width of 10 mm. Constraints and displacements were applied to the model as indicated in Figure 11, where a vertical arrow represents a node fixed in the vertical axis and a horizontal arrow represents a node fixed in the horizontal axis, in the direction of the arrow.

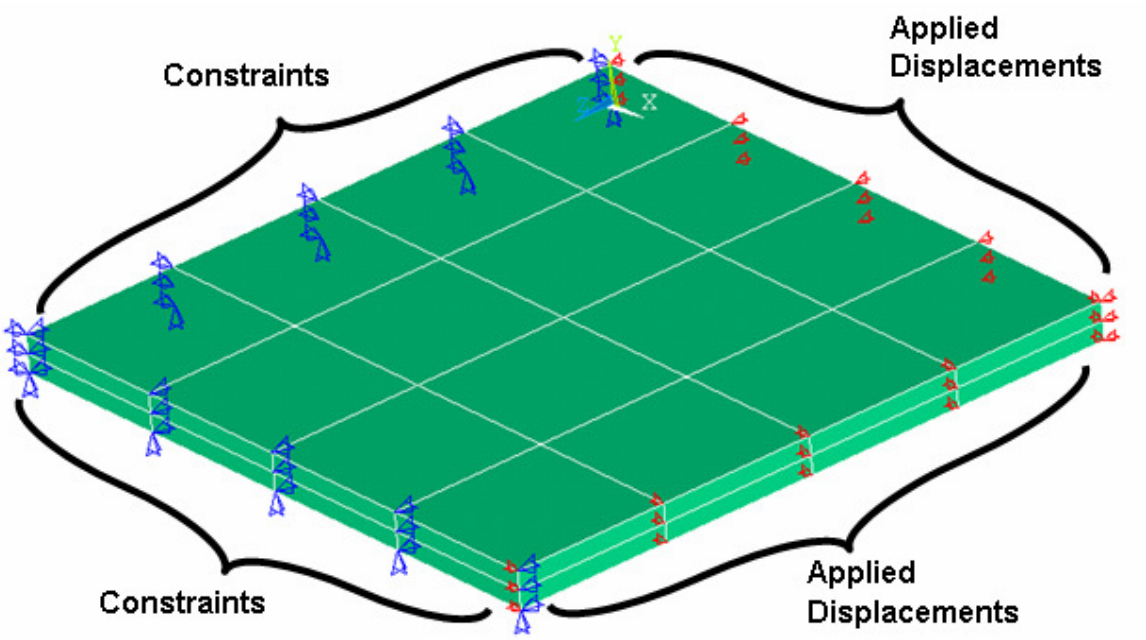

Figure 11 - Biaxial Tensile Test Model

The element and nodal data were exported from ANSYS and used to create an input file for LS-DYNA, for dynamic analysis. Displacements were calculated from the Green strain data obtained from the May-Newman study and were applied using the BOUNDARY_PRESCRIBED_MOTION_NODE keyword in LS-DYNA. The load curve for each test is given in Table 2 with the duration of the loading. The analysis began with a displacement of zero and increased linearly until the maximum displacement was reached. The results of the test are plotted in Figure 12 and Figure 13 with the experimental and theoretical data from Figure 10. The tests show that the dynamic finite element analysis software, LS-DYNA 971, can handle large material and geometric deformations properly and is able to accurately model the stress-strain behaviour of the mitral valve's leaflets.

Table 2 - Loads applied in simulated biaxial tensile test.

Posterior Leaflet			Anterior Leaflet		
	Displacement			Displacement	
Time	Circumferential	Radial	Time	Circumferential	Radial
0	0	0	0	0	0
0.3962	3.38805	3.274035	0.2102	1.91889	1.91885

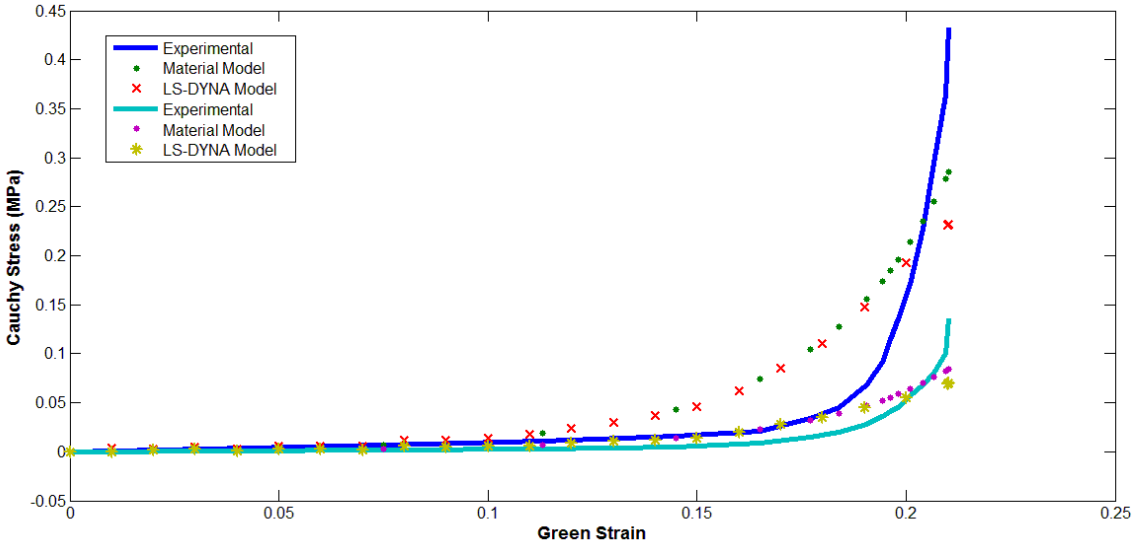

Figure 12 – Results of simulated biaxial tensile tests (LS-DYNA Model) for the anterior leaflet, compared to experimental (May-Newman [31]) and theoretical (material model) data.

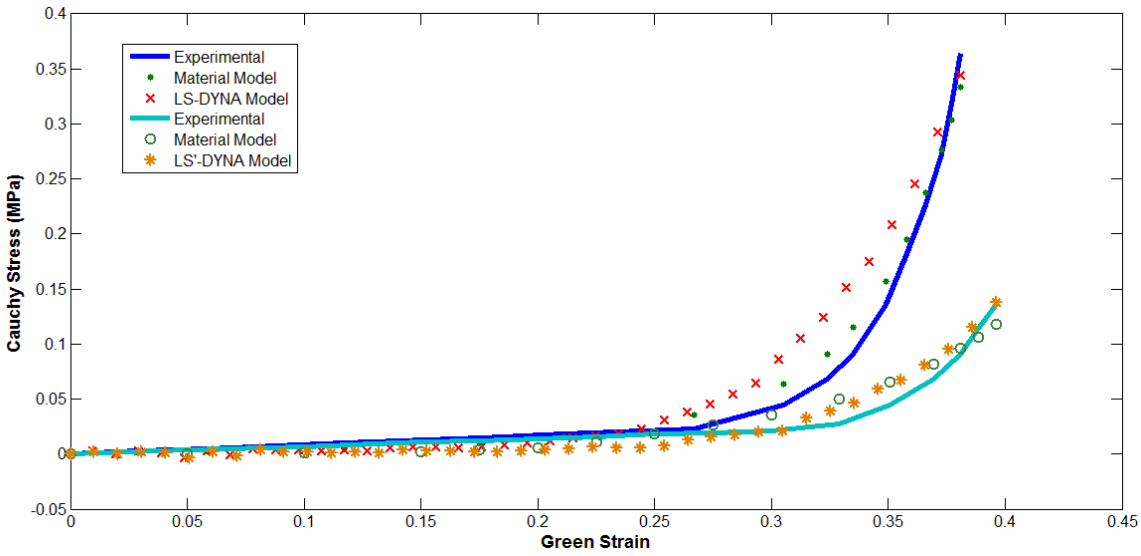

Figure 13 - Results of simulated biaxial tensile tests (LS-DYNA Model) for the posterior leaflet, compared to experimental (May-Newman [31]) and theoretical (material model) data.

3.2 Chordae Tendinae Material Properties

The chordae tendinae of the mitral valve are formed of the same basic elements as the leaflets, in a very dissimilar structure and proportions. The tendinae have a circular cross-section with three distinct layers of biological soft-tissue [47]. The outer layer is

called the endothelium and consists of a thin layer of endothelial cells [47]. Next is the middle layer, a thin layer of elastin fibres with the outer fibres of the layer arranged in mesh pattern and the inner fibres arranged parallel to the longitudinal axis of the tendinae [47]. Moving inwards, the elastin fibres become interspersed with wavy collagen fibres aligned with the longitudinal direction of the chordae [47]. As shown in Figure 14 - Chordae tendinae structure (Modified from [47]), the concentration of elastin fibres quickly diminishes from the outer circumference to the interior.

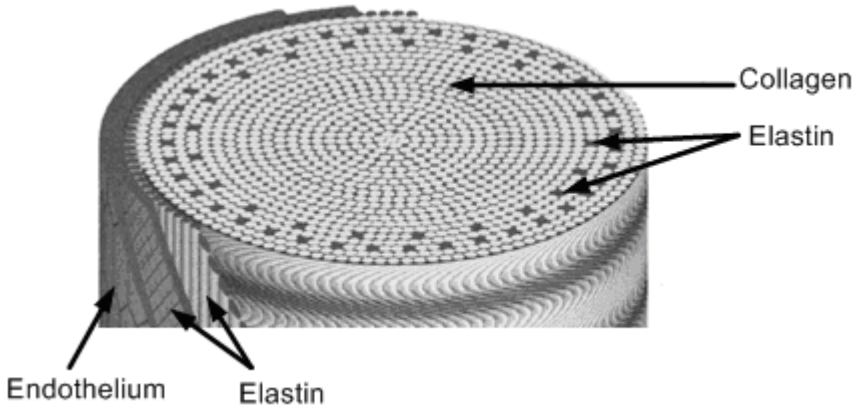

Figure 14 - Chordae tendinae structure (Modified from [47])

As with the leaflets, the elastin and collagen fibres give the tendinae a nonlinear stress-strain behaviour. Uniaxial tensile testing by Ritchie *et al*. determined the material behaviour of the chordae tendinae of porcine mitral valves [48], which are considered equivalent to the human mitral valve. Figure 15 shows the stretch-load behaviour of the tendinae from Ritchie *et al*. and, according to the authors of the study, the physiological range in which the chordae function falls between the A and B markers in Figure 15 [48]. Thus, a simplifying assumption used for modeling the chordae tendinae stress-strain behaviour in this study is to consider it as a linear material. From Ritchie *et al*. the average load per % strain of this region is 3.485 N/% strain, with an average chordae diameter of 1.6 mm [48]. The elastic modulus of the chordae is determined from

$$\Delta F = AE\Delta\varepsilon \tag{0.18}$$

where ΔF = 3.485 N and $\Delta\varepsilon$ = 0.01. Given the average diameter above and solving equation (0.18) for *E*, the elastic modulus is 173.3 MPa. This allows the analyst to use a simple, cable-like element in LS-DYNA 971 to model the chordae tendinae, as described in the next chapter.

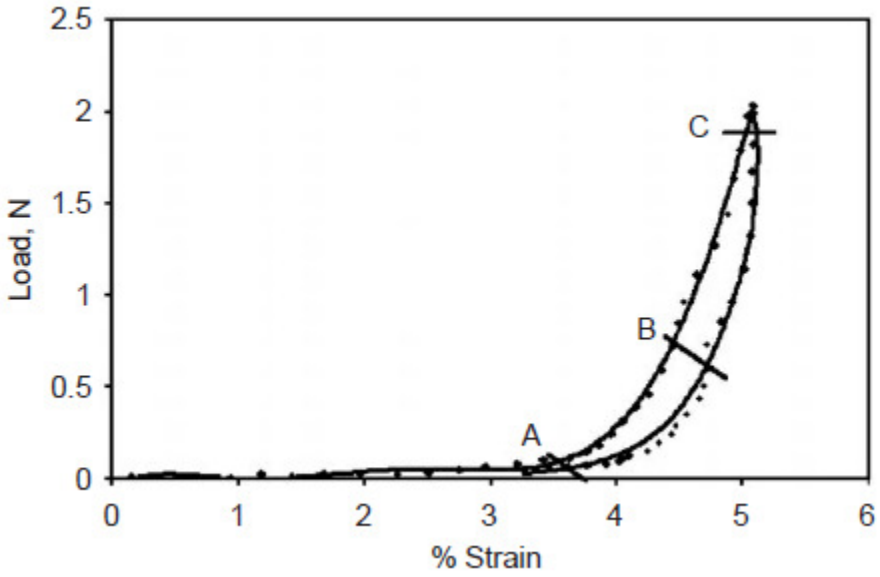

Figure 15 - Tensile test results of mitral valve chordae tendinae [48].

Chapter 4

Finite Element Model of the Mitral Valve

4 Finite Element Model of the Mitral Valve

4.1 Ultrasound Imaging

4.1.1 Transesophageal Echocardiography

Ultrasound images of the mitral valve were obtained during normal examination by a cardiologist of the University of Ottawa Heart Institute using 3D transthoracic echocardiography (TTE) and 3D transesophageal echocardiography (TEE). The protocol (2008710-01H) was approved by the Ottawa Hospital Research Ethics Board. Transesophageal echocardiography is an imaging method wherein an ultrasound probe is inserted into the patient's oesophagus to provide images of the heart, whereas in transthoracic echocardiography the probe is outside the body, scanning through the thorax. In both cases, the probe scans the mitral valve in three dimensions and the valve can be viewed via two dimensional videos at various angles about the vertical axis. 3D TEE provides clearer images than 3D TTE, as it scans through less tissue between the probe and the heart.

4.1.2 Image Acquisition

Images were obtained from a subject with a normal mitral valve (MVs1) and a patient with an unhealthy mitral valve (MVp1). The images of MVs1 were obtained from 3D TTE, while the images of MVp1 were obtained from 3D TEE. Eighteen images of the open mitral valve, in the diastolic phase of the cardiac cycle, were obtained for each model using the medical imaging software QLAB and the imaging format DICOM. The procedures being routine and the data completely de-identified, informed consent was

waived. Each image, such as Figure 16, shows a cross-section of the mitral valve at ten degree intervals about the vertical axis of the valve. The geometry of the mitral valve was then extracted from each set of images.

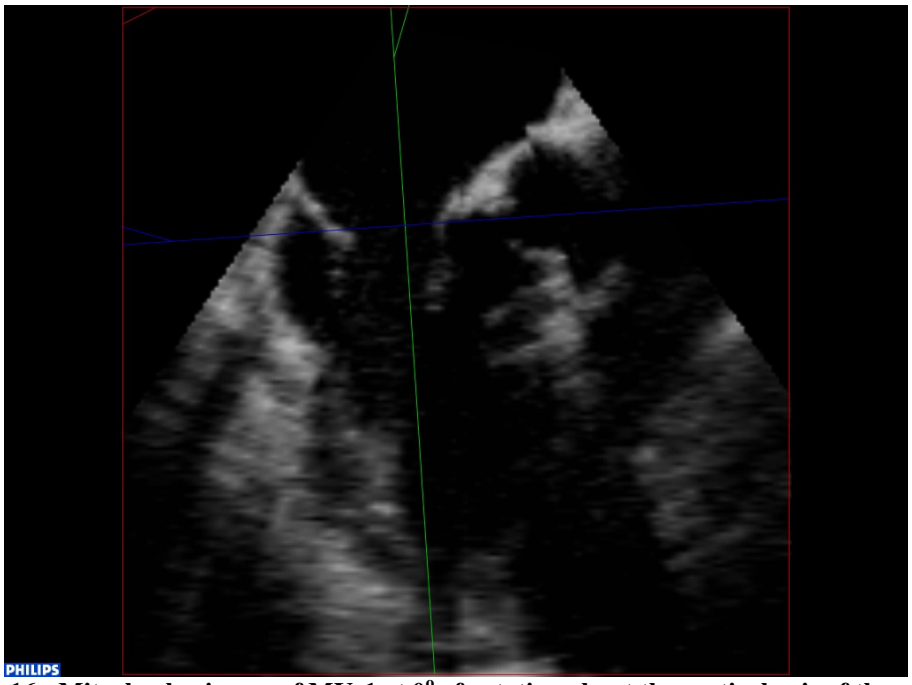

Figure 16 - Mitral valve image of MVs1 at 0^o of rotation about the vertical axis of the mitral valve, indicated by the green line in the image.

4.2 Image Processing

The ultrasound images are processed in a MATLAB algorithm that allows the analyst to select the points of interest on the images. There are six possible points of interest to be selected on each image: two points for the location of the annulus (P_3 and P_4), two points for the free margin (P_5 and P_6), and one point each for the papillary muscle heads (P_7 and P_8), as denoted in Figure 17. A Cartesian coordinate system is defined for each image by selecting two points to define a vector from the intersection of the vertical and horizontal axes (P_1), and another point along the horizontal axis (P_2). Since each image is a cross-section rotated about the vertical (green) axis, this creates a

consistent coordinate system for all the images. Identification of the anatomical structures can be difficult with ultrasound images, so the videos the still images were extracted from were used to help with identification.

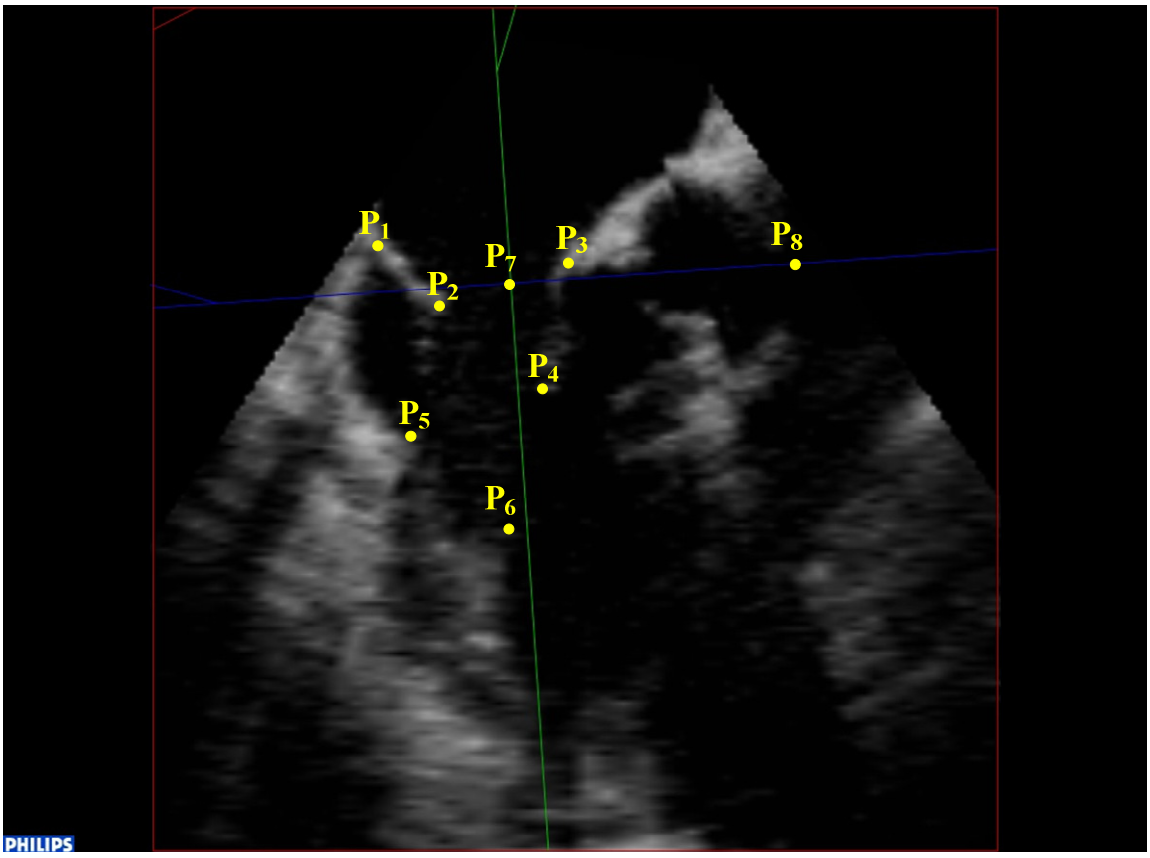

Figure 17 - Coordinates selected during image processing.

The coordinates obtained from each image are two dimensional and must then be converted to three dimensional for construction of the model. The angle θ in cylindrical coordinates is the angle at which the image was acquired, while the r and z values of point $P(x, y)$ relative to the origin, $P(x_7, y_7)$ are given by:

$$\begin{aligned} r &= -\cos(\alpha)(x - x_7) - \sin(\alpha)(y - y_7) - y_7 \\ z &= \sin(\alpha)(x - x_7) - \cos(\alpha)(y - y_7) \end{aligned} \tag{0.19}$$

where the angle α is the angle of the vector formed by points $P(x_7, y_7)$ and $P(x_8, y_8)$:

$$\alpha = \arctan \frac{\left(y_8 - y_7\right)}{\left(x_8 - x_7\right)} \tag{0.20}$$

The coordinates for each image are then saved into a text file for future use in constructing the finite element model.

4.3 Geometric Reconstruction

Once the geometric coordinates of the annulus, free margin, and papillary muscle heads have been acquired they are processed to construct the finite element model of the mitral valve. The processing is performed using a MATLAB program, herein termed the 'Processor,' which takes the coordinates as inputs and outputs the LS-DYNA input file.

4.3.1 Import Coordinates

The valve coordinates are stored in data files, one per angular orientation. The coordinates are given in cylindrical coordinates, in the form (θ, n, r, z) where θ, r, and z are the coordinate values, with θ in degrees, and n is the coordinate number within the data file (n = 1, 2, …, 6). Each data file contains six points in each cross-sectional image of the valve, labelled P_n in Figure 18. These coordinates are imported into the Processor into four arrays, denoted *A*, *FM*, *AP*, and *PP* for the Annulus, Free Margin, and Anterior and Posterior Papillary Muscles, respectively. Upon importation, the r and z coordinates are multiplied by a scaling factor f to convert the coordinates to a 1:1 scale ratio between the geometric model and the actual valve size. Next, the coordinates are converted from

the cylindrical coordinate system (r, θ, z) to the Cartesian coordinate system (x, y, z), where

$$x = r\cos\left(\frac{\theta \cdot \pi}{180}\right) \tag{0.21}$$

$$y = r\sin\left(\frac{\theta \cdot \pi}{180}\right) \tag{0.22}$$

$$z = z \tag{0.23}$$

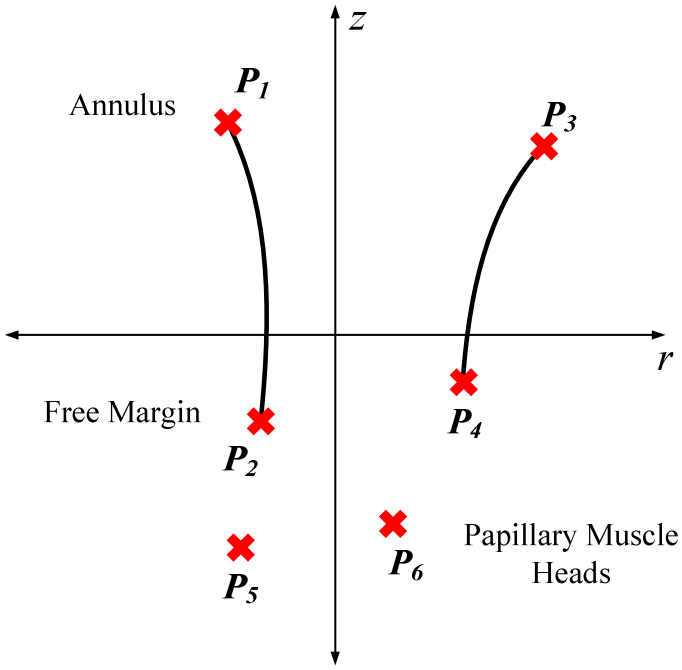

Figure 18 - Mitral valve cross-section at angle θ.

The scaling factor for the subject model was determined by measuring the annulus of the unscaled model and relating that to the length of a typical mitral valve, as the actual value of the subject's valve was not available. In LS-DYNA, the annulus length from commissure to commissure was measured as 253.415 mm and the same dimension of a typical mitral valve is 37.0 mm [49]. This gives a scaling factor of $f = {}^{37.0}\!/_{253.415} = 0.146$. The scaling factor for the patient model was determined in the same manner, except the actual dimension of the patient's annulus was used, 27.3 mm, measured in QLAB from commissure to commissure. The scaling factor was $f = {}^{27.3}\!/_{192.5} = 0.1418$.

4.3.2 Free Margin & Annular Shape Construction

The coordinates for the annulus and free margin provide a general outline of these two valve features, but do not provide a continuous shape. There are three steps to constructing the annulus and free margin. First, the initial shapes are defined by creating splines from the coordinates. These splines are then smoothed to remove irregularities in their shapes. Finally, the data points in the first splines are used to create a second set of splines for both features, with a high number of points along the spline, constituting the final shapes of the annulus and free margin.

4.3.2.1 Initial Shape

The initial shapes of the annulus and the free margin are created from the coordinates acquired from the ultrasound images using a cubic cardinal spline. The cubic cardinal spline is defined by

$$C_i(u) = \begin{pmatrix} c_1(u) & c_2(u) & c_3(u) & c_4(u) \end{pmatrix} \begin{pmatrix} p_{i-1} \\ p_i \\ p_{i+1} \\ p_{i+2} \end{pmatrix} \tag{0.24}$$

and

$$\begin{pmatrix} c_1(u) & c_2(u) & c_3(u) & c_4(u) \end{pmatrix} = \begin{pmatrix} u^3 & u^2 & u & 1 \end{pmatrix} \begin{pmatrix} -h & 2-h & h-2 & h \\ 2h & h-3 & 3-2h & -h \\ -h & 0 & h & 0 \\ 0 & 1 & 0 & 0 \end{pmatrix} \tag{0.25}$$

where p is the free margin/annulus points, u is the current interpolation point, h is the spline 'tension' and i is the current point . For each point along the annulus and free margin, a hundred points are interpolated between the point and adjacent points. The spline tension controls the shape of the spline and can be defined in the range of 0 to 1.

A tension of 0.9 creates a spline with large radius curves as desired. The initial application of the spline to the raw data creates irregularly shaped annular and free margin geometries (Figure 19). Data smoothing is used to eliminate these irregularities.

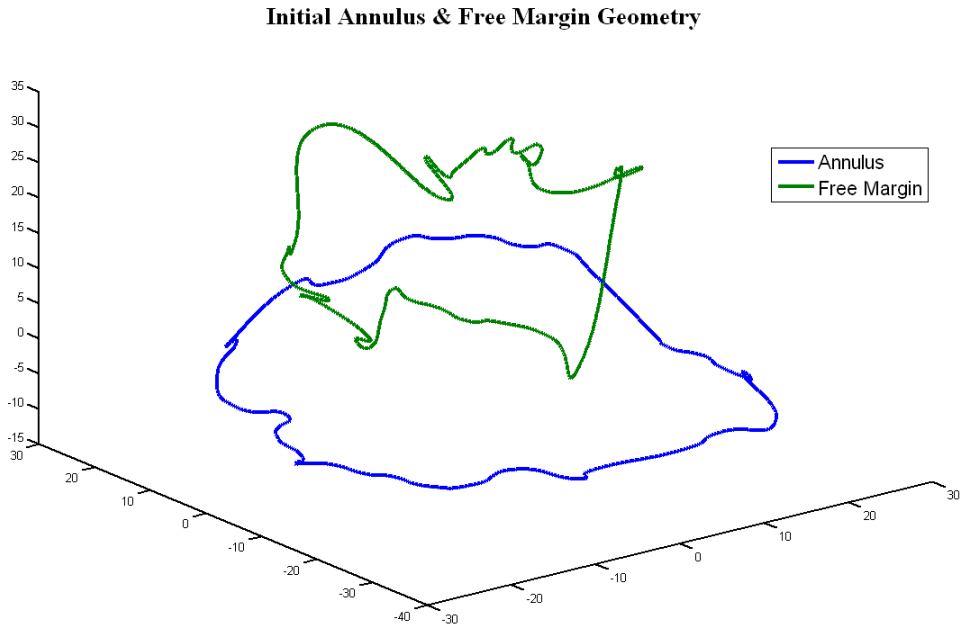

Figure 19 - Result of Application of Spline Algorithm to the Annulus and Free Margin Data.

4.3.2.2 Data Smoothing

The splines are simplified using a 7-point moving average data smoothing technique. A selection of eighty points is taken from the spline at regular intervals. The algorithm used for this assigns the points to an empty array using

$$C_{raw}(i) = C\left(i \cdot \frac{n}{sn}\right) \tag{0.26}$$

where C is the initial spline, i is the current point from 1 to 80, n is the number of points in the initial spline, and sn is the number of points being selected (80). The smoothed spline, shown in Figure 20, is given by

$$C_s(i) = \frac{\sum_{i-h}^{i+h} C_{raw}(i)}{2h+1} \tag{0.27}$$

where h is the number of points before and after the current point i (h=3).

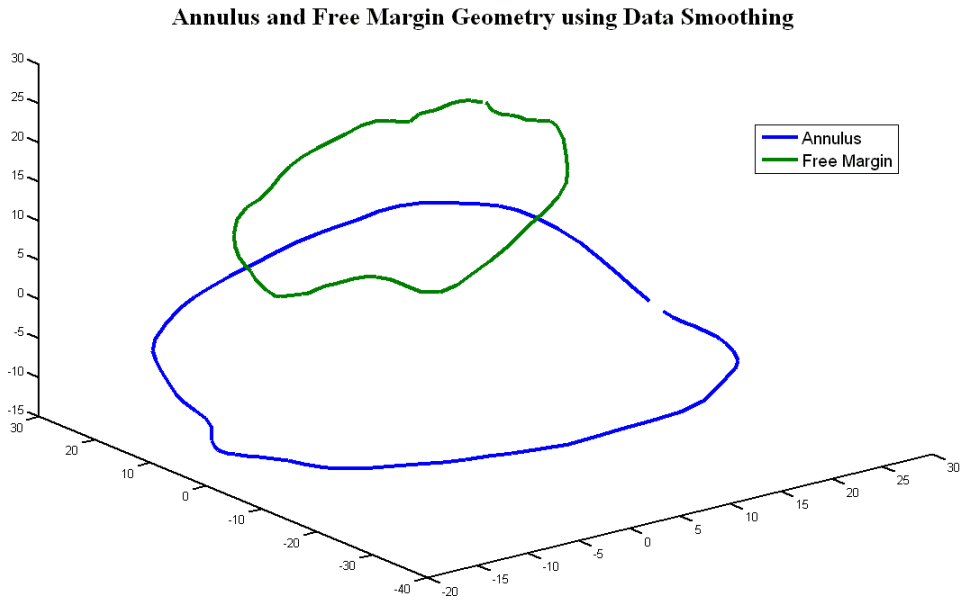

Figure 20 - Application of the 7-point moving average to the annulus and free margin.

4.3.2.3 Final Shape

The final shapes of the annulus and free margin are created from smoothed data points, using the same spline method described above, with 8000 points per spline. These shapes, shown below in Figure 21, are used to create the leaflets of the valve in further steps.

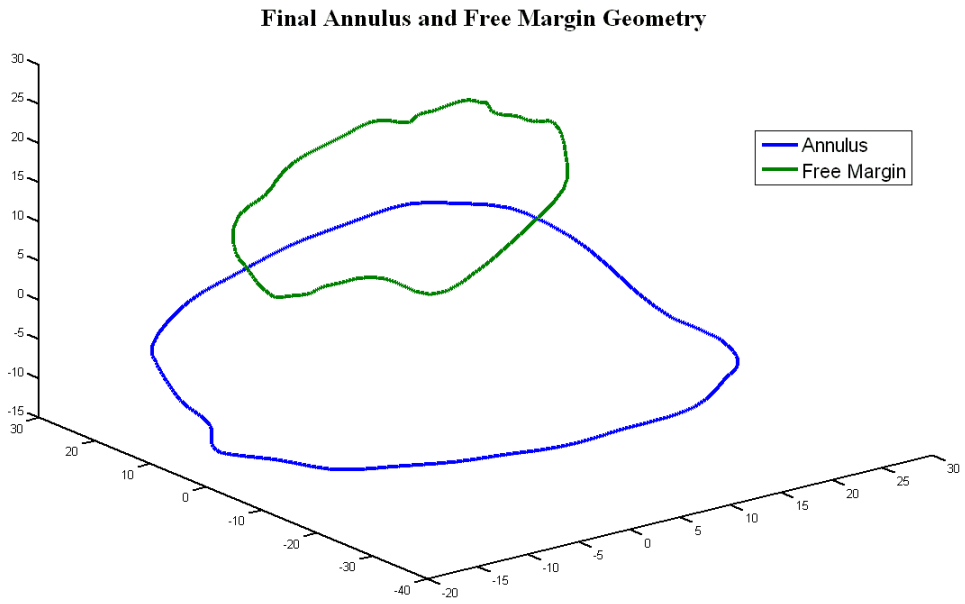

Figure 21 - Final annulus and free margin splines.

4.3.3 Papillary Muscle Head Creation

The anterior and posterior papillary muscle heads are created using a similar method as that used to create the annulus and leaflets. The data acquired from the ultrasound equipment consists of eighteen points each for the anterior and posterior sides of the valve. However, each muscle head is only represented by four or five points with the remaining points having null values. These null points are first eliminated from the data set, leaving only the points representing the muscle heads. In this model each muscle head is modelled as a spline created from the attachment points for the chordae tendinae.

4.3.3.1 Spline Generation

The same type of spline is used to create the muscle heads as for the annulus and free margin. Since a muscle head consists of an array of points and does not form a loop,

points must be created extending from each end of the array to create the spline. Given a set of points P_1, P_2… P_n, points P_0 and P_{n+1} are given by

$$\vec{l} = P_1 - P_2$$
$$P_0 = 1.1\vec{l} + P_1 \tag{0.28}$$

and

$$\vec{l} = P_n - P_{n-1}$$
$$P_{n+1} = 1.1\vec{l} + P_n \tag{0.29}$$

These new points P_o and P_{n+1} are shown in Figure 22 as the inserted points, which enable the application of the spline. A spline is then created from the data representing the muscle heads. As the two new points are only used for the spline function, they are removed from the final geometry, shown in Figure 23 with the annulus and free margin. The papillary muscle heads are then discretized at a later step.

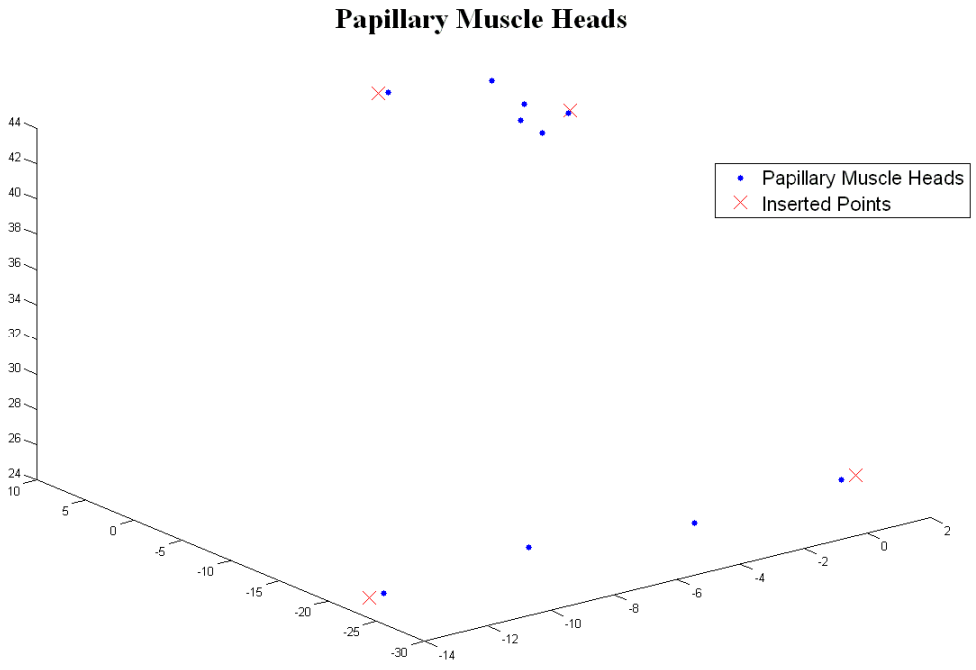

Figure 22 - Insertion of points at each end of the papillary muscle heads.

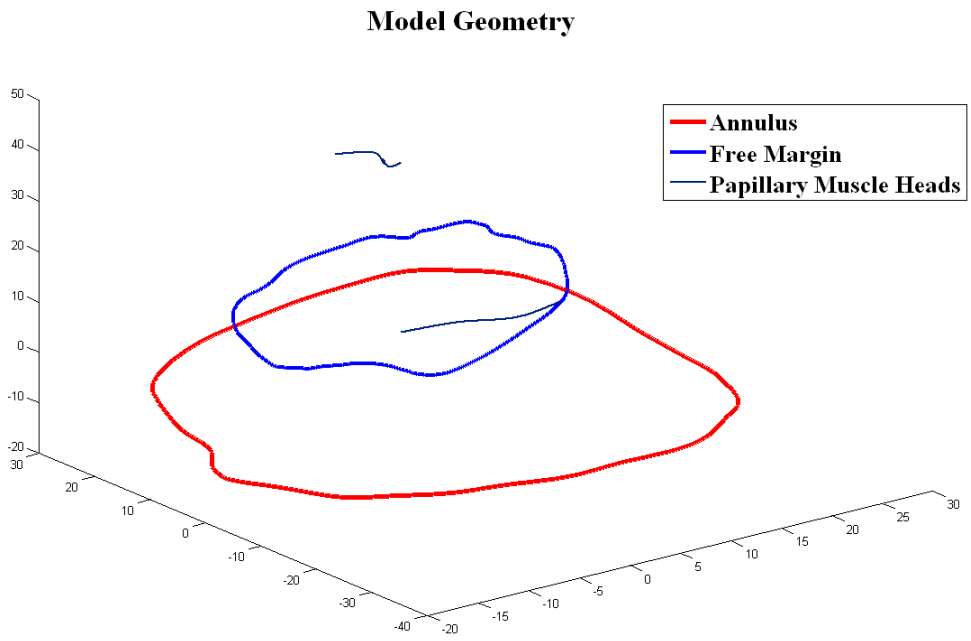

Figure 23 - Final geometry for the papillary muscle heads, annulus, and free margin.

4.3.4 Definition of Posterior and Anterior Leaflets

The two mitral valve leaflets must be differentiated from each other in the model due to their different material properties. In the valve, the points where the two leaflets join are at the commissures, but these points are difficult to identify in the model and ultrasound images. The commissures typically correspond to the widest point of the annulus and to the locations of the papillary muscle heads. In this model, the widest point of the annulus is used as a starting point to find the commissures. The widest point of the annulus is found automatically using an algorithm to search the annulus spline for the two points with the largest distance between them. For each point P_i (with $i = 1, \ldots, n$), the distance is calculated between P_i and P_j (with $j = 1, \ldots, n$) by

$$d = \left| P_j - P_i \right| \tag{0.30}$$

and

$$d_{\max} = \max\left(\left|P_j - P_i\right|\right) \tag{0.31}$$

where n is the number of points in the spline. For example, for MVs1 all points between P_{2471} and P_{6431} form the posterior leaflet; all other points form the anterior leaflet. The material flags for these points are set to: m = 1 for the posterior and m = 2 for the anterior leaflet. The commissure locations for MVs1 are shown in Figure 24.

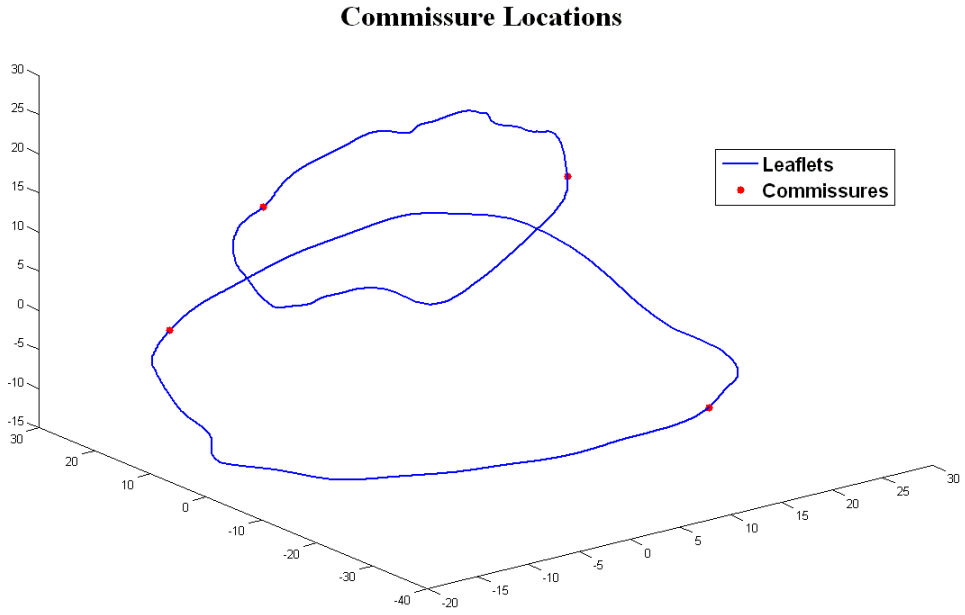

Figure 24 - Approximate commissure locations marked on the annulus and free margin.

4.3.5 Creation of Leaflet Thickness

At this point, the leaflets do not have any thickness, whereas the thickness of a typical mitral valve leaflet is 0.55 mm [31]. The model is modified to attribute this dimension to the valve by creating new splines along the previous splines: a spline on the atrial side and a spline on the ventricle side for both the annulus and free margin. On the annulus, each point, P_i^a, its adjacent points P_{i-1}^a and P_{i+1}^a, and its corresponding point on the free margin, form the vectors

$$\vec{r}_1 = P_{i+1}^a - P_{i-1}^a \tag{0.32}$$

$$\vec{r}_2 = P_i^{fm} - P_i^a \tag{0.33}$$

Using these two vectors, the thickness dimension is created in the inner and outer directions by

$$\vec{r}_{3_{outer}} = \vec{r}_2 \times \vec{r}_1 \tag{0.34}$$

$$\vec{r}_{3_{inner}} = \vec{r}_1 \times \vec{r}_2 \tag{0.35}$$

with unit vectors

$$\vec{u}_{outer} = \frac{\vec{r}_{3_{outer}}}{\left|\vec{r}_{3_{outer}}\right|} \quad \text{and} \quad \vec{u}_{inner} = \frac{\vec{r}_{3_{inner}}}{\left|\vec{r}_{3_{inner}}\right|} \tag{0.36}$$

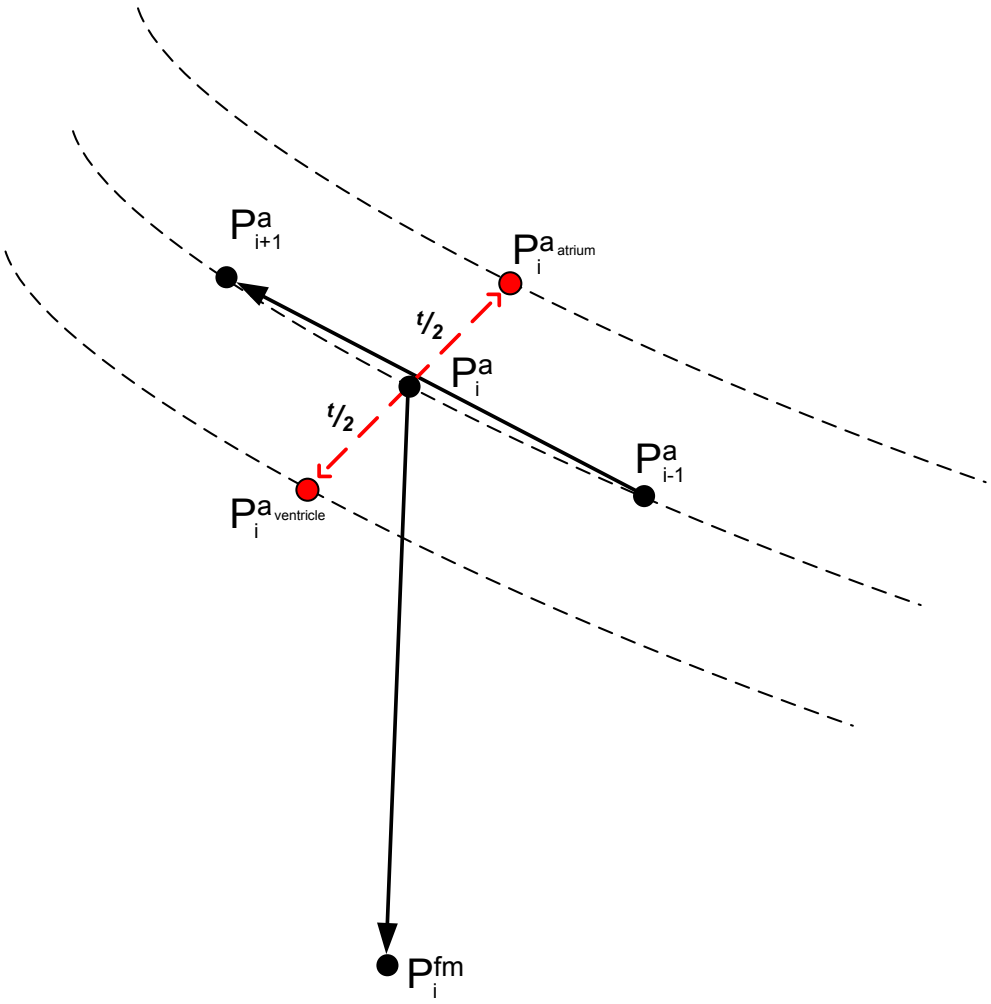

Figure 25 - Definition of the thickness dimension for the model.

Finally, the coordinates of the new splines are given by

$$P_i^{a_{outer}} = \tfrac{t}{2}\vec{u}_{outer} + P_i^a \quad \text{and} \quad P_i^{a_{inner}} = \tfrac{t}{2}\vec{u}_{inner} + P_i^a \tag{0.37}$$

for a thickness t (Figure 25). The same method is used to create the thickness dimension for the free margin.

4.3.6 Nodes

4.3.6.1 Leaflet Discretization

4.3.6.1.1 Annulus and Free Margin Nodes

4.3.6.1.1.1 Number of Nodes

The first step in discretizing the leaflets is to determine the number of nodes required for the annulus and free margin. The number of nodes depends on the desired element size, which can vary. The number of nodes is found simply by dividing the approximate length of the annulus by the element size

$$N = \left\lfloor \frac{L_a}{e_{size}} \right\rfloor \tag{0.38}$$

where $\lfloor \ \rfloor$ means floor to the next lowest integer and where the annulus length is

$$L_a = \sum_{i=1}^{n-1} \left(P_{i+1} - P_i \right) \tag{0.39}$$

where n is the number of points along the annulus. The two commissure points on the annulus must be nodes, therefore the nodes are divided between the posterior and anterior leaflets, such that

$$N_{anterior} = \frac{n_{anterior}}{n_{annulus}} \cdot N \tag{0.40}$$

and

$$N_{posterior} = N - N_{anterior} \tag{0.41}$$

where $n_{anterior}$ is the number of points forming the anterior section of the annulus and $n_{annulus}$ is the number of points along the annulus.

4.3.6.1.1.2 Node Creation

Nodes are created along the annulus and free margin by selecting points along the two splines at regular intervals starting and ending at the commissures. These intervals, h_p and h_a, are a ratio of the number of points in the anterior and posterior sections of the splines to its number of nodes, floored:

$$h_p = \left\lfloor \frac{n_{posterior}}{N_{posterior}} \right\rfloor \quad \text{and} \quad h_a = \left\lfloor \frac{n_{anterior}}{N_{anterior}} \right\rfloor \tag{0.42}$$

4.3.6.1.2 Radial Nodes

4.3.6.1.2.1 Number of Nodes

The number of nodes required to connect the annulus to the free margin in the radial direction is variable, depending on the size of the element. The number of nodes was varied experimentally until a ratio of 1:1 was obtained for a given element size. This was done by creating the model and measuring a specific element in LS-DYNA.

4.3.6.1.2.2 Node Creation

The nodes connecting the annulus to the free margin are created by first creating vectors connecting each node on the free margin to each node on the annulus, given by

$$\vec{l}_i^{\,s} = FM_i - A_i \tag{0.43}$$

where s = inner, outer, or middle spline, FM and A are the points of free margin and annulus nodes, and $i = 1, \ldots, n$. Each new node is calculated by adding the annulus point A_i to a factor of the vector:

$$R_j^s = \frac{j}{N_r+1}\vec{l}_i^{\,s} + A_i \tag{0.44}$$

where N_r is the number of nodes across the leaflet for each set of two points and $j = 1, \ldots, N_r$.

4.3.6.1.3 Brick Elements

The valve leaflets are modelled using two layers of brick elements, which are hexahedra with eight nodes. Two layers of elements are used as they can handle bending in the leaflets better than only one layer. LS-DYNA being an explicit solver, best results are obtained with shape functions described by polynomials of low order. In addition, the material properties to be implemented require a solid element. Therefore the ELEMENT_SOLID linear brick element is used and the node numbering convention for the element's nodes is as shown in Figure 26.

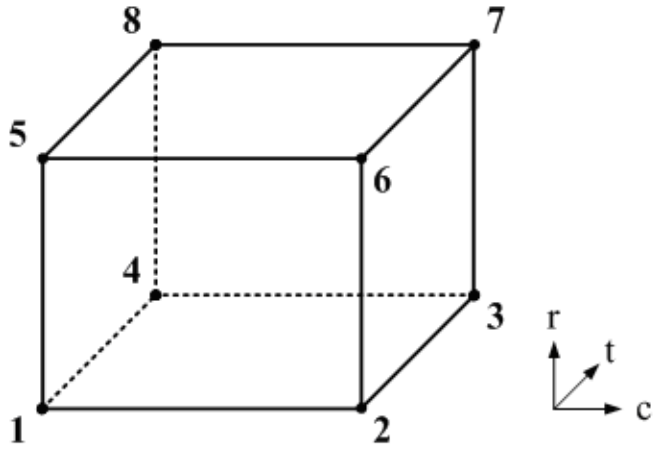

Figure 26 - Brick element node numbering (coordinate system: r = radial direction, c = circumferential direction, and t = thickness direction of the leaflets).

The leaflets are discretized into brick elements using an algorithm to sequentially create each element from the set of leaflet nodes. The algorithm starts from the first node, located on the inner edge, or atrium side, of the annulus, creating a row of elements along the annulus. Discretization progresses to the next row of elements, until the free margin is reached, at which point the inner layer of elements has been created. The process starts at the annulus again for the second layer of elements, the ventricle side of the leaflets. Element numbering for each layer was stored in an array, E_x^{inner} and E_x^{outer}, with nodes N_1 to N_8 numbered automatically by the equations:

$$E_x^{inner} = \begin{bmatrix} N_1 \\ N_2 \\ N_3 \\ N_4 \\ N_5 \\ N_6 \\ N_7 \\ N_8 \end{bmatrix}^{\mathrm{T}} = \begin{bmatrix} jb+i \\ (j+1)b+i \\ (j+1)b+i+1 \\ jb+i+1 \\ jb+i+n_l \\ (j+1)b+i+n_l \\ (j+1)b+i+n_l+1 \\ jb+i+n_l+1 \end{bmatrix}^{\mathrm{T}} \tag{0.45}$$

and

$$E_x^{outer} = \begin{bmatrix} jb+i \\ (j+1)b+i \\ (j+1)b+i+1 \\ jb+i+1 \\ jb+i+n_l \\ (j+1)b+i+n_l \\ (j+1)b+i+n_l+1 \\ jb+i+n_l+1 \end{bmatrix}^{\mathrm{T}} + n_l \tag{0.46}$$

where x is the element number, $i = 1, \ldots, b$, $j = 1, \ldots, n_r$, b is the number of nodes along the annulus in each layer of nodes, and n_l is the number of nodes in one layer. The number of nodes per layer is calculated from the number of radial nodes, n_r, by

$$n_l = (n_r + 2)b \tag{0.47}$$

The element numbers (x) range from 1 for the first element, increasing by increments of one for each subsequent brick element created.

4.3.6.2 Chordae Tendinae Discretization

The chordae tendinae are modelled using beam elements, so nodal discretization requires two nodes per element. At a point midway between the papillary muscles and the free margin, the tendinae are branched from one element into three elements. So for each tendinae, there is one node on the papillary muscle head, one midway between the papillary muscle and free margin, and three nodes on the free margin.

4.3.6.2.1 Papillary Muscle Head Nodes

The papillary muscle heads serve as an anchor point for the chordae tendinae, so the muscle heads are discretized with a number of nodes equal to the number of chordae. For the mitral valve, the number of chordae per muscle head is 12 on average [50]. Thus, the papillary muscle heads is divided into 12 nodes each. To determine the coordinates of these nodes, the length of each papillary muscle is calculated from

$$L_{pm} = \sum_{i=1}^{n-1} \left\| P_{i+1} - P_i \right\| \tag{0.48}$$

where P_x are the points forming the papillary muscle splines and n is the number of points. The first and last points on the spline each form nodes. The intermediary nodes are found by iteratively calculating the distance between a node and the next point along the spline (l_d) is summed until the set length between nodes (l_n) is reached. The distance between node $N_{pm,j}$ with point P_j and the next point is given by

$$l_{d_j} = \sum_{i=j}^{n} \left\| P_{i+1} - P_i \right\| \quad \text{while} \quad l_{d_j} \leq l_n \tag{0.49}$$

where the length l_n is given by

$$l_n = \frac{L_{pm}}{N_c} = \frac{L_{pm}}{12} \tag{0.50}$$

When l_n is reached, a new node $N_{pm,j+1}$ is defined as the point P_i and the algorithm is repeated starting from the new node, until all nodes are defined.

4.3.6.2.2 Chordae-to-Free Margin Attachment Nodes

The next step in constructing the chordae is to find the nodes where they attach to the free margin. Each chordae requires three nodes on the free margin due to the branched structure of the tendinae. Since a real chordae tendinae attaches across the entire thickness of the leaflet, attaching the elements at the midway point of the thickness offers a better approximation of this than attaching at either edge. The middle row of free margin nodes is used, since it is midway across the thickness of the leaflet.

The first step in identifying the chordae-free margin nodes is to find the commissure nodes, P_{c1} and P_{c2}, since chordae attachment is centred on these two nodes. A simple search algorithm, described in section 4.3.4, is used to identify these two points. Next, nodes along the free margin, moving outwards on either side of the commissures, are selected and assigned as chordae tendinae nodes. The chordae nodes are identified from the set of free margin nodes, N_{fm}, for each commissure, by the algorithm:

$$
\begin{aligned}
&\text{if } \left(i + P_c - \left(\tfrac{3n_c}{2} + 1\right) - x\right) > n_{fm} \\
&\quad N_C(i) = N_{fm}\left(i + P_c - \left(\tfrac{3n_c}{2} + 1\right) - n_{fm}\right) \\
&\text{if } \left(i + P_c - \left(\tfrac{3n_c}{2} + 1\right) - n_{fm}\right) > 0 \text{ and } < 1 \\
&\quad N_C(i) = N_{fm}\left(i + P_c - \left(\tfrac{3n_c}{2} + 1\right)\right) \\
&\text{if } \left(i + P_c - \left(\tfrac{3n_c}{2} + 1\right) - n_{fm}\right) < 1 \\
&\quad N_C(i) = N_{fm}\left(i + P_c - \left(\tfrac{3n_c}{2} + 1\right) + n_{fm}\right)
\end{aligned}
\tag{0.51}
$$

where n_{fm} is the number of free margin nodes, n_c is the number of chordae tendinae (n_c = 12), P_c is the node number of the commissure (P_{c1} and P_{c2}), and i = 1, …, $3n_c$. The free margin node number is saved in an array with the coordinates for the chordae nodes.

4.3.6.2.3 Chordae Branching Nodes

Creating the node where the single chordae tendinae branches into three parts is a simple process of finding the midway point between the papillary muscle head node and a free margin node. Each tendinae has a set of three nodes on the free margin, for which the middle of the three nodes ($N_{c,m}$) forms a vector with the muscle head node

$$\vec{r} = N_{c,m} - N_{pm} \tag{0.52}$$

Therefore, the node at which the chordae tendinae branches is given by

$$N_{c,b} = 0.5\vec{r} + N_{pm} \tag{0.53}$$

and finalizes the discretization of the chordae tendinae, as shown below in Figure 27.

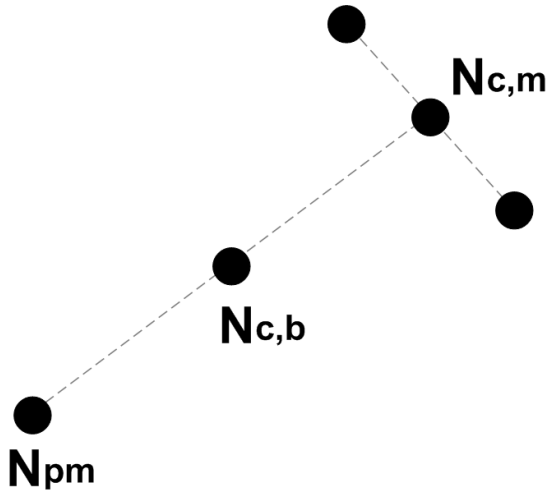

Figure 27 - Chordae Tendinae Nodes

At this point, all nodes necessary for constructing a 3D model of the mitral valve are defined, as shown in Figure 28, and may be connected to form elements.

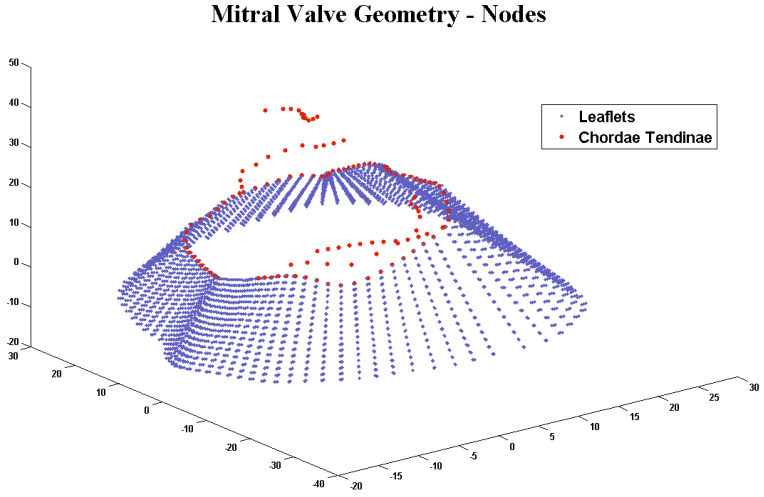

Figure 28 - Mitral valve model created from nodes.

4.3.6.2.4 Beam Elements

The chordae tendinae are modeled using the ELEMENT_BEAM two node beam element in LS-DYNA, combined with the MAT_CABLE_DISCRETE_BEAM material property, which, in effect, transforms the element into an elastic rod that can only take tension (all bending moments are zero, and no force develops in compression). The chordae

elements connected to the papillary muscle heads are created first and stored in an array $E_w^{chordae}$, such that

$$E_w^{chordae} = \begin{bmatrix} N_1 \\ N_2 \end{bmatrix}^{\mathrm{T}} = \begin{bmatrix} n_l + w \\ n_l + w + 24 \end{bmatrix}^{\mathrm{T}} \tag{0.54}$$

where w is the beam element number, n_l is the number of nodes in each layer of nodes of the leaflets, and 24 is the number of chordae tendinae. The chordae elements connected to the free margin are defined as

$$E_w^{chordae} = \begin{bmatrix} N_1 \\ N_2 \end{bmatrix}^{\mathrm{T}} = \begin{bmatrix} N_{fm} \\ n_l + 24 + j \end{bmatrix}^{\mathrm{T}} \tag{0.55}$$

where N_{fm} is the node number of the free margin node, j = 1, 2, …, 72, and w = 25, 26, …, 72.

4.4 Load and Boundary Conditions

4.4.1 Pressure Loading

The movement of the leaflets is a result of the fluid-structure interaction of the blood and the leaflets. The effect of the blood on the valve is simulated using the typical blood pressure in the left ventricle over the cardiac cycle. The blood pressure of a normal, healthy individual is well documented and obtained from a Wiggers Diagram (Figure 29). The key area of interest in the cardiac cycle is systole, where the pressure rapidly increases and decreases during contraction of the heart. Therefore, the cycle can be shortened by not applying the entire portion of diastole, where the pressure is low, saving computing resources. Data points, starting from just before systole to just after

systole, were collected from the Wiggers Diagram describing the pressure in the left ventricle, as plotted in Figure 30. The time frame of the cardiac cycle is scaled to 1/10th of the actual cycle time in order to reduce computation time, which has been found previously to provide accurate results [46], thanks to negligible inertial effects. The pressure is applied to the surface of the leaflet, using the LOAD_SEGMENT command.

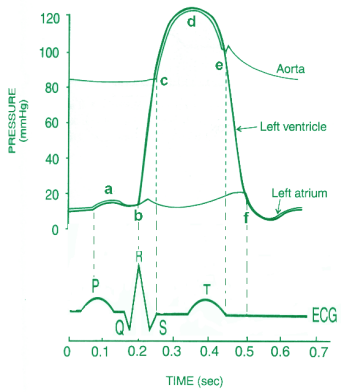

Figure 29 - Wiggers Diagram [51].

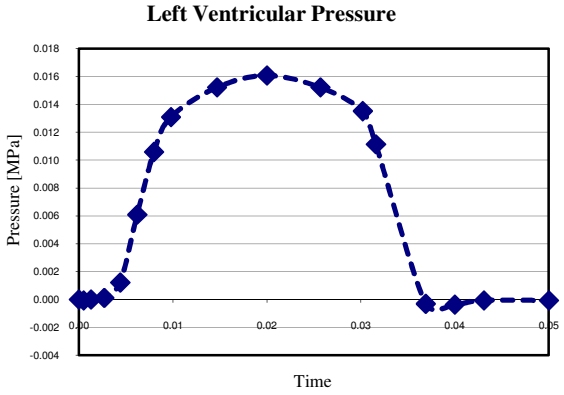

Figure 30 - Pressure in the left ventricle during the cardiac cycle.

4.4.2 Annular Displacements

The dimensions of the annulus change throughout systole. At the start of systole, the annulus begins to constrict, reaches its smallest size at the peak of systole, and returns to its original dimensions at the start of diastole. Measurements done by Dagum *et al.* determined the change in distance from commissure-to-commissure was 1.65 mm and the change in distance across the valve from anterior to posterior leaflets was 1.85 mm [49]. For simplicity, an average displacement of 1.75 mm is applied to the annulus. The displacement acts inwards to the centre of the valve in the plane of the annulus. Displacement of the annulus begins with systole, peaks in early systole, and returns to zero at the end of systole, as shown in Figure 31. The displacement is applied to the nodes of the annulus using the BOUNDARY_PRESCRIBED_MOTION_NODE card in

LS-DYNA, with a direction vector for each node pointing toward the centre of the annulus and the load curve set accordingly.

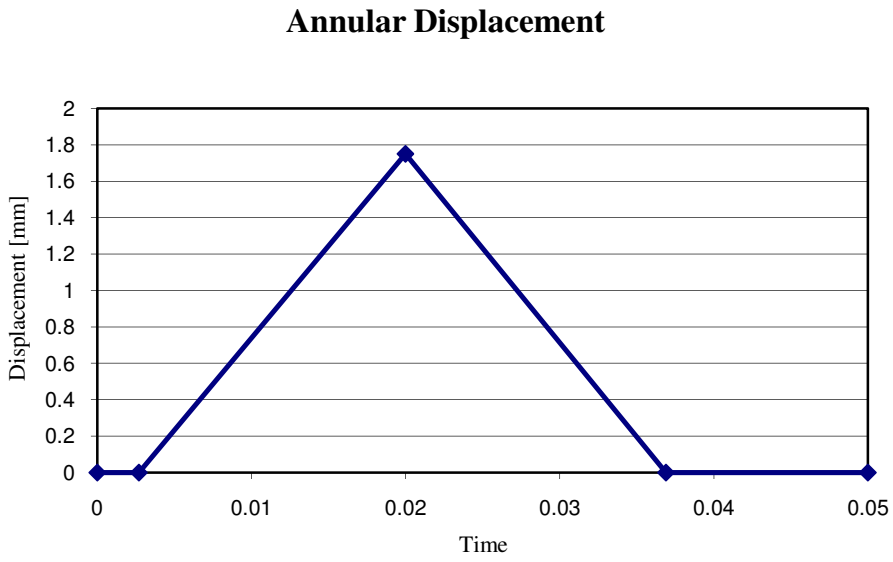

Figure 31 - Annular displacement over the cardiac cycle.

4.4.3 Papillary Muscle Head Constraints

According to Dagum *et al*. the motion of the papillary muscle heads relative to the mitral valve leaflets is minimal [49]. For simplicity, the papillary muscle heads are nodes fixed in position using the BOUNDARY_PRESCRIBED_MOTION_NODE card in LS-DYNA. The vector and load curve functions of the boundary condition card are both set to zero values, thereby fixing the papillary muscle head nodes in position for the duration of the analysis while allowing free rotation in all directions.

4.5 Exporting the Model from MATLAB to LS-DYNA

The final step in the process of constructing the FE model is creating an input file for the solver, LS-DYNA. Once all the nodes and elements are defined, the MATLAB

program prints all parameters of the model to one text file, ready for input into the solver. This file defines the control parameters, the material properties, the model parts (leaflets and chordae), the nodes and elements, and the boundary conditions. A sample input file, LSDYNA_input.txt, is included in the Appendix, along with the code for constructing the file.

Chapter 5

Modeling of Mitral Valve Repair

5 Modeling of Mitral Valve Repair

In cardiac surgery, a mitral valve repair entails restoring functionality to the valve of a patient by modifying its structure using various techniques. In this study, the analyst endeavours to apply these techniques to the model described in the previous chapter to develop a better method for simulating mitral valve repairs. These models use the same material properties, loading, and boundary conditions as the original model, with the goal of examining the dynamics of a repaired mitral valve. Three main categories of mitral valve repair are modeled: the annuloplasty ring, the Alfieri stitch, and the quadrangular resection. Furthermore, two forms of the Alfieri stitch are modeled: the double-orifice technique and the paracommissural technique. Each repair technique involves major changes in the geometry of the leaflets and a method was developed to model these changes in as natural a manner as possible. The original model is modified in a manner as closely resembling the way a surgeon would modify a real valve during surgery, using the dynamic FE solver LS-DYNA to manipulate the model.

5.1 Annuloplasty Ring

There are several types and models of annuloplasty ring available for use in mitral valve repair. In this study, a two dimensional, rigid model is created based on the Medtronic PROFILE 3D annuloplasty ring shown in Figure 32. The model consists of a set of points defining the shape of the ring, to which the annulus of the mitral valve model is fitted.

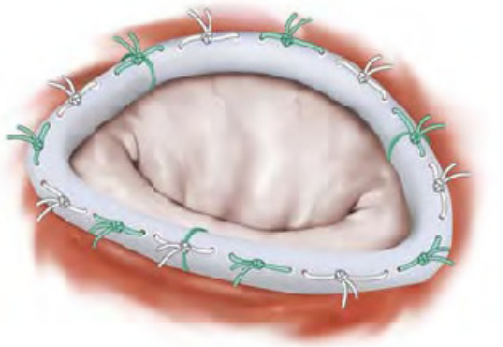

Figure 32 - Sketch of a Medtronic PROFILE 3D Annuloplasty Ring sutured to the annulus of a mitral valve.

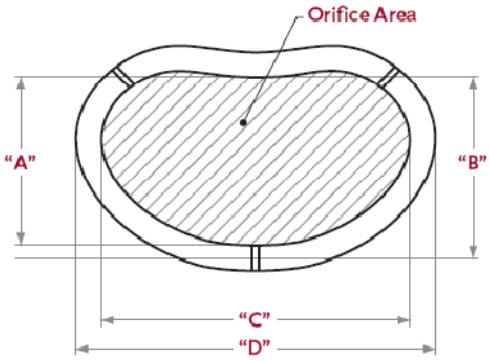

Figure 33 - Geometry of the Medtronic PROFILE 3D Ring.

The first step in creating the model was to process the diagram shown in Figure 33 using the image analysis program UTHSCSA ImageTool. The inner and outer lines of the ring were traced using points along the lines, for which the x-y coordinates were saved and exported. Two reference points were also found, defining the dimension "A" in the diagram above. The coordinates for the outer ring, inner ring, and reference points were imported into MATLAB to be processed (Figure 34).

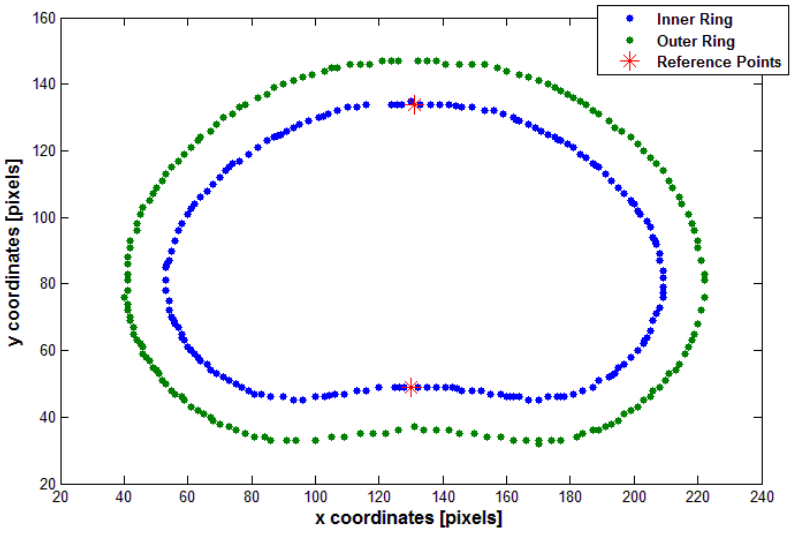

Figure 34 - Raw data for annuloplasty ring model, in MATLAB.

Next, splines were created from points of the inner and outer rings using the algorithm described in Chapter 4, which smoothed the shape of the rings by interpolating new

points, increasing the number of points by a factor of one hundred. A fifty-point moving average was applied to both splines, further smoothing the data, using the same method used in Chapter 4 and decreasing the number of data points to twenty times that of the raw data. A midline was created between the inner and outer rings by multiplying the x- and y-coordinates of each point on the outer ring by scale factors of S_x=0.94 and S_y=0.89 (Figure 35). The centre of the ring, P_c, was calculated as the midpoint between the reference points denoting the dimension "A." The centre point was then subtracted from all points on the inner, mid, and outer rings, as well as the reference points, to translate the model to the origin. Additional reference points were found on the rings to facilitate measuring the dimensions indicated in Figure 33.

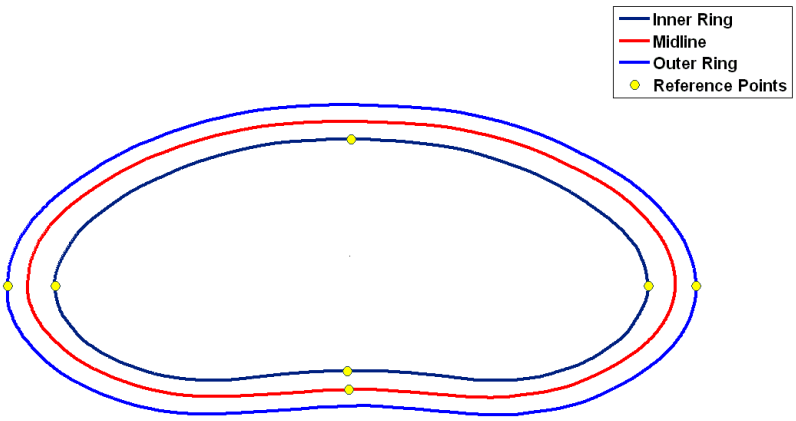

Figure 35 - Midline of annuloplasty ring.

Since the dimensions A, B, C, and D shown in Figure 33 are available from Medtronic for each available ring size, they can be applied to the model. A ring size of 24 is chosen, since it would most closely fit the annulus size of the mitral valve model, with the actual dimensions from the manufacturer given in Table 3. The model was scaled to the manufacturer's dimensions by first measuring the corresponding dimension in MATLAB.

For each dimension, a scale factor (sf_X) was calculated using a ratio of the actual dimension divided by the MATLAB model's dimension:

$$sf_X = \frac{X_a}{X_m} \tag{0.56}$$

where X_a is the actual dimension and X_m is the MATLAB model dimension. The coordinates of the inner, middle, and outer rings were scaled by multiplying the X and Y values by the scale factors as follows:

$$\begin{aligned} P_f^{inner} &= \left(sf_C \cdot x_i^{inner}, \quad sf_A \cdot y_i^{inner} \right) \\ P_f^{mid} &= \left(sf_{CD} \cdot x_i^{mid}, \quad sf_B \cdot y_i^{mid} \right) \\ P_f^{outer} &= \left(sf_D \cdot x_i^{outer}, \quad sf_B \cdot y_i^{outer} \right) \end{aligned} \tag{0.57}$$

Table 3 - Dimensions for the Annuloplasty Ring

Dimension	Actual [mm]	Model [mm]	Scale Factor	Final Model [mm]	Error [%]
A	13.4	85.2038	$sf_A = 0.1573$	13.4	0
B	15.0	92.0781	$sf_B = 0.1629$	14.76	1.6
C	24.2	155.6612	$sf_C = 0.1555$	24.2	0
D	30.5	180.7895	$sf_D = 0.1687$	30.5	0
CD_{avg}			$sf_{CD} = 0.1621$		

The final model dimensions were taken at the new equivalent reference points on the inner, outer, and middle rings. The dimensions A, C, and D were precisely those of the actual size 24 annuloplasty ring. However, the vertical dimension B showed a small margin of error, 1.6%, due to the fact that the two points forming this metric are multiplied by different scale factors. This margin of error is acceptable, since it scales the midline ring quite well and is based on the same method of calculation as the other scale factors. The final ring shape is shown in Figure 36, from which the midline ring is used to shape the annulus of the mitral valve models.

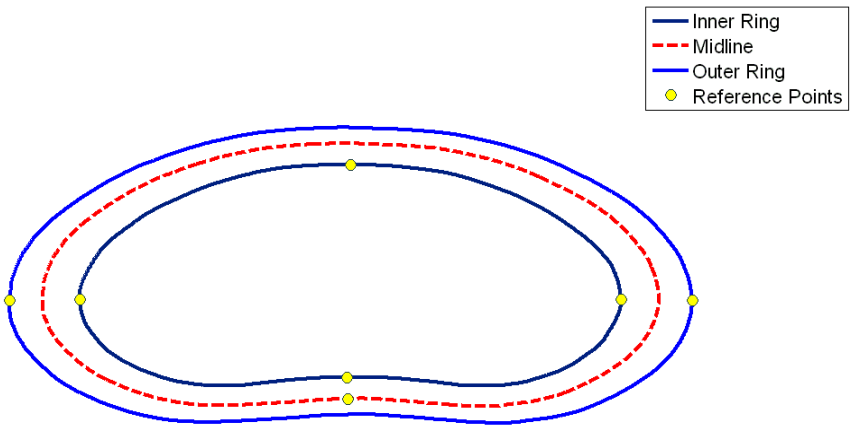

Figure 36 - Final annuloplasty ring

In the 3D model of the mitral valve the annulus does not lie in a plane parallel to the xy-plane, unlike the annuloplasty ring model. Therefore, the ring was fitted to the annulus by visual inspection in the following manner. First, the midline of the annuloplasty ring was rotated about the y and z axes using the rotation matrices R_y and R_z:

$$R_y = \begin{bmatrix} \cos(-\theta_y) & 0 & \sin(-\theta_y) \\ 0 & 1 & 0 \\ -\sin(-\theta_y) & 0 & \cos(-\theta_y) \end{bmatrix} \text{ and } R_z = \begin{bmatrix} \cos(\theta_z) & -\sin(\theta_z) & 0 \\ \sin(\theta_z) & \cos(\theta_z) & 0 \\ 0 & 0 & 1 \end{bmatrix} \tag{0.58}$$

where θ_y = 7° and θ_z = -102°. The ring was then translated in the x-direction by 3 mm to centre the ring at the centre of the annulus. It was also translated in the z-direction by 4.4 mm to raise the ring to the plane formed by the annulus. The rotations and translations were applied to all i points of the midline ring as follows

$$P_{step1_i} = R_z P_i^T \tag{0.59}$$

$$P_{step2_i} = R_y {P_{step1_i}}^T \tag{0.60}$$

$$P_{final_i} = \left[x_{step2_i} + 3, \quad y_{step2_i}, \quad z_{step2_i} + 4.4 \right] \tag{0.61}$$

The resulting set of points P_{final} is the final model of the annuloplasty ring. At this point, the ring has been fitted to the annulus of the mitral valve finite element model, as shown in Figure 37.

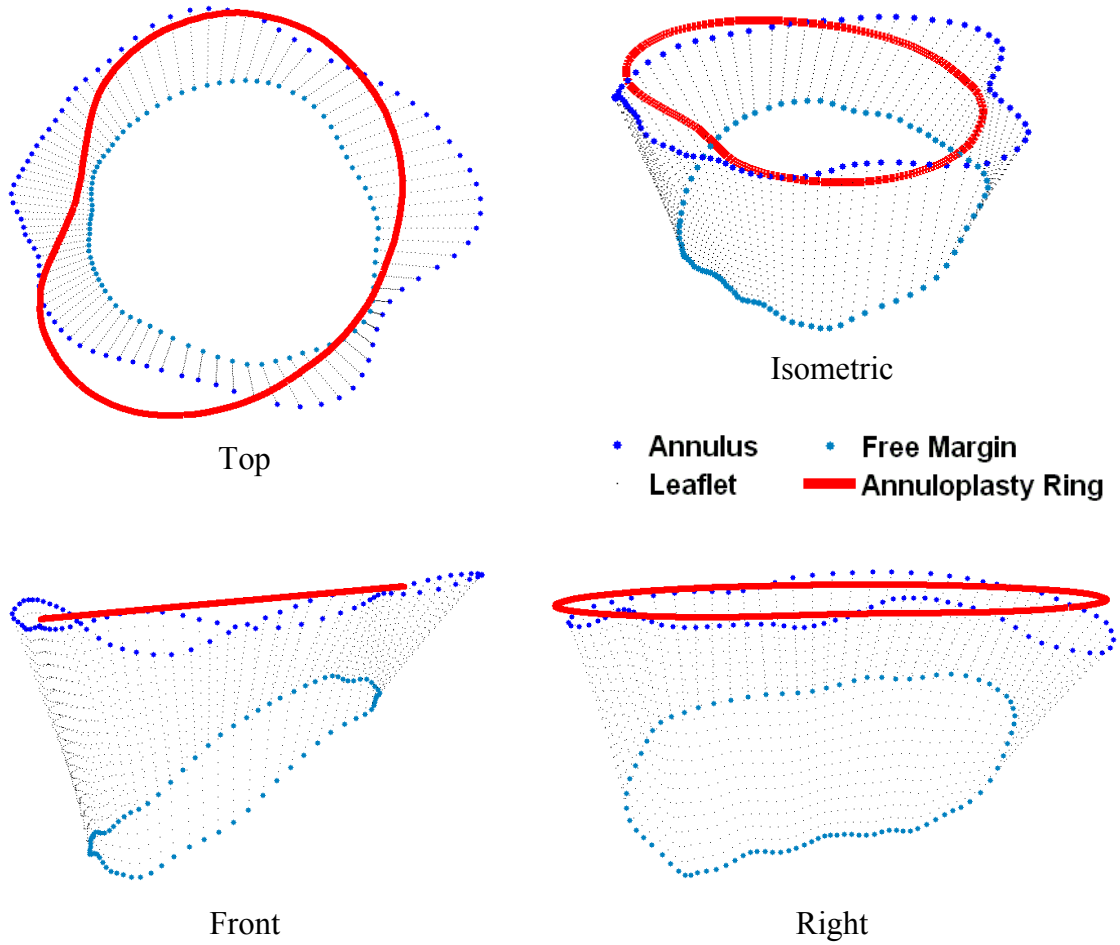

Figure 37 - Multiple views of the annuloplasty ring fitted to the annulus of the mitral valve model.

Now that the ring is in position, the shape of the annulus is modified to that of the ring. For each node i on the inner edge of the annulus, the point closest to it on the ring is determined by iteratively calculating the minimum distance d_{min} such that

$$d_{\min_i} = \min \left| P_{ring_j} - P_{node_i} \right| \text{ for } j = 1,...,n \text{ and } i = 1, ..., m \qquad (0.62)$$

where n is the number of points in the ring and m is the number of nodes. For each node, d_{min} and P_{ring} are saved for use in the LS-DYNA input file. Nodal displacements are used for each of the nodes on the inner edge of the annulus to shape the annulus into the form of the annuloplasty ring. The BOUNDARY_PRESCRIBED_MOTION_NODE keyword

is added to the original mitral valve LS-DYNA input file used in Chapter 4, with d_{min} as the displacement in the load curve and the load vector given by

$$\vec{R}_i = P_{ring_i} - P_{node_i} \quad \text{for } i = 1, ..., m \tag{0.63}$$

The boundary condition which controls the dilation of the annulus during the cardiac cycle is removed, along with the pressure loads applied to the leaflets. The analysis time was set to 0.06 s. Once the analysis was complete, with the annulus reshaped as shown in Figure 38, all of the node coordinates were exported from LS-DYNA. The coordinates were then added to a LS-DYNA input file with the load, boundary and material settings used for analysing the dynamics of the mitral valve over one cardiac cycle, as described in Chapter 4. During the geometry definition process, the (relatively low) stresses induced by the initial deformation of the leaflets to conform to the annulus ring were not carried over to the rest of the analysis, whereby representing a situation in which tissue remodeling has had time to occur and regularize stresses. In this study, the ring was applied to the Alfieri stitch and quadrangular resection models, as this is normal procedure in those types of repairs.

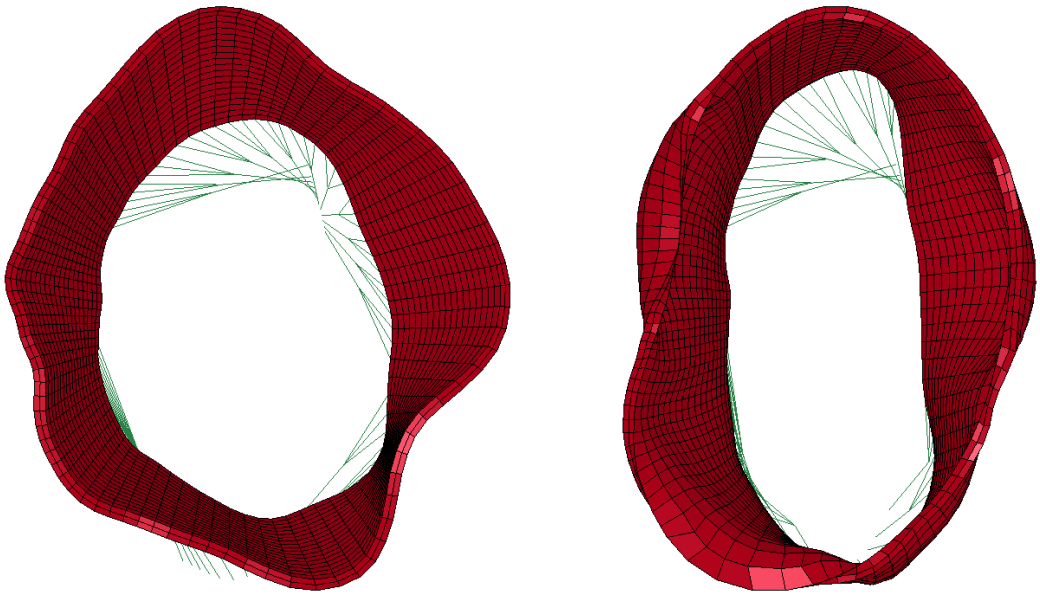

(a) (b)

Figure 38 - Mitral valve model (a) before and (b) after application of the annuloplasty ring model.

5.2 Alfieri Stitch

As illustrated in Figure 39, the Alfieri stitch involves joining two opposite edges of the free margin together. In the double-orifice Alfieri stitch, the free margin is stitched with sutures at the centres of the two leaflets, creating two smaller orifices for blood flow from the original, larger orifice. In the paracommissural Alfieri stitch, the free margin is stitched starting from one of the two commissures, moving towards the centre of the valve, decreasing the size of the orifice. The diagram in Figure 39 shows the sutured section of the free margin and the new orifices.

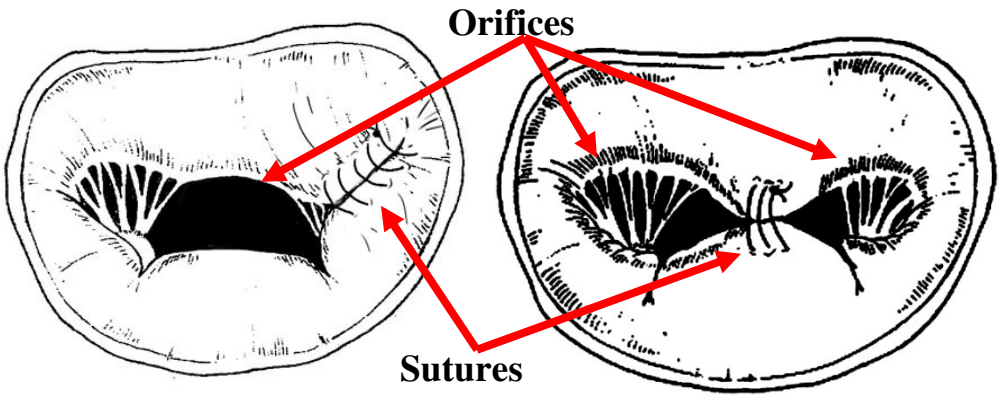

Figure 39 – Paracommissural (left) and Double-orifice (right) Alfieri Stitches [8].

The process for modeling this repair technique is the same for both double-orifice and paracommissural repairs. It starts with identifying the regions along the free margin of both leaflets where the leaflets are to be "stitched." Nodes were selected within these two regions on both the inner edge and the middle of the free margin, as shown in Figure 40.

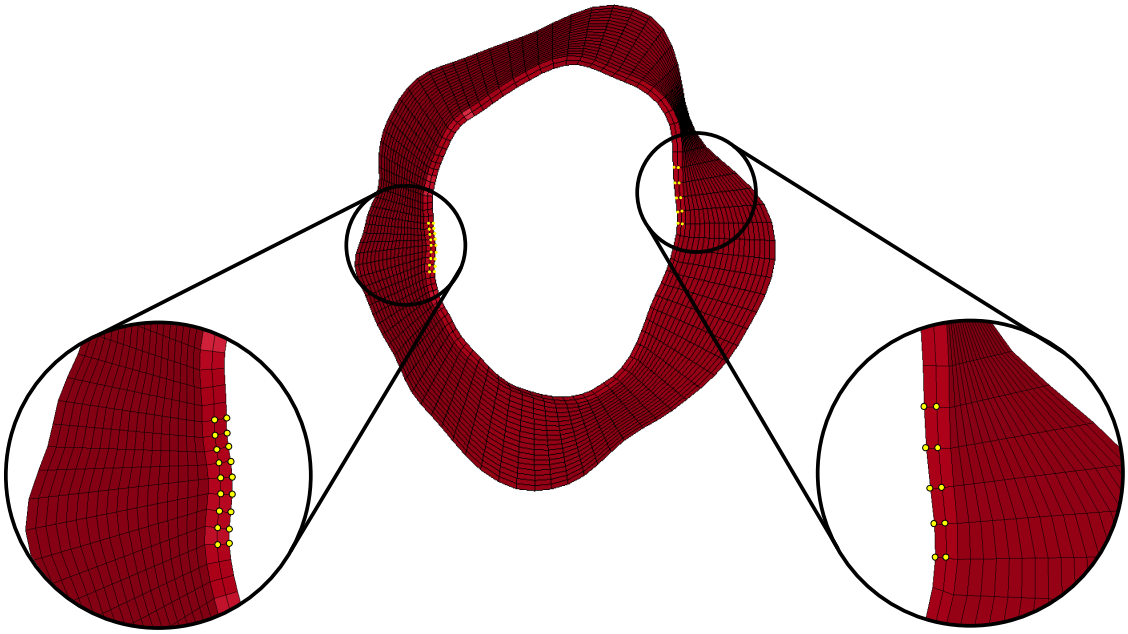

Figure 40 - Nodes selected on free margin in area to be stitched.

Each node selected on the anterior leaflet is paired with a node opposite it on the posterior leaflet. In the case where there are more nodes on one leaflet than on the other, a node is paired with the midpoint between two nodes on the opposite leaflet. In order to

bring the two regions together, nodal displacements are applied at the selected nodes. When analyzed, the nodal displacements draw the two leaflets together. Using two rows of nodes distributes the loads across the elements formed by the respective nodes, minimizing deformation of the element.

Given the coordinates of a node P_{a_i} on the anterior leaflet, and a node P_{p_i} on the posterior leaflet (see Figure 41), the magnitude (d) and direction ($\vec{R}_i$) of the displacement for that node is

$$\begin{aligned} \vec{R}_i &= P_{p_i} - P_{a_i} \\ d_{Ant_i} &= c_a \left| \vec{R}_i \right| - 0.05 \end{aligned} \tag{0.64}$$

where the constant 0.05 mm creates a small gap between the leaflets after the displacement. The displacement for the node at P_{p_i} is given as

$$d_{Post_i} = c_p \left| \vec{R}_i \right| - 0.05 \tag{0.65}$$

The displacements for the anterior and posterior leaflets are proportional to the constants c_a and c_p, respectively. For the double-orifice stitch the constants are $c_a = 0.92$ and $c_p = 0.08$. For the paracommissural stitch the constants are $c_a = 0.9$ and $c_p = 0.1$. The constants are designed to avoid uneven stretching in both leaflets and were determined by trial-and-error as those values which minimize the difference in the percent change in length of the two leaflets:

$$\% \text{ difference in lengths} = \left| \%\Delta_{Ant} - \%\Delta_{Post} \right| = \left| \frac{L_{Ant_{final}} - L_{Ant_{initial}}}{L_{Ant_{initial}}} - \frac{L_{Post_{final}} - L_{Post_{initial}}}{L_{Post_{initial}}} \right| \tag{0.66}$$

The lengths L were measured in LS-DYNA before and after application of the displacements, in the middle of the sutured regions. The percent difference in lengths for

the double-orifice stitch was 0.59 %, with a percent change of 13.64 % in the length of the anterior leaflet and 14.23 % in the length of the posterior leaflet. For the paracommissural stitch, the percent difference in lengths was 0.4259 %, with a percent change of 14.00 % in the length of the anterior leaflet and 13.56 % in the length of the posterior leaflet.

As for the annuloplasty ring, the BOUNDARY_PRESCRIBED_MOTION_NODE keyword was used to apply the nodal displacements to the leaflets. The load vectors for the selected nodes on the annulus were the direction ($\vec{R}_i$) and magnitude (d) given above. The direction vectors for each pair of nodes were opposite to each other, such that

$$\vec{R}_{a_i} = P_{p_i} - P_{a_i} \text{ and } \vec{R}_{p_i} = P_{a_i} - P_{p_i} \tag{0.67}$$

The analysis was performed over a time period of 0.085 s, which resulted in a maximum displacement rate of 185.6 mm/s based on the largest displacement. This displacement rate was found to be effective in maintaining the form of the brick elements.

Of note in Figure 41 is the lack of chordae tendinae. Although it would be ideal to include the tendinae in this step of the repair modelling, it was found that removing the tendinae for this step in constructing the repair model was necessary to prevent unnecessary deformation of the brick elements along the free margin. The chordae tendinae were reinserted in a later step. Also, a boundary condition was applied to the annulus, using the BOUNDARY_PRESCRIBED_MOTION_NODE function with zero degrees of freedom, to prevent annulus displacement.

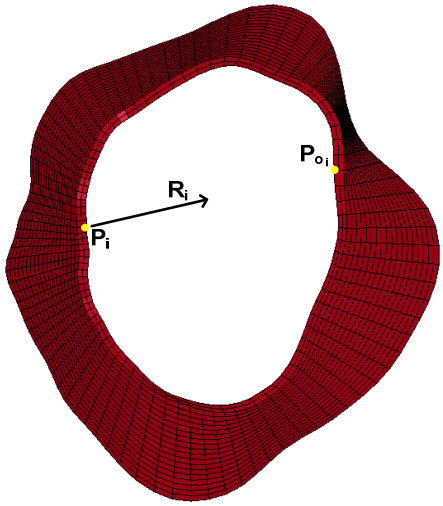

Figure 41 - Direction vector for nodal displacement.

Next, the model was analyzed in LS-DYNA 971. The key outcome of this step is to modify the free margin shape in a way that simulates what might actually occur during surgery. The results of this are shown in Figure 42, wherein the leaflets are pulled together at the centre. The positioning and shape of the remainder of the free margin has changed to form two new orifices. The advantage of using this method over others is the ability to change the shape of the orifice as a result of an applied load, due to the material properties of the leaflets, which is more realistic than using a numerical method to approximate an ideal geometry. The node coordinates for the results of this step are then exported and used to create a new LS-DYNA input file for dynamic analysis of the valve, with sutures connecting the leaflets.

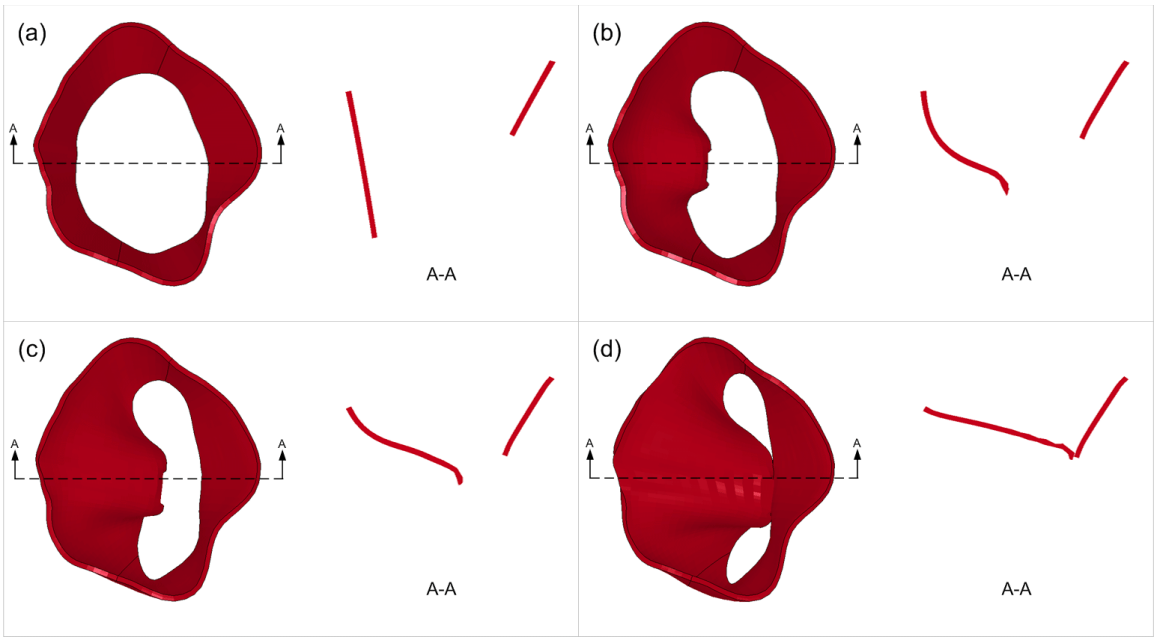

Figure 42 - Displacements applied to the free margin at (a) t=0s, (b) t=0.04s, (c) t=0.06s, and (d) t=0.085s.

The sutures are then added to the model (Figure 43), which are modelled in the same manner as the chordae tendinae (see Section 4.3.6.2.4). The stitch elements attach to nodes on the interior surface of the posterior and anterior leaflets. The type of suture modelled is a Polypropylene 4-0 (PROLENE) suture, which is commonly used in cardiac surgery. The elastic modulus of the suture is 1.3 GPa [52] and the density is 0.8739 g/cm^3 [53] ($8.739 \cdot 10^{-10}$ tonne/mm^3 in LS-DYNA).

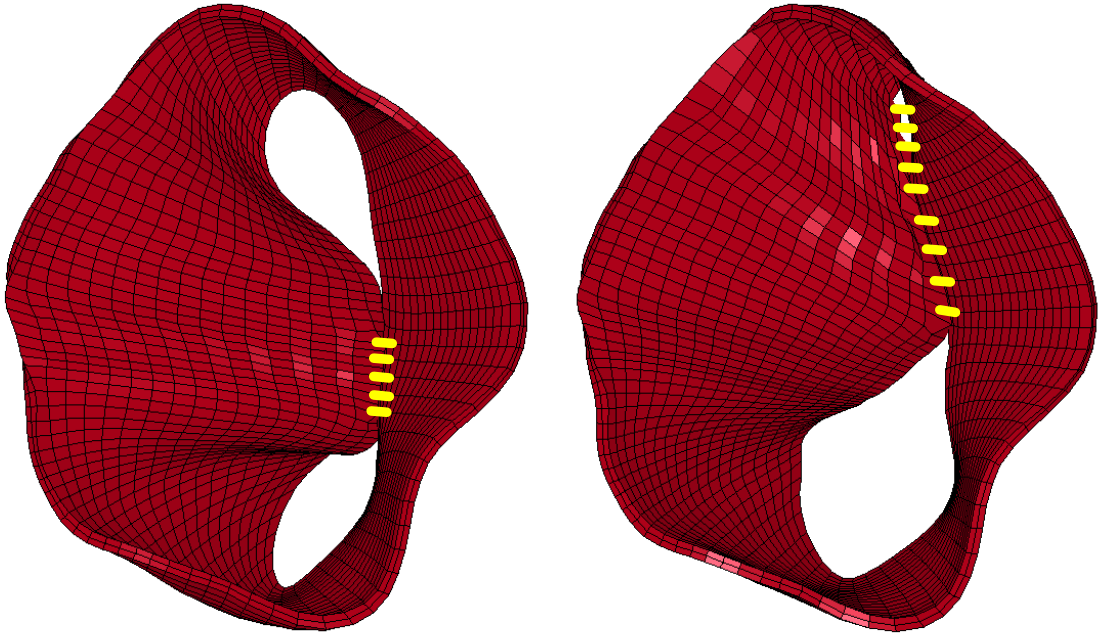

(a) Double-orifice Alfieri stitch (MVp1-DO) **(b) Paracommissural Alfieri stitch (MVp1-PC)**

Figure 43 - Completed Alfieri stitch models (stitches enlarged for illustrational purposes).

It is typical in cardiac surgery to attach an annuloplasty ring to the annulus of the valve being repaired with an Alfieri stitch. Thus, the annuloplasty ring model was combined with the two Alfieri stitch models (Figure 44). Using the same load and boundary conditions as described in the previous chapter, the double-orifice Alfieri stitch model was then analyzed in LS-DYNA to determine the dynamic properties of the valve and the impact of this repair technique.

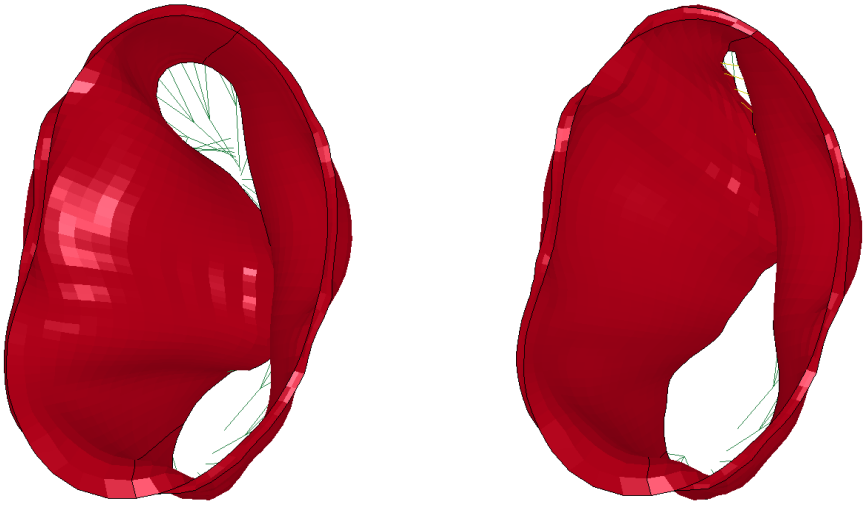

(a) Double-orifice Alfieri stitch with annuloplasty ring (MVp1-DO-A)

(b) Paracommissural Alfieri stitch with annuloplasty ring (MVp1-PC-A)

Figure 44 – Alfieri stitch models with annuloplasty ring applied to the annulus.

5.3 Quadrangular Resection

The quadrangular resection procedure involves removing a section of the posterior leaflet, from the annulus to the free margin. The resulting gap in the leaflet is closed by drawing the sides of the gap closer and suturing the leaflet together, as illustrated in Figure 45.

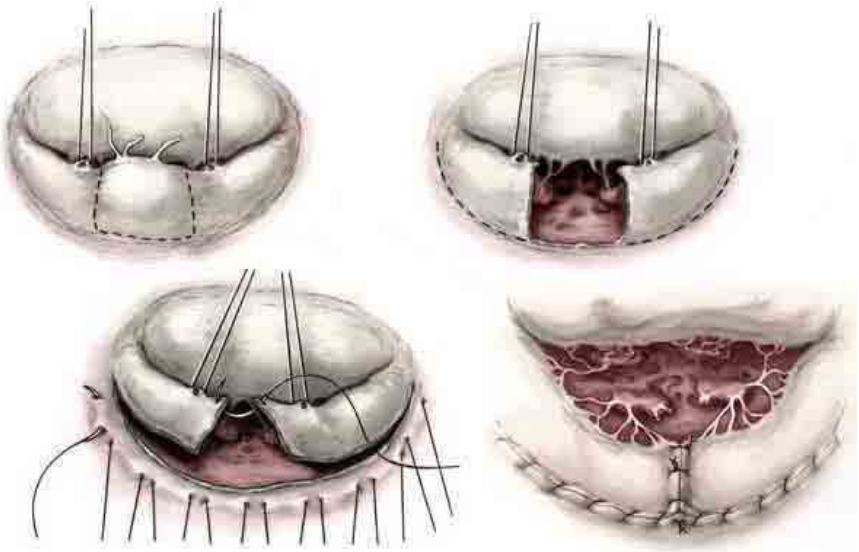

Figure 45 - Quadrangular resection of the posterior leaflet [54].

The approach used for modeling this repair technique is similar to that used for the previous repair techniques. First, a section at the centre of the posterior leaflet is identified for removal (Figure 46-a). The nodes and elements forming this section of the leaflet are deleted from the LS-DYNA input file for model MVp1 (Figure 46-b). The nodes on the cut surfaces of the leaflet are selected to have displacements applied to them. These displacements draw the two surfaces together, where they meet in the centre of the removed section. Each node on one surface, defined as point P_1, is paired with a node on the other surface (P_2), forming a vector from their coordinates:

$$\vec{R}_i = P_2 - P_1 \tag{0.68}$$

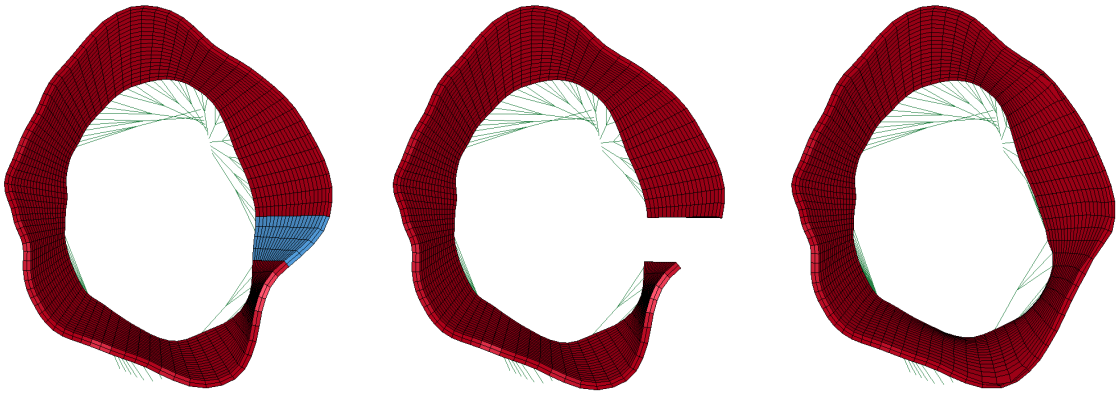

(a) **(b)** **(c)**

Figure 46 – (a) Section of leaflet to be removed (in blue), (b) section removed, and (c) section closed.

The displacements required to draw the two surfaces together are equal to

$$d_i = \frac{\left|\vec{R}_i\right|}{2} - 0.1 \tag{0.69}$$

where i is the number of nodes in the set. A constant of 0.1 mm is subtracted from each displacement to create a small gap between the surfaces, avoiding contact during the analysis. Also, one chordae tendinae was removed from the model, since its attachment points were on the removed section of leaflet.

As before, the *BOUNDARY_PRESCRIBED_MOTION_NODE keyword is used to apply the displacements to the nodes. The vector $\vec{R}_i$ defined above is used as the direction vector for each node i. The model is analysed in LS-DYNA and the nodal coordinates for the model, with leaflets drawn together as pictured in Figure 46, are exported. A new model is created based on these coordinates, with sutures added to the inner and outer surfaces of the leaflet. The sutures join to nodes on one side of the cut section of leaflet and cross over the cut to attach to nodes on the other side. The number of nodes and their attachment points can be varied, with nine sutures on each side of the leaflet used for this study. The completed quadrangular resection model is shown in Figure 47. The load and boundary conditions used for the model are the same as for the previous simulations.

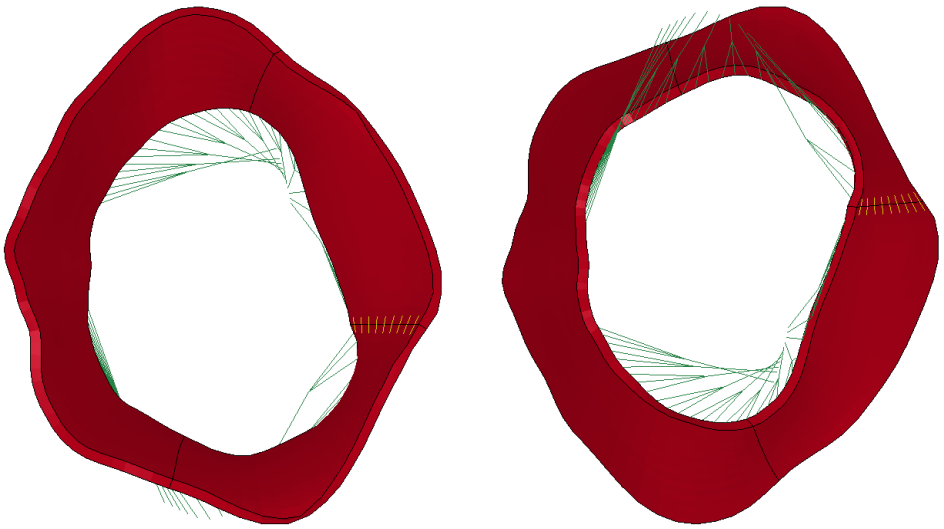

Figure 47 - Quadrangular resection model, with sutures shown on the top (left) and bottom (right) sides of the leaflet.

As for the Alfieri stitch models, the annuloplasty ring model is also applied to the quadrangular resection model, as shown in Figure 48. These two models were analysed

in LS-DYNA to determine the dynamic behaviour of the repair technique over one cardiac cycle.

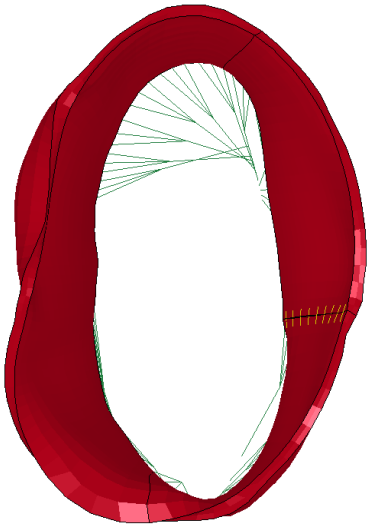

Figure 48 - Quadrangular resection model with annuloplasty ring.

Chapter 6

Results

6 Results

In Chapters 3 to 5, the methods for constructing finite element models of the mitral valve and mitral valve repairs were described, including implementation of the material models, geometric reconstruction, and the load and boundary conditions. This chapter will present the results of the simulations performed on each model. The results obtained from these analyses include:

- Mitral Valve Dynamics
- Principal Stresses in the Leaflets
- Chordae Tendinae Axial Forces
- Degree of Leaflet Bulging

6.1 Mitral Valve Dynamics

In this section, the dynamics of the mitral valve are presented using images of the mitral valve showing the opening and closing of the valve over time. Figure 49 shows the pressure load applied to the valve in each image, indicated by the red dots.

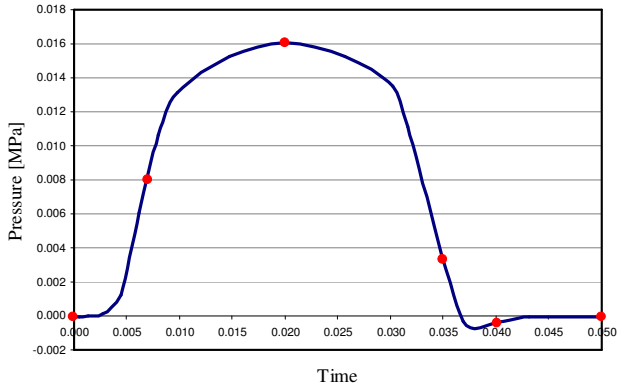

Figure 49 - Load curve indicating the loads at each time step for which analysis images are presented.

6.1.1 MVs1 – Normal Mitral Valve

The dynamics of the normal mitral valve model (MVs1) are shown in Figure 50, which shows that the valve closes as the pressure is ramped up from 0 kPa to approximately 130 kPa at the start of systole, from t = 0.04 s to t = 0.01 s. It remains closed as the pressure increases to its peak of 160 kPa at t = 0.02. During closure, there are pronounced folds, wherein the leaflet is bent over on itself with the centre of the fold running radially from the free margin to the annulus, in the posterior leaflet near the commissures and at both commissures. The valve begins to open at t = 0.03 s, when the pressure starts to rapidly decrease from 130 kPa to below zero at the end of systole. The leaflets continue to open through the start of diastole until it is fully open at t = 0.045 s.

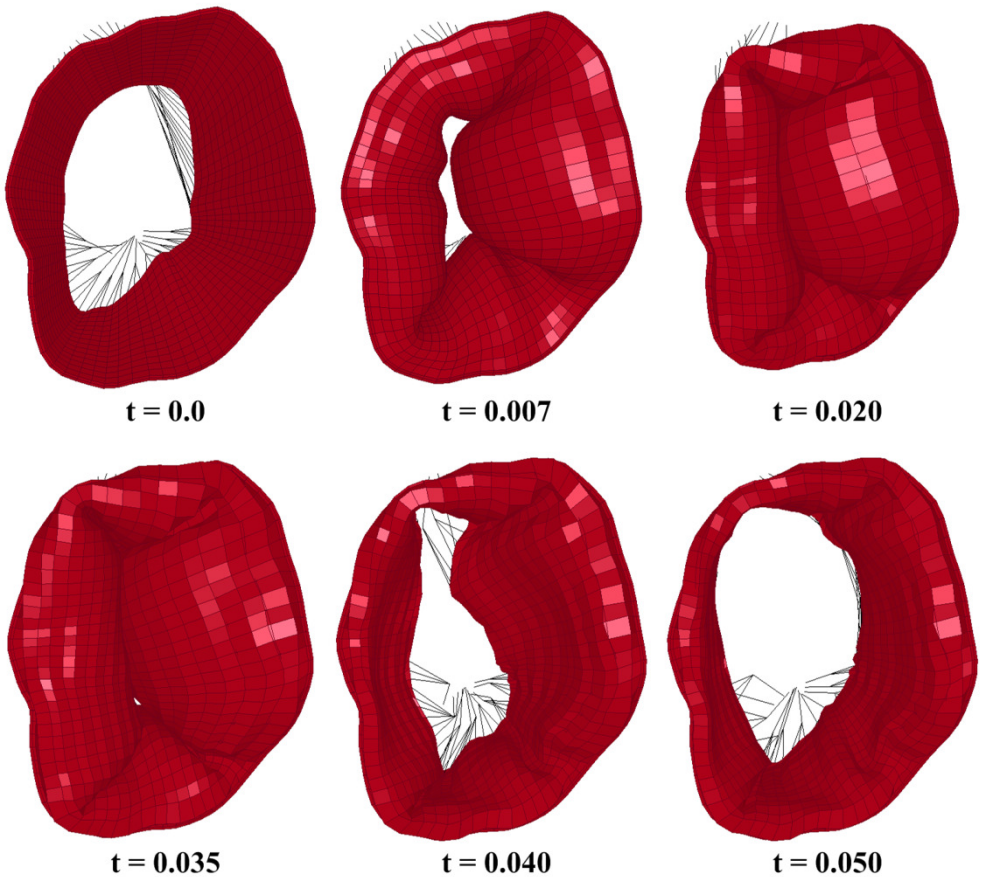

Figure 50 - View from the left atrium showing the closing and opening of the normal mitral valve model, MVs1.

6.1.2 MVp1 – Dysfunctional Mitral Valve

In Figure 51, coaptation of the MVp1 valve model appeared to be complete at t = 0.01 s. The leaflets are folded at the commissures, with minimal folding on one side of the posterior leaflet and a very large fold in the other side. As with MVs1, the valve begins to reopen as the pressure drops after t=0.03 and is fully open once systole has ended.

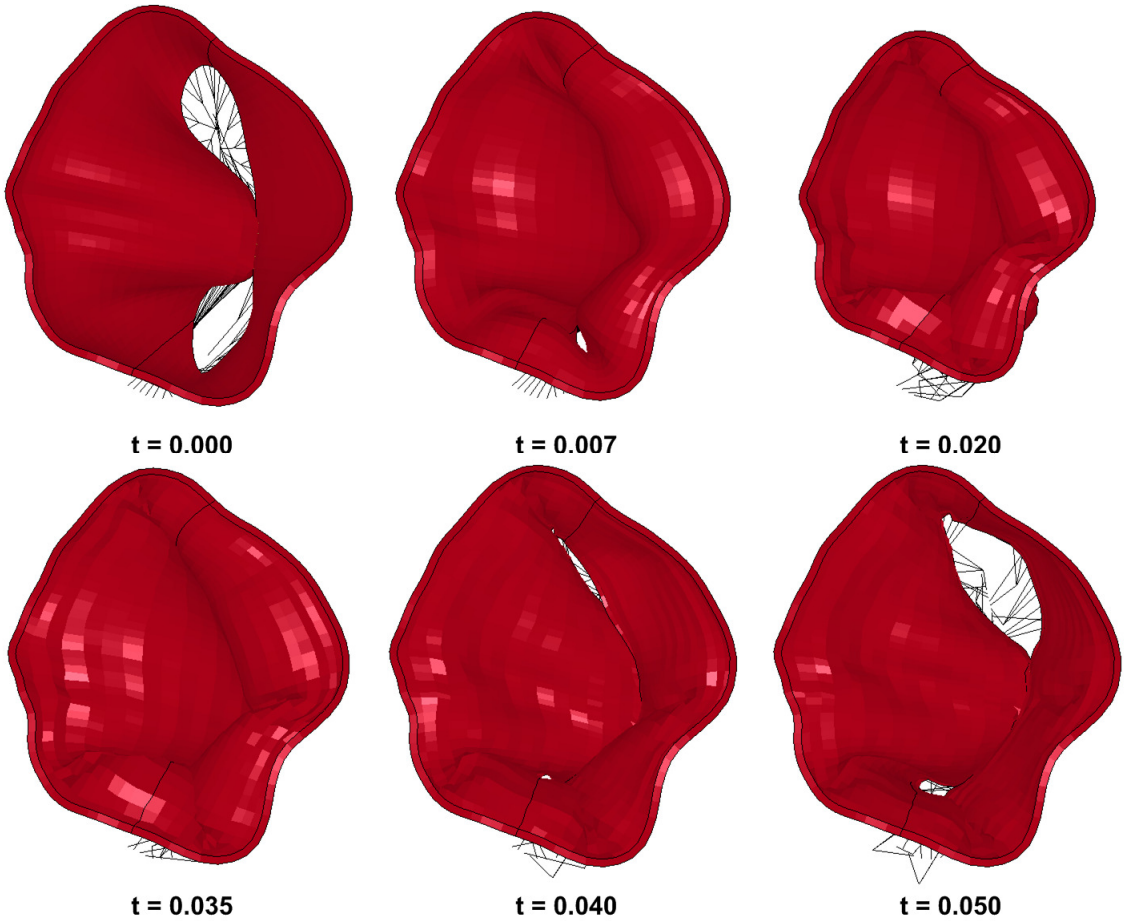

Figure 51 - View from the left atrium of the dynamics of the dysfunctional mitral valve, model MVp1.

However, Figure 52 shows a hole visible between the leaflets when viewed from a different angle. The hole was located at a large fold at the centre of the posterior leaflet. At t = 0.016 s, the hole reaches its smallest size and remains minimal until the valve begins to reopen. In examining the ultrasound images used to construct this model, it is

noted that there appears to be a small hole at this location in the images (Figure 53). Although no systematic parameter sensitivity analysis was carried out, the hole was present in the simulation for a wide range of leaflet material properties.

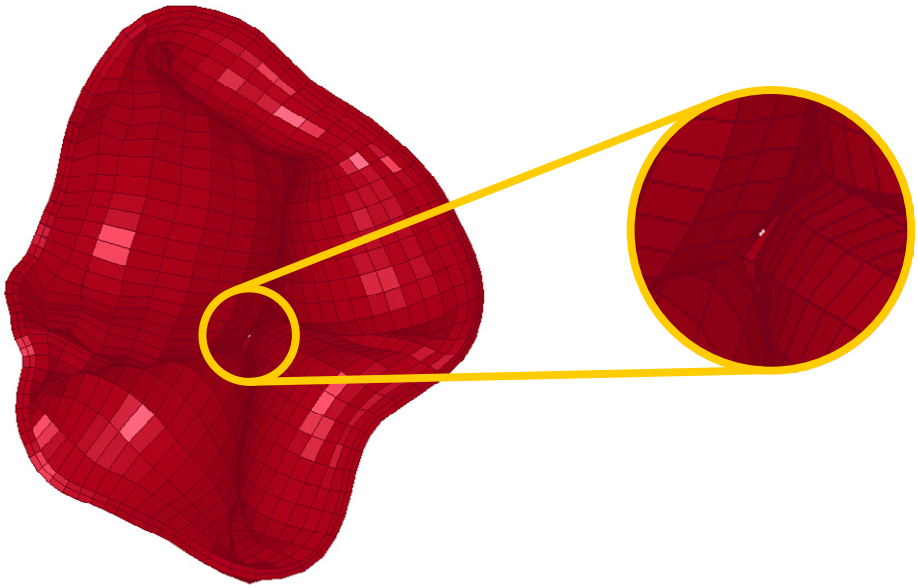

Figure 52 - Incomplete coaptation of the leaflets during systole in model MVp1.

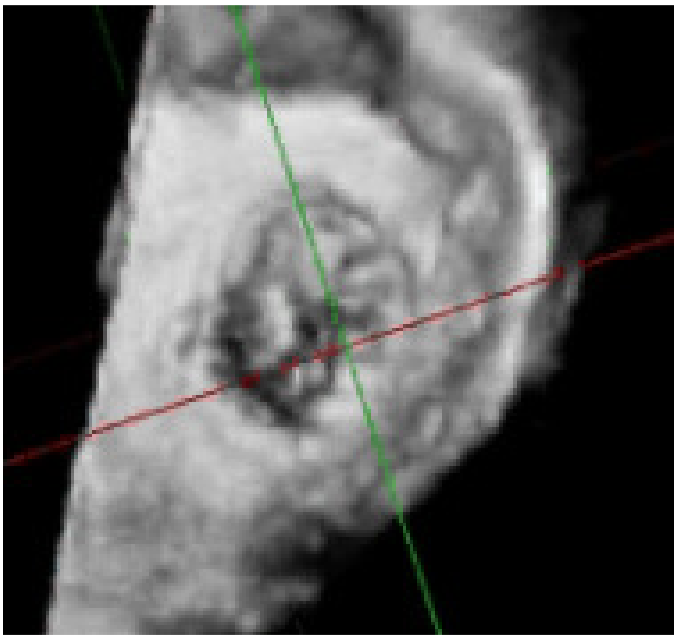

Figure 53 - Ultrasound image from the patient showing a dark spot at the centre of the valve, a possible hole, or incomplete coaptation, in the mitral valve.

6.1.3 MVp1-DO – Double-orifice Alfieri Stitch

Analysis of the double-orifice Alfieri stitch model, without the annuloplasty ring, shows similar behaviour as the MVp1 model (Figure 54). Coaptation occurred by $t = 0.01$, after the initial ramp up of the pressure, with a large fold in the centre of the posterior leaflet where the two leaflets are sutured together. The large fold in the posterior leaflet near the commissure is reduced, compared to MVp1, and there is no fold in the posterior leaflet near the opposite commissure. In diastole, the valve has reopened, forming two orifices for blood flow. As can be seen between Figures 51 and 54, the final orifice sizes are considerably smaller than the unstitched model.

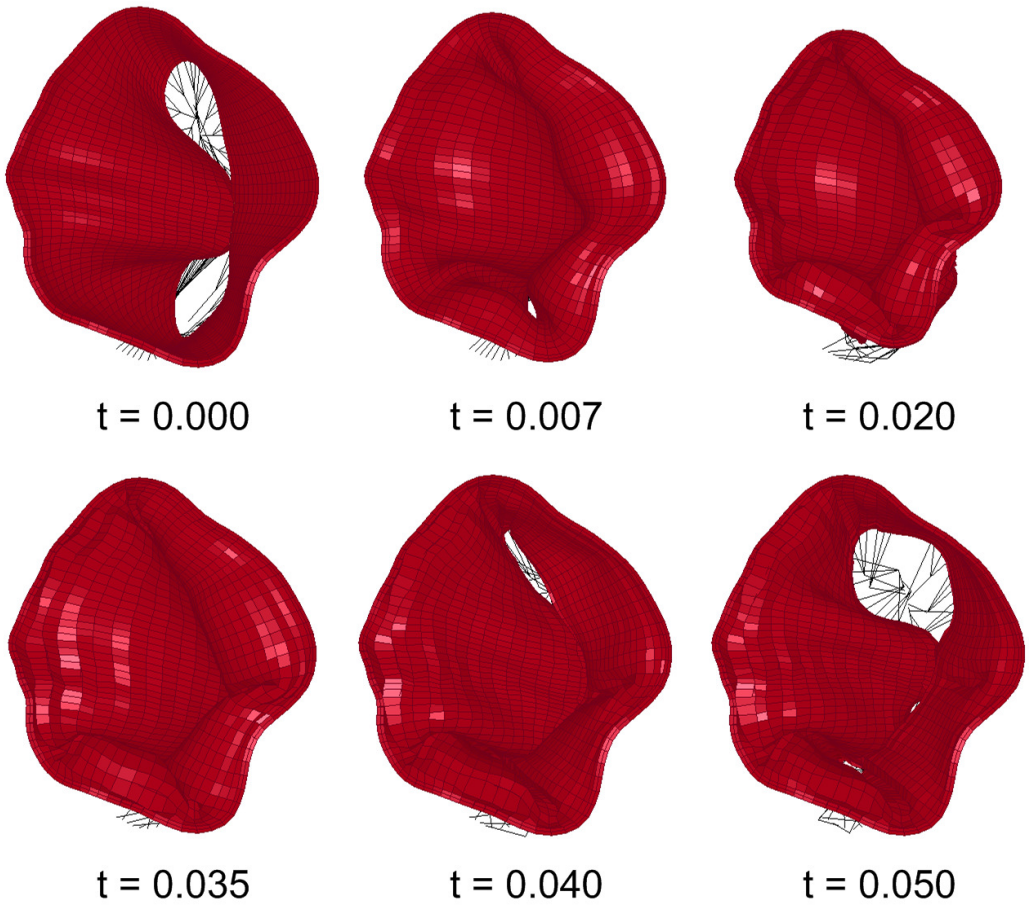

Figure 54 - View from the left atrium showing the dynamics of the double-orifice Alfieri stitch, model MVp1-DO.

6.1.4 MVp1-DO-A – Double-orifice Alfieri Stitch with Annuloplasty

In comparing Figures 54 and 55, it is seen that the addition of the annuloplasty ring coupled with the double-orifice Alfieri stitch has eliminated the fold at the centre of the posterior leaflet. Smalls folds are visible in the posterior leaflet near each commissure, with folds at each commissure as well. Coaptation of the leaflets occurs by $t = 0.01$ s with no holes showing between the leaflets. Valve opening is improved over the same model without the annuloplasty ring, with larger orifice sizes in diastole.

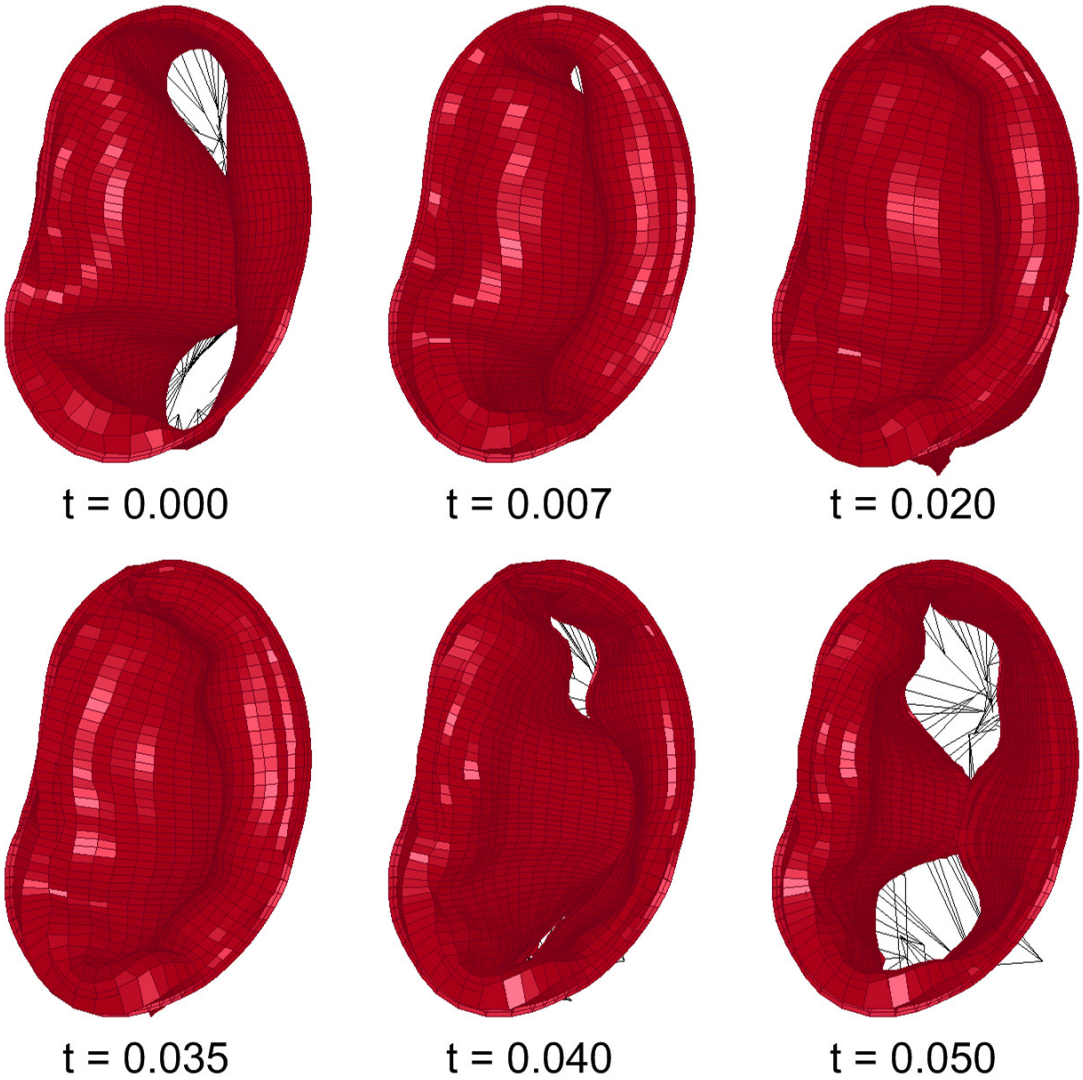

Figure 55 - View from the left atrium of the dynamics of the double-orifice Alfieri stitch with annuloplasty ring, model MVp1-DO-A.

6.1.5 MVp1-PC – Paracommissural Alfieri Stitch

Analysis of the paracommissural Alfieri stitch in Figure 56 showed similar coaptation as previous models, with complete coaptation by t = 0.01 s. In the sutured portion of the valve, there is a fold at the commissure, but not in the posterior leaflet near the commissure. The opposite side shows two folds, one at the commissure and one nearby in the posterior leaflet, as was the case in the MVp1 model. At the centre of the posterior leaflet there is a slight fold near the annulus, but it does not extend to the anterior/posterior leaflet contact region. The valve begins to open at the end of systole and is fully open during diastole.

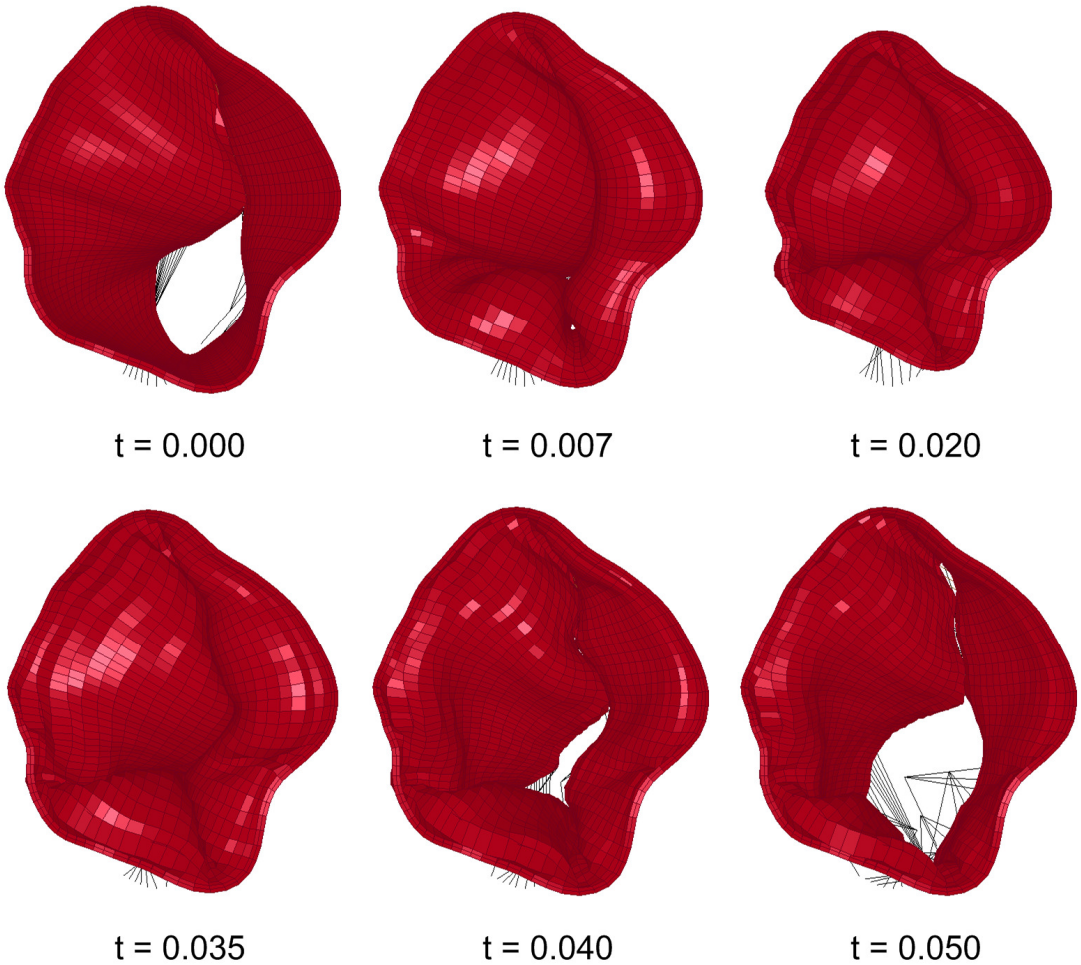

Figure 56 - View from the left atrium showing the dynamics of the mitral valve with a paracommissural Alfieri stitch, model MVp1-PC.

6.1.6 MVp1-PC-A – Paracommissural Alfieri Stitch with Annuloplasty

In this case, coaptation occurs as with the MVp1-PC model, with complete coaptation at *t* = 0.01 s. In Figure 57, at mid-systole there are two folds by the commissure of the sutured portion of the valve, with a small fold in the posterior leaflet and one at the commissure. The fold found in the previous model, without the annuloplasty ring (Figure 56), in the centre of the posterior leaflet near the annulus, is significantly smaller than without the annuloplasty ring.

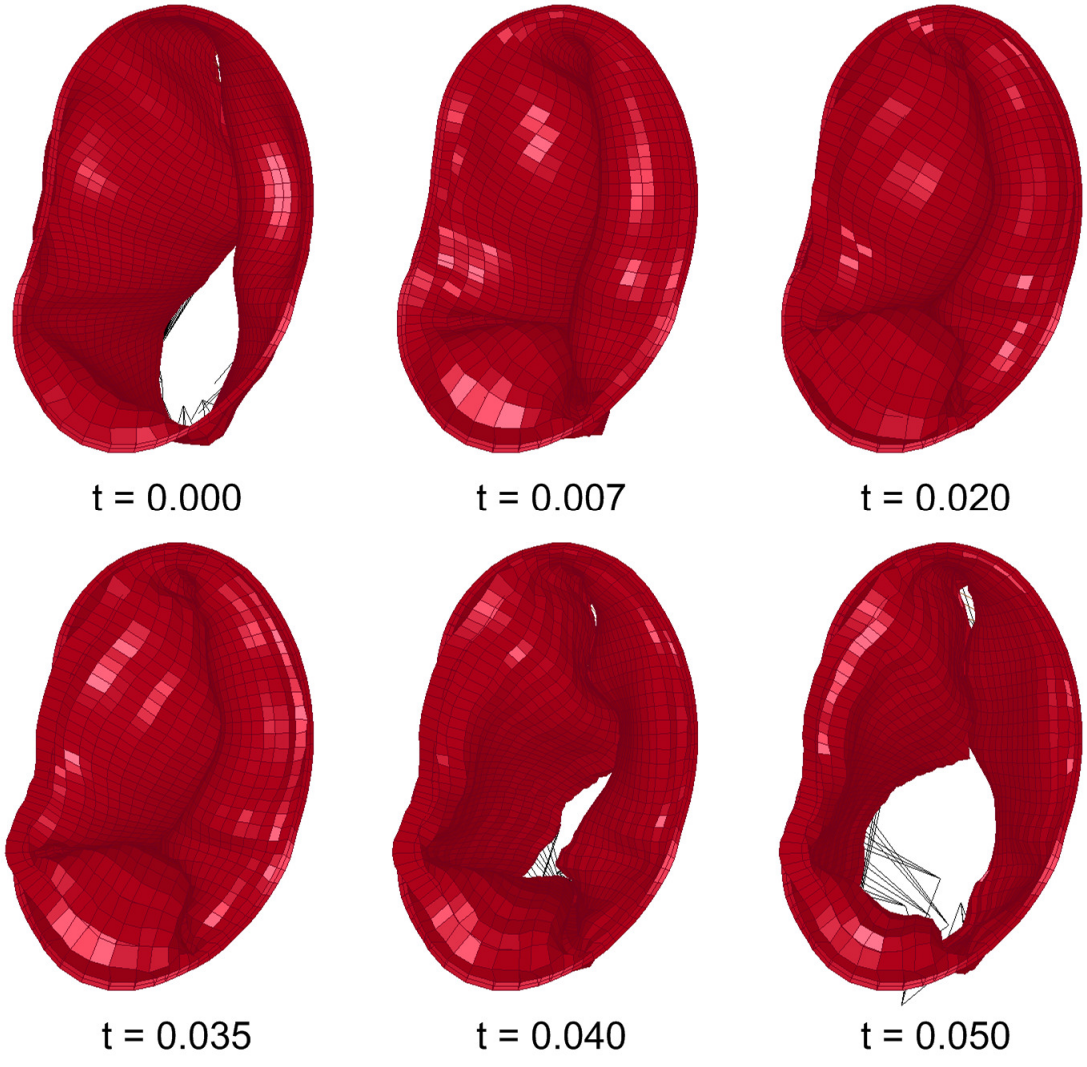

Figure 57 - View from the left atrium showing the dynamics of the paracommissural Alfieri stitch model with an annuloplasty ring, model MVp1-PC-A.

6.1.7 MVp1 – Quadrangular Resection

Figure 58 shows the coaptation and opening of the quadrangular resection model. The model exhibits similar behaviour to the initial patient model, with coaptation done by 0.01 s, opening beginning at 0.03 s and leaflet separation at 0.035 s. The sutured portion formed a fold during systole, similar to the fold that occurred in the initial patient model at the same location.

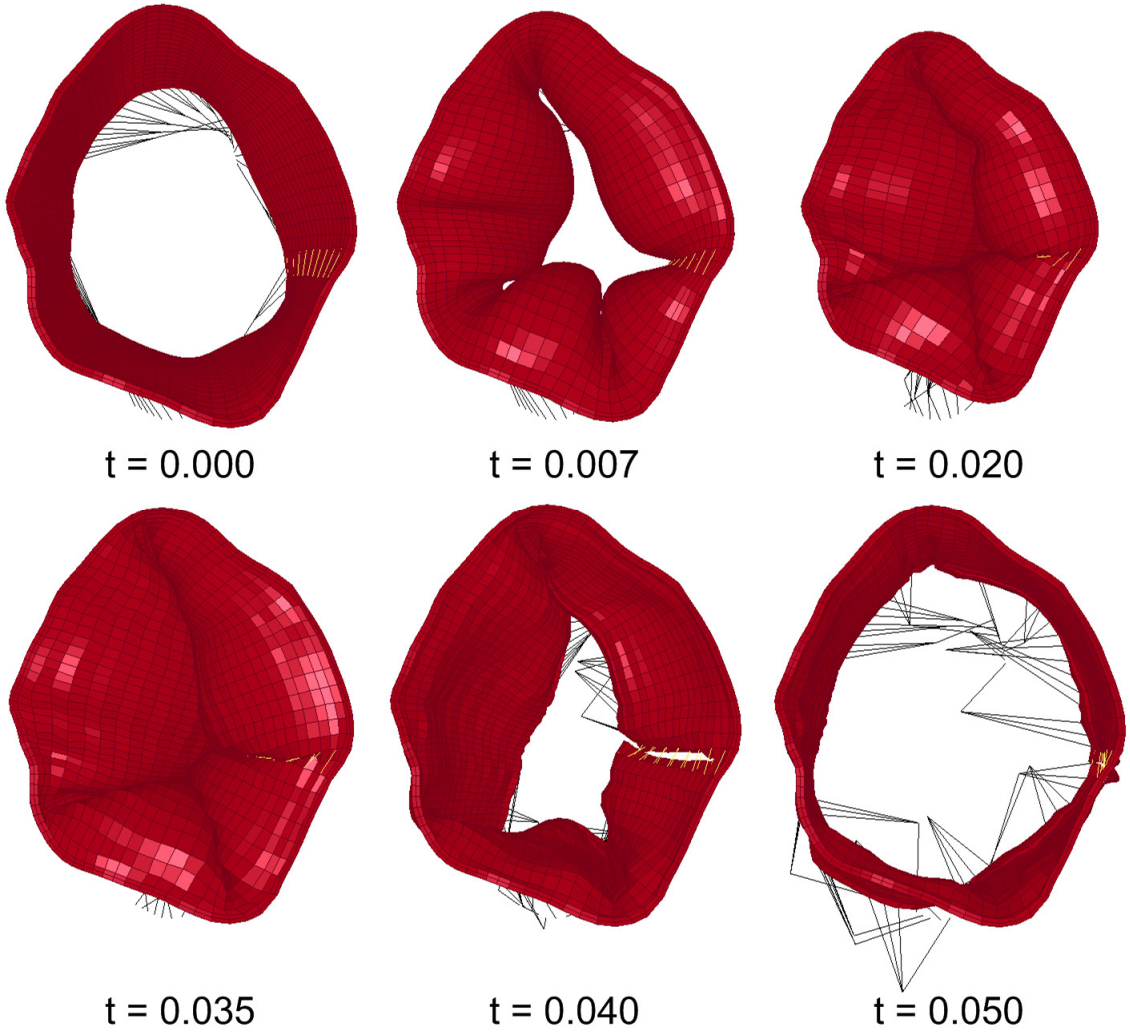

Figure 58 - View from the left atrium showing the dynamics of the quadrangular resection model, model MVp1-QR.

6.1.8 MVp1 – Quadrangular Resection with Annuloplasty Ring

The addition of the annuloplasty ring (Figure 59) caused no change in the timing of coaptation or opening from the previous model (Figure 58). However, the sutured portion of the posterior leaflet pressed flat against the anterior leaflet, unlike all previous models where a fold was formed at this location.

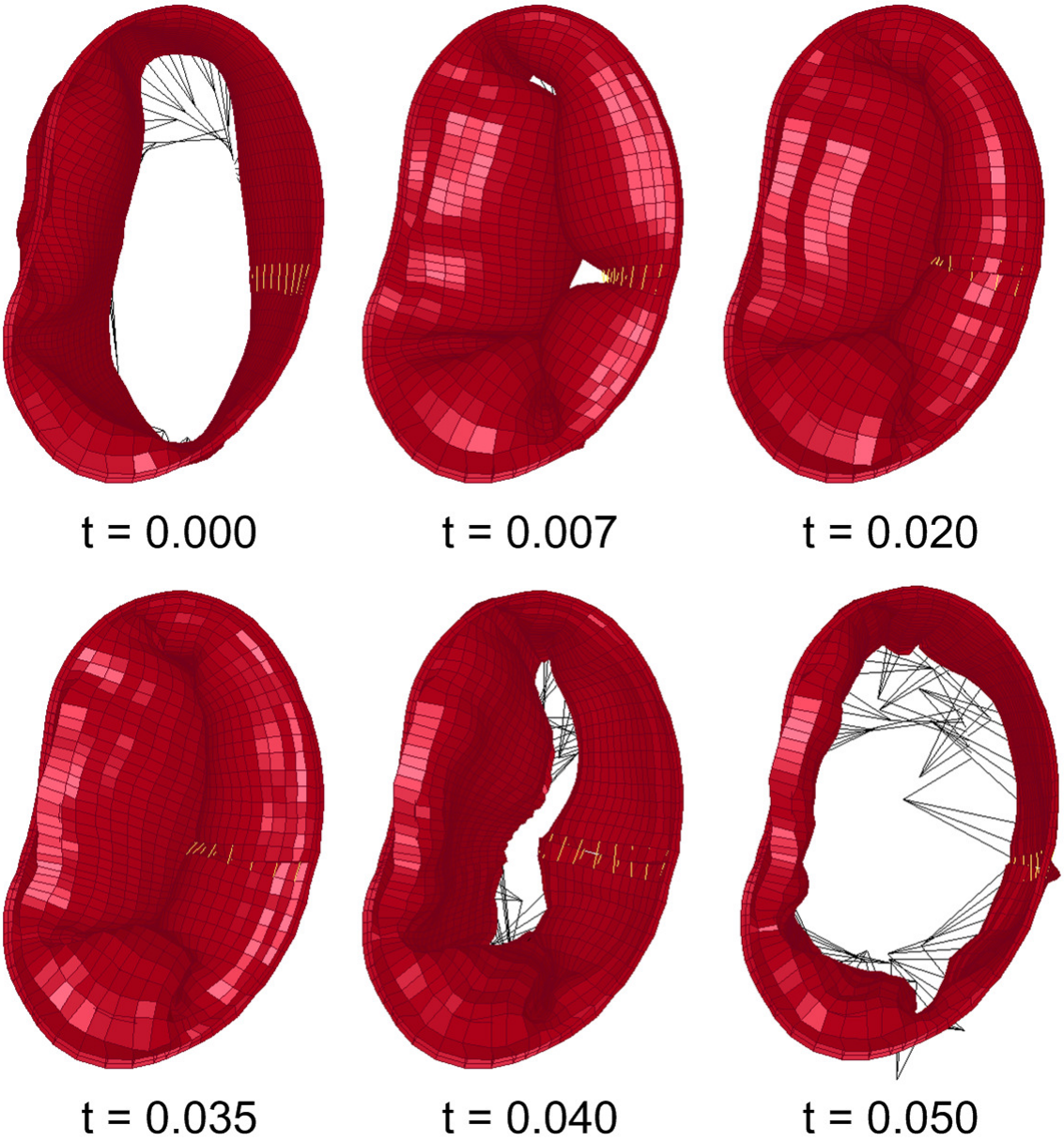

Figure 59 - View from the left atrium showing the dynamics of the quadrangular resection model with an annuloplasty ring, model MVp1-QR-A.

6.1.9 Timing of Coaptation and Opening

All eight previous models exhibited similar coaptation timing, with coaptation commencing at approximately 0.04 s and completed by 0.01 s. Valve opening commenced in all cases at 0.03 s, but with varying times of leaflet separation. In the initial subject and patient models, leaflet separation occurred at 0.035 s, with the valve fully open between 0.043 s and 0.045 s and small billowing in the leaflets for the remainder of the simulation. The Alfieri stitch models showed delayed leaflet separation, with separation occurring at 0.037 s. The valves were fully open by the end of the simulation, but were in the process of opening from leaflet separation until then. The quadrangular resection models showed the same behaviour as the initial models, with leaflet separation at 0.035 s and a fully open valve by 0.045 s.

6.2 Principal Stresses in the Leaflets

This section presents the principal Cauchy stresses found in the leaflets of the valve. Through the duration of the cardiac cycle there are two areas of interest with respect to the stresses. The first is the stresses in the leaflets at mid-systole, when the pressure acting on the leaflets is at its highest. The second is the stresses in the mitral valve repair models during diastole, when the valve is open and the leaflets are restrained by the sutures. The stress results are presented in the form of stress contour plots and stress vector plots, as they provide information about the magnitude and direction of stress.

6.2.1 MVs1 – Normal Mitral Valve

The stress contour plots in Figure 60 show the regions of relatively high stress in the leaflets in mid-systole. The 1st principal stress plot shows relatively high stresses in the bulging regions on each leaflet, with the centre of the anterior leaflet experiencing higher stresses than the posterior leaflet. The anterior leaflet shows stresses on the order of 0.4 MPa to 0.6 MPa at its centre, with stress diminishing away from the centre. The 1st principal stresses in the posterior leaflet are lower, ranging from approximately 0.2 MPa to 0.4 MPa.

The same pattern is seen in the 2nd principal stresses, with a high stress region at the centre of the anterior leaflet, with a large region at approximately 0.245-0.28 MPa. In the posterior leaflet, the 2nd principal stress is minimal, near zero throughout most of the leaflet. Along the annulus, the 1st principal stresses show several areas of high stress while the 2nd principal stresses are near zero. Also, the stresses along the folds in the leaflets are shown to be very low, in contrast to the centre regions of the leaflets.

In comparing the two views in Figure 60, the principal stresses viewed from the ventricle side of the leaflets show the same stresses as the atrial side of the leaflets. Also, the stresses in the ventricle side appear to mirror those of the atrial side of the leaflets. An area of stress concentration is visible at the free margin, where the chordae tendinae attach to the leaflet, in the view from the ventricle side. Areas of relatively high 1st principal stress are also apparent at some locations along the annulus

The vector plot in Figure 61 shows the 1st principal stresses are in the radial direction, in general, but with 1st and 2nd principal stresses in the anterior leaflet being near equal in magnitude towards the centre of the valve.

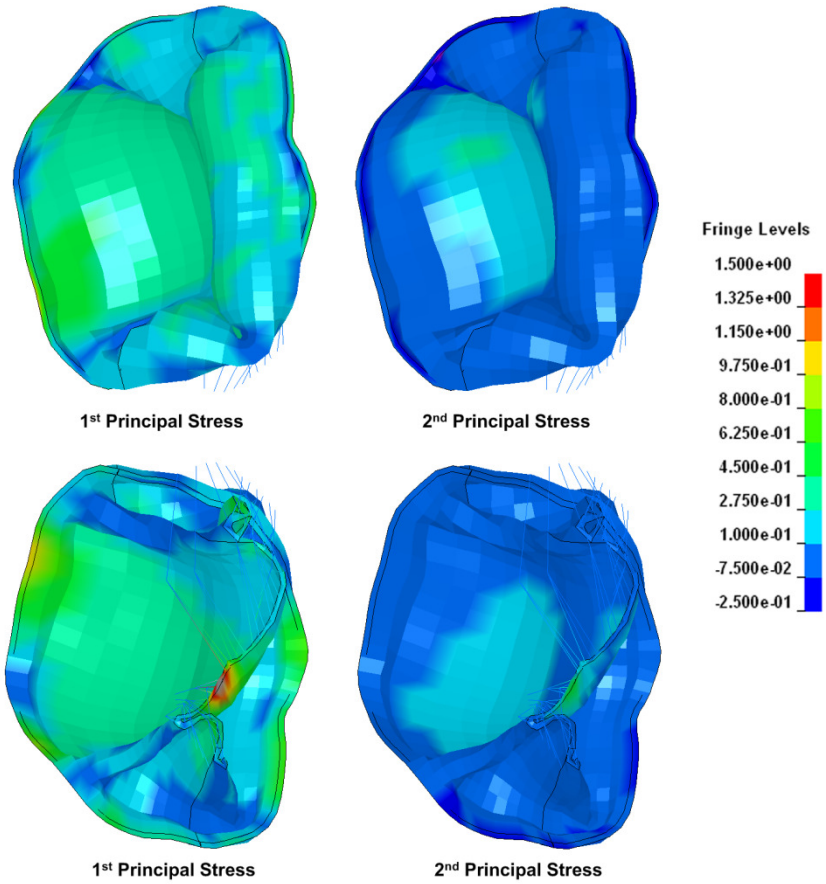

Figure 60 - Two views of the contours of the 1st principal stress [MPa] and the 2nd principal stress [MPa] of the normal mitral valve (MVs1) at mid-systole: atrial side (top) and ventricle side (bottom).

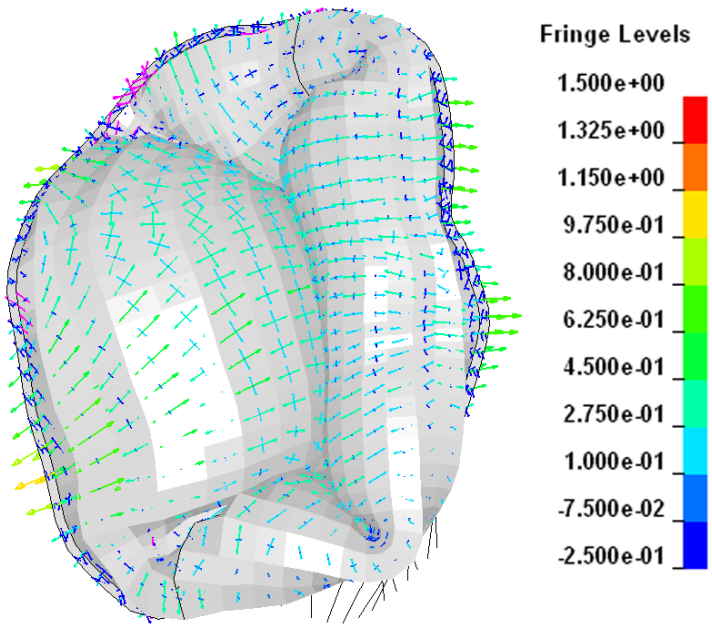

Figure 61 - Vector plot of the principal stresses [MPa] in the normal mitral valve (MVs1) at mid-systole.

6.2.2 MVp1 – Dysfunctional Mitral Valve

The stress contours for the dysfunctional mitral valve show very similar results to the normal mitral valve. Figure 62 shows relatively high 1st principal stresses in the anterior leaflet, ranging from approx. 0.3-0.6 MPa, with stress concentrations at the annulus near the commissures. Also, the figure shows very low stresses along the folds in the leaflets, as with the normal mitral valve. The 2nd principal stresses are highest at the centre portion of the anterior leaflet, ranging from approx. 0.07-0.22 MPa, and are predominantly compressive throughout the rest of the valve.

The principal stresses viewed from the ventricle side of the leaflets show the same stresses as in the atrial side of the leaflets. Since the stresses on the atrial and the ventricular sides of the leaflets, in both the normal and dysfunctional models, were similar, the stresses in the repair models will only be viewed from the atrium side of the valve.

The vector plot of Figure 63 shows a very similar pattern of principal stress directions to that seen in Figure 61 with the normal mitral valve. The 1st principal stresses are in the radial direction in both leaflets, while the 2nd principal stresses are in the circumferential direction.

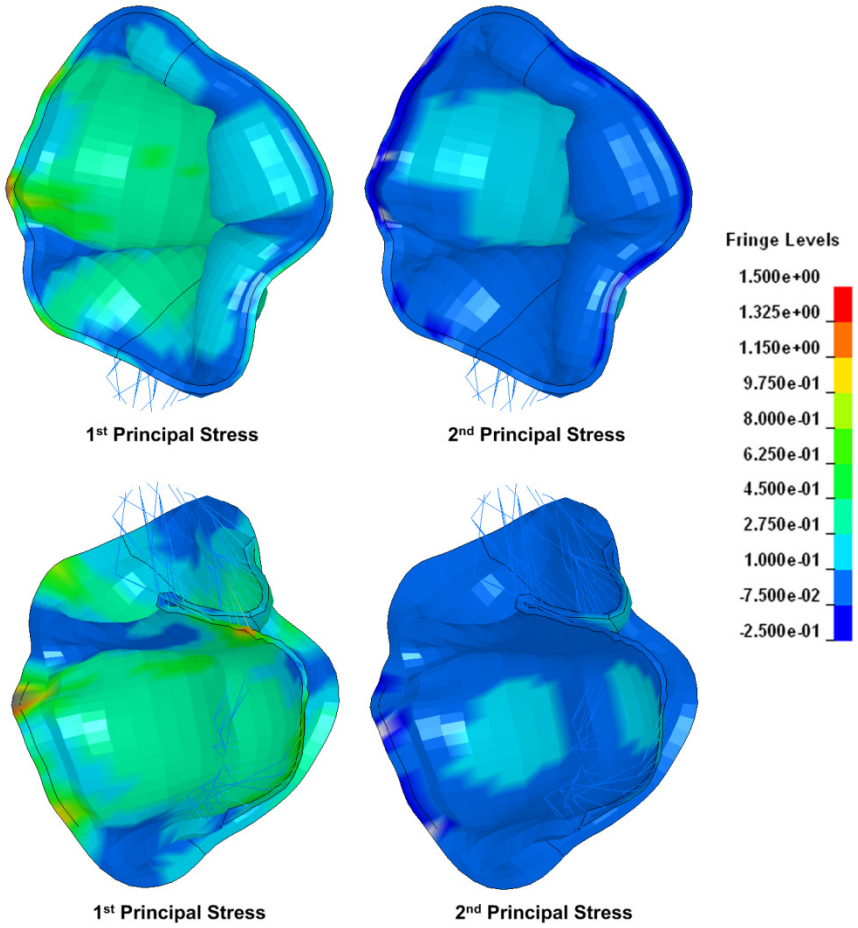

Figure 62 – Two views of the contours of the 1st principal stress [MPa] and the 2nd principal stress [MPa] of the dysfunctional mitral valve (MVp1) at mid-systole: atrium side (top) and ventricle side (bottom).

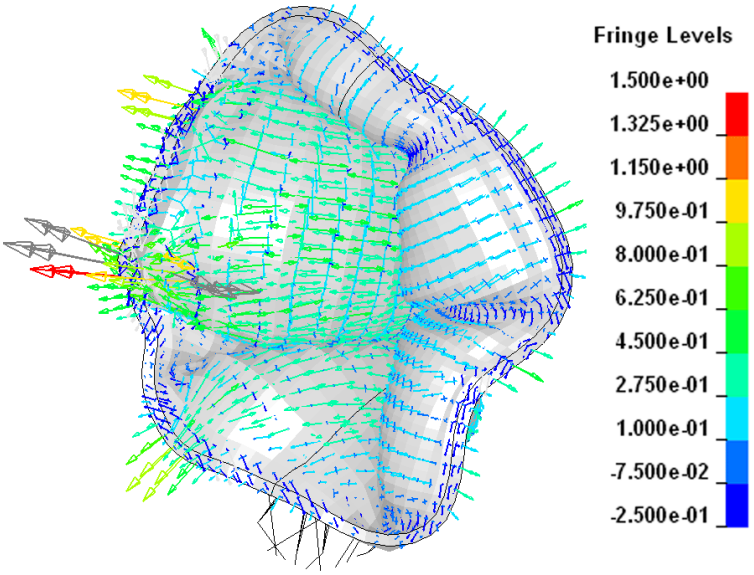

Figure 63 - Vector plot of the principal stresses [MPa] in the dysfunctional mitral valve (MVp1) at mid-systole.

6.2.3 MVp1 – Double-orifice Alfieri Stitch

The stress distribution in both double-orifice Alfieri stitch models (Figures 64 and 65) follow the same pattern as the previous two models discussed (MVs1 and MVp1). However, the 1st principal stresses in both double-orifice models are lower than in unmodified, dysfunctional mitral valve, in the range of 0.18 MPa to 0.52 MPa without the annuloplasty ring and 0.12 MPa to 0.55 MPa with the ring. The 2nd principal stresses are similar in the two double-orifice models, but the region of higher stress in the anterior leaflet is smaller in the annuloplasty ring model, with compressive stresses throughout the rest of the valve.

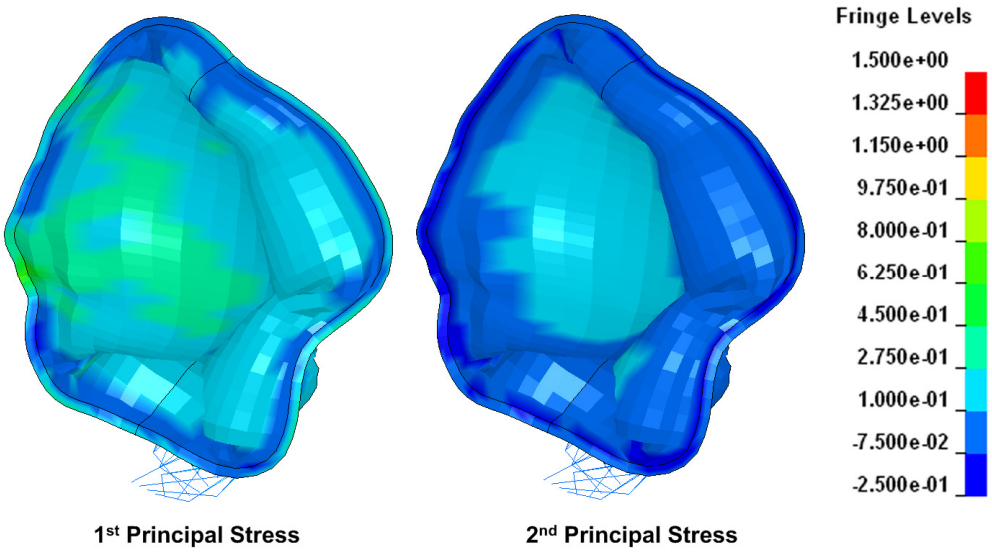

Figure 64 - Contours of the 1st principal stress [MPa] and the 2nd principal stress [MPa] at mid-systole in the mitral valve with a double-orifice Alfieri stitch.

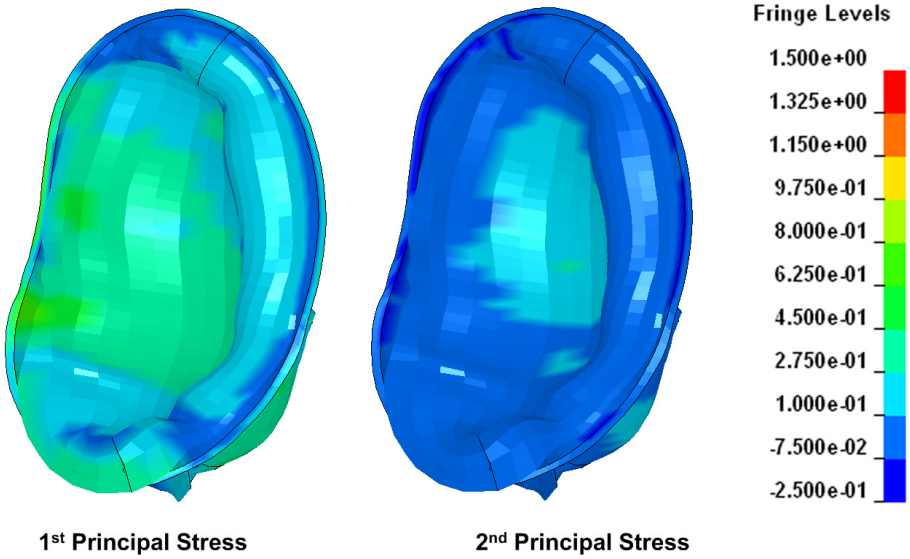

Figure 65 – Contours of the 1st principal stress [MPa] and the 2nd principal stress [MPa] at mid-systole in the mitral valve with a double-orifice Alfieri stitch with an annuloplasty ring.

The vector plots of the principal stresses (Figure 66) show the same stress directions are seen for the normal mitral valve and the unmodified, dysfunctional mitral valve.

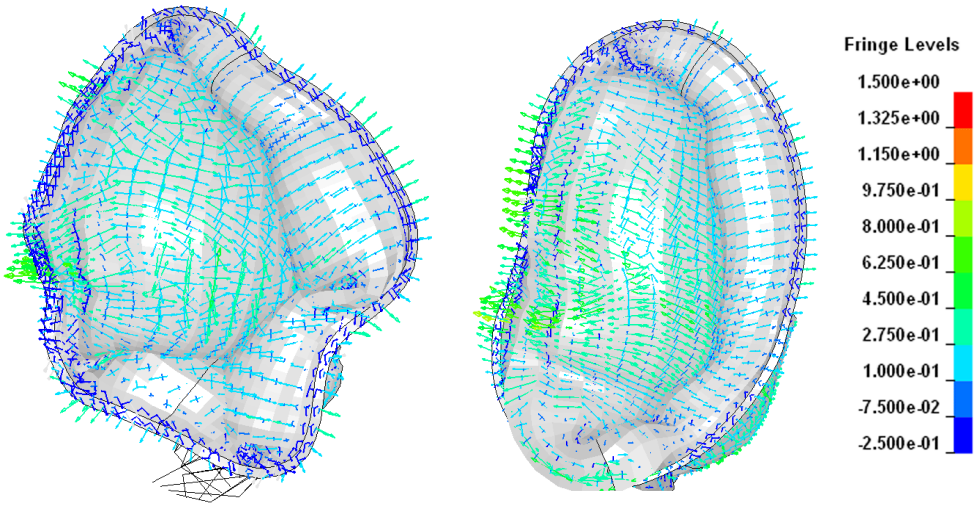

Figure 66 - Vector plots of the principal stresses [MPa] in a mitral valve with a double-orifice Alfieri stitch: without an annuloplasty ring (left) and with an annuloplasty ring (right).

As the sutures joining the leaflets together restrict the opening of the valve, stress contours were also plotted for the diastolic phase of the cardiac cycle. Figures 67 and 68 show relatively low stresses throughout the leaflets, with increased stresses near the sutures in the annuloplasty model.

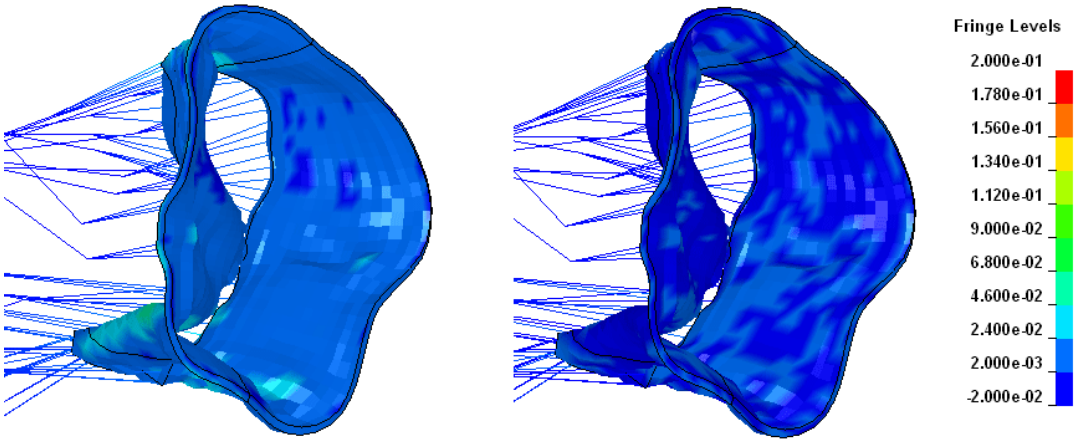

Figure 67 - 1st principal stresses (left) and 2nd principal stresses (right) in the double-orifice Alfieri stitch (MVp1-DO) in the diastolic phase (t = 0.05 s).

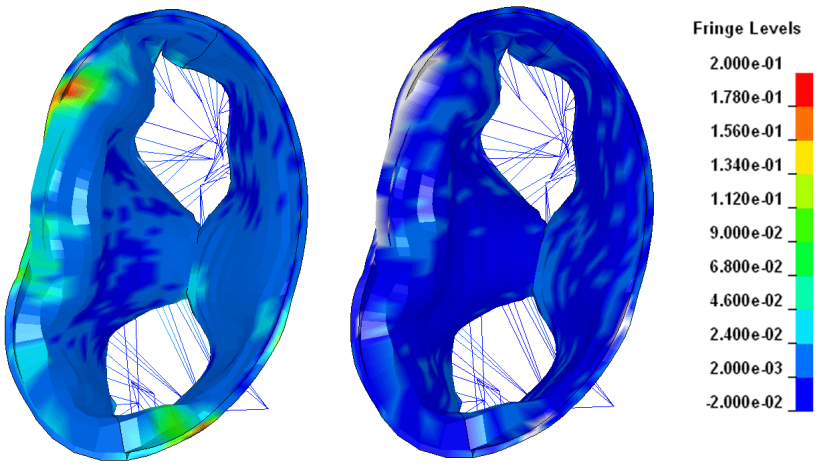

Figure 68 - 1st principal stresses [MPa] (left) and 2nd principal stresses [MPa] (right) in the double-orifice Alfieri stitch with annuloplasty ring in the diastolic phase (t = 0.05 s).

6.2.4 MVp1 – Paracommissural Alfieri Stitch

The principal stresses in the paracommissural Alfieri stitch models, in Figures 69 and 70, show the same pattern as before, with higher stress regions at the leaflet centres. Without the annuloplasty ring, the 1st principal stresses range from 0.15 MPa to 0.43 MPa at the centre of the anterior leaflet, while the 1st principal stresses range from 0.1 MPa to 0.47 MPa with the annuloplasty ring applied. The 2nd principal stresses reach a maximum of 0.22 MPa and approximately 0.17 MPa in the central regions of the leaflets, in the model without the ring and the model with the ring, respectively. The vector plots in Figure 71 show a slight difference from previous models, with the longer vectors on the anterior leaflet angled towards the orifice-side of the valve, away from the sutured portion. The stresses along the annulus are mainly compressive, except for the stress concentrations visible in the figures, indicated by the green colouring.

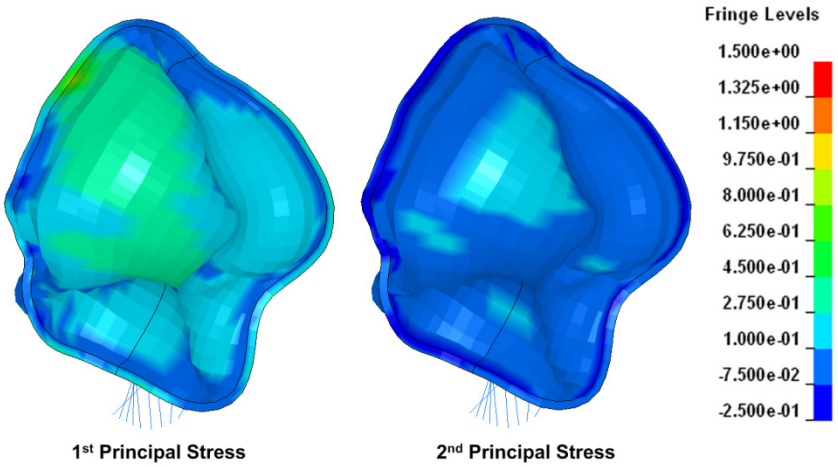

Figure 69 - Contours of the 1st principal stress [MPa] and 2nd principal stress [MPa] at mid-systole in the mitral valve with a paracommissural Alfieri stitch.

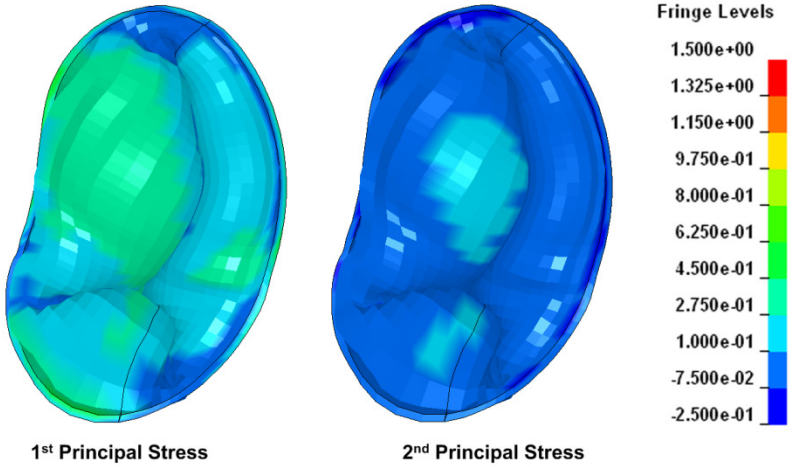

Figure 70 - Contours of the 1st principal stress [MPa] and the 2nd principal stress [MPa] at mid-systole in the mitral valve with a paracommissural Alfieri stitch with an annuloplasty ring.

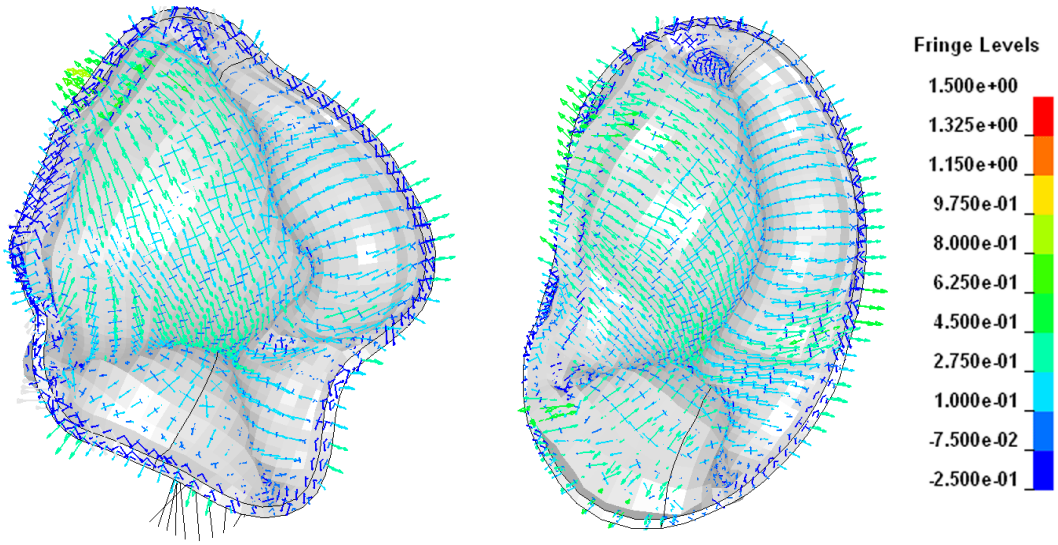

Figure 71 - Vector plots of the principal stresses [MPa] in a mitral valve with a paracommissural Alfieri stitch: without an annuloplasty ring (left) and with an annuloplasty ring (right).

The stress contours of the paracommissural Alfieri stitch model (Figures 72 and 73) in the diastolic phase (t = 0.05 s) show very low stresses, mainly compressive, in the leaflets. There are relatively higher stresses along the sutured area in both models, particularly where the sutures edge meets the orifice. With the addition of the annuloplasty ring to the paracommissural Alfieri stitch, the stresses appeared lower than without it.

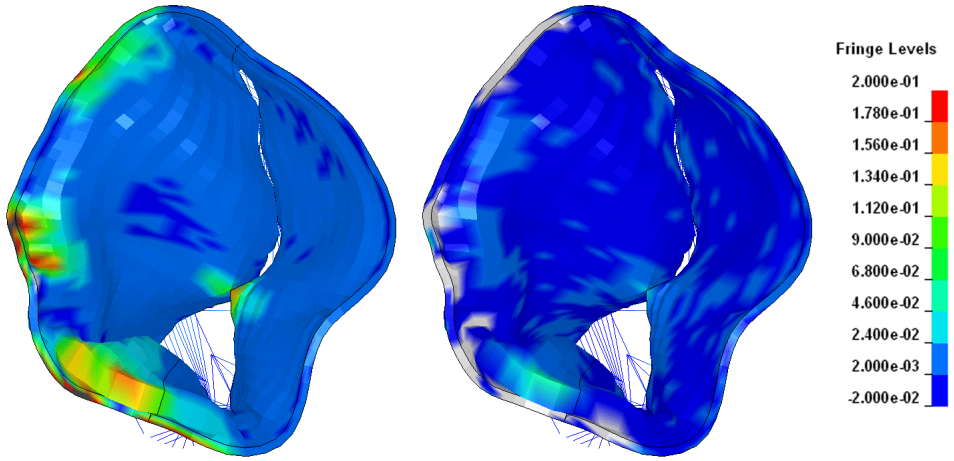

Figure 72 - 1st principal stresses [MPa] (left) and 2nd principal stresses [MPa] (right) in the paracommissural Alfieri stitch in the diastolic phase (t = 0.05 s).

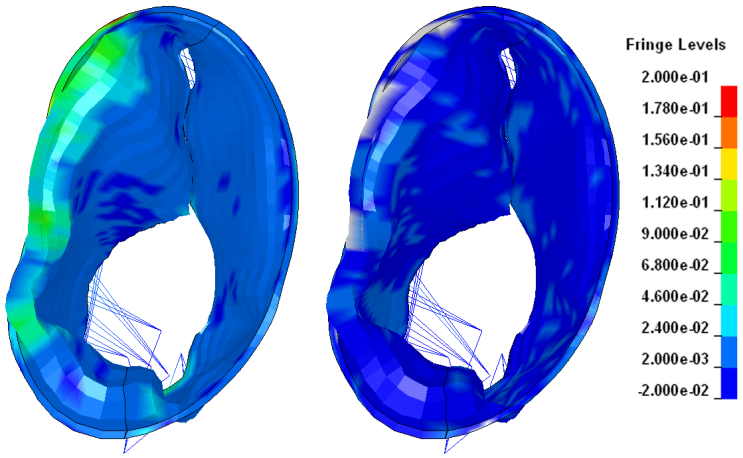

Figure 73 -1st principal stresses [MPa] (left) and 2nd principal stresses [MPa] (right) in the paracommissural Alfieri stitch with annuloplasty ring in the diastolic phase (t = 0.05 s).

6.2.5 MVp1 – Quadrangular Resection

The two quadrangular resection models show stress levels similar to the other models and the same stress distribution pattern (Figures 74 and 75). The application of the annuloplasty ring resulted in lower 2nd principal stresses in the posterior leaflet, with a smaller region of higher stress in the anterior leaflet than was found in the model without the annuloplasty ring The 1st principal stresses remained relatively unchanged. The principal stress vector plots in Figure 76 show the same directions of the 1st principal stresses, radially along the leaflets, as was found in almost all the other models of this study.

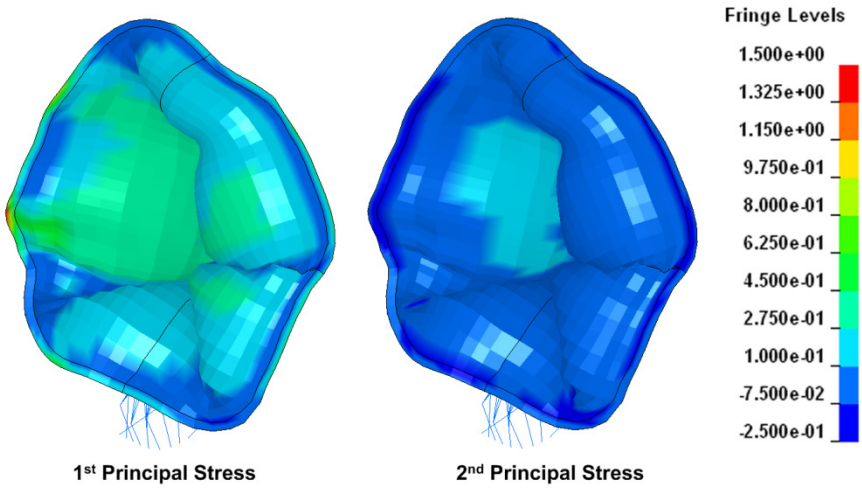

Figure 74 - 1st principal stresses [MPa] and 2nd principal stresses [MPa] in the quadrangular resection model at mid-systole.

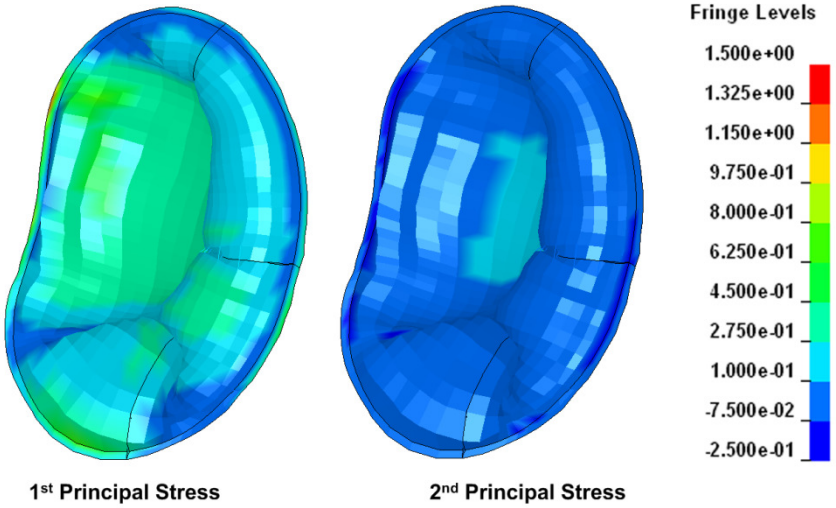

Figure 75 - 1st principal stresses [MPa] and 2nd principal stresses [MPa] in the quadrangular resection model with annuloplasty ring at mid-systole.

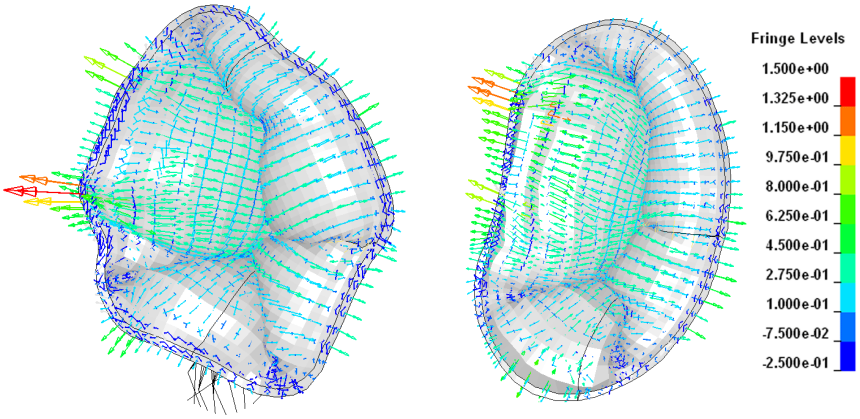

Figure 76 - Principal stress [MPa] vectors in the quadrangular resection models, without annuloplasty ring (left) and with annuloplasty ring (right).

The contour plots of the stress state in diastole are shown in Figure 77 for the quadrangular resection model and in Figure 78 for the model with an annuloplasty ring. In both cases, there is a small increase in stress at the suture area. In the annuloplasty model there is a high stress concentration at the annulus along the anterior leaflet, where the ring curved inwards towards the centre of the valve.

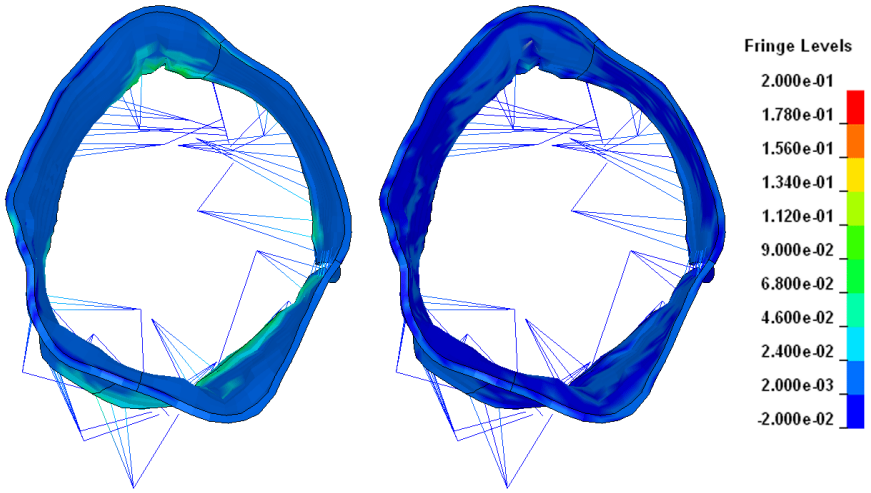

Figure 77 - 1st principal stresses [MPa] (left) and 2nd principal stresses [MPa] (right) in the paracommissural Alfieri stitch in the diastolic phase (t = 0.05 s).

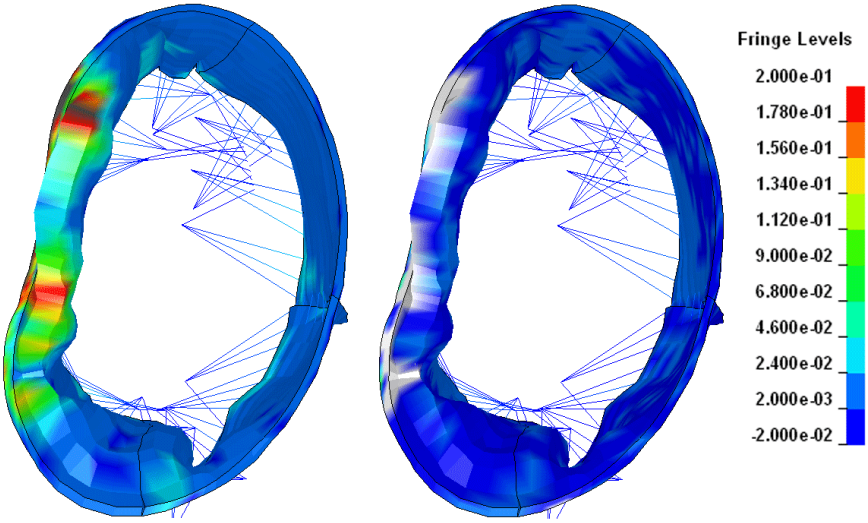

Figure 78 -1st principal stresses [MPa] (left) and 2nd principal stresses [MPa] (right) in the paracommissural Alfieri stitch with annuloplasty ring in the diastolic phase (t = 0.05 s).

6.3 Chordae Tendinae Forces

As the structures preventing prolapse of the leaflets into the left atrium during systole, the chordae tendinae undergo a varying degree of tensile loading. The average force in the chordae tendinae attached to the papillary muscle heads was determined for each analysis, along with its standard deviation. This was done by outputting the axial forces in the beam elements forming the chordae tendinae attached to the papillary muscle heads at each time step. The average force and standard deviation were then calculated in Excel and plotted (Figure 79). In each case, the axial load increased rapidly at the beginning of systole, before dropping to a minimal load, near zero, at the beginning of diastole. As the error bars in Figure 79 indicate, the forces varied considerably during the systolic phase. The average force remained relatively constant, indicating possible uneven distribution of the loading across the tendinae.

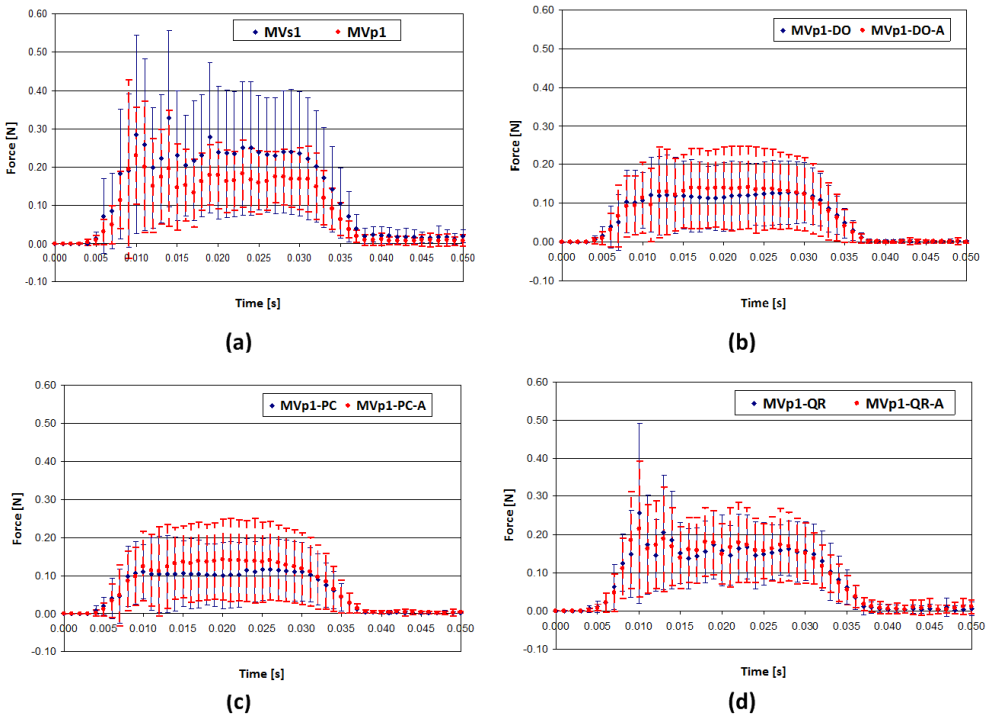

Figure 79 - Mean chordae tendinae forces over the cardiac cycle: (a) Patient-specific models; (b) Double-orifice Alfier stitch models; (c) Paracommissural Alfieri stitch models; and (d) Quadrangular resection models.

6.4 Leaflet Bulging & Coaptation Length

The degree to which the leaflets bulge into the left atrium during systole is another measure of leaflet function and is a useful metric in comparing and analysing repair model performance. Similarly, the radial length of the contact area between the leaflets, or coaptation length, is another useful metric for measuring leaflet function and analysing repair model performance. For each model, a cross-sectional image was taken at the centre of the leaflets at mid-systole (t = 0.02 s). First, the distance between the posterior and anterior annulus was measured (in millimetres) in LS-DYNA. In ImageTool, the four dimensions indicated in Figure 80 were measured in pixels. The ratio between the annulus measurements in LS-DYNA and ImageTool was used to convert the pixel measurements into millimetres. The bulge distances (l_a and l_p) and the coaptation length (l_c) were converted to millimetres using the equation $l = \frac{l_{\text{LS-DYNA}}}{l_{\text{ImageTool}}}$. The results of this analysis are given in Table 4 and the raw data may be found in the Appendix.

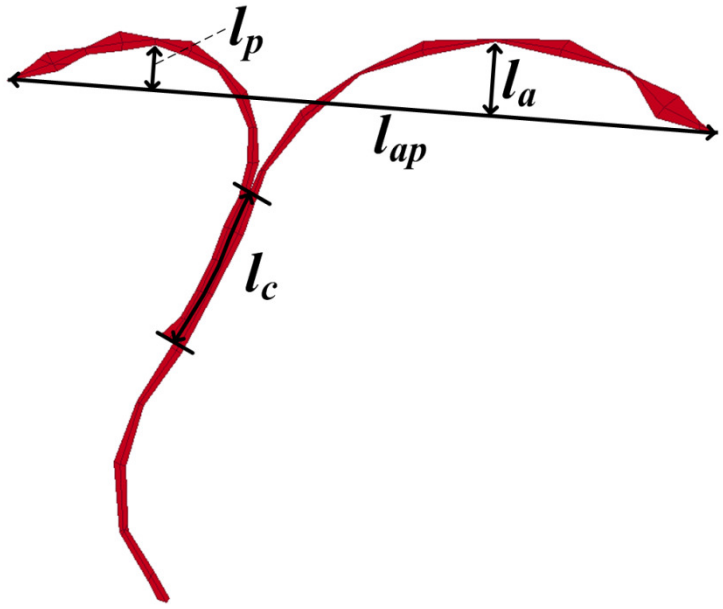

Figure 80 – Measurements used for determining the degree of leaflet bulging and coaptation length.

Table 4 – Degree of bulging of the leaflets into the left atrium and the coaptation length, for each model.

Model	Anterior Leaflet, l_a [mm]	Posterior Leaflet, l_p [mm]	Coaptation Length, l_c [mm]
MVs1	2.6	1.7	6.1
MVp1	1.0	0.7	0.9
MVp1-DO	2.6	1.4	6.1
MVp1-DO-A	3.2	1.0	8.3
MVp1-PC	2.1	2.3	4.6
MVp1-PC-A	2.9	2.0	6.2
MVp1-QR	0.3	1.4	0.9
MVp1-QR-A	1.3	1.0	3.3

6.5 Suture Forces

The average suture forces found in the sutures of the mitral valve repair models are plotted in Figure 81. The loads in the suture elements were extracted from LS-DYNA and the average load was calculated, along with the standard deviation of load for each time step of 0.01 s. The figure shows the effects of coaptation and the pressure loading on the suture loading, with an increase in forces from 0 N at the beginning of the systolic phase to a maximum of 0.033 N when the valve has closed. As expected, the forces

remain elevated throughout the systolic phase, but begin to decrease after mid-systole and drop rapidly as the valve opens. The double-orifice Alfieri stitch caused the highest suture forces, while the forces in the sutures of the quadrangular resection models were negligible. One outlier in the data is the average suture load at $t = 0.038$ s in the double-orifice Alfieri stitch model. The load is considerably higher than all others, at a time point when leaflet separation had just occurred and systole was ending. Other suture loads just before and just after are very low, indicating either a sudden loading due to the separation of the leaflets pulling on the sutures or an unexplained inaccuracy in this data point.

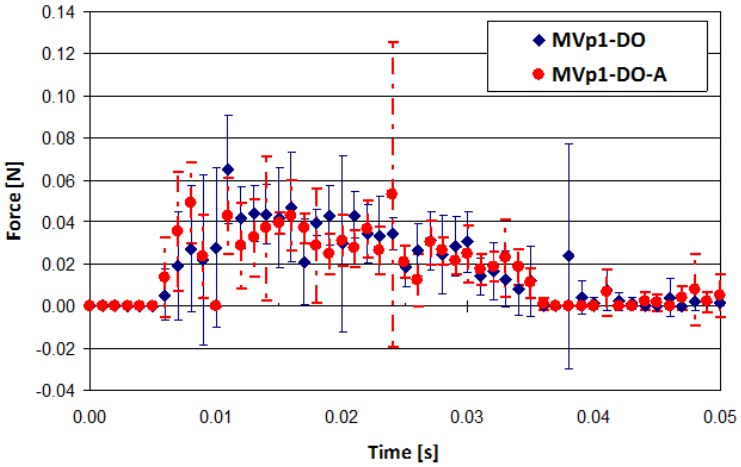

(a)

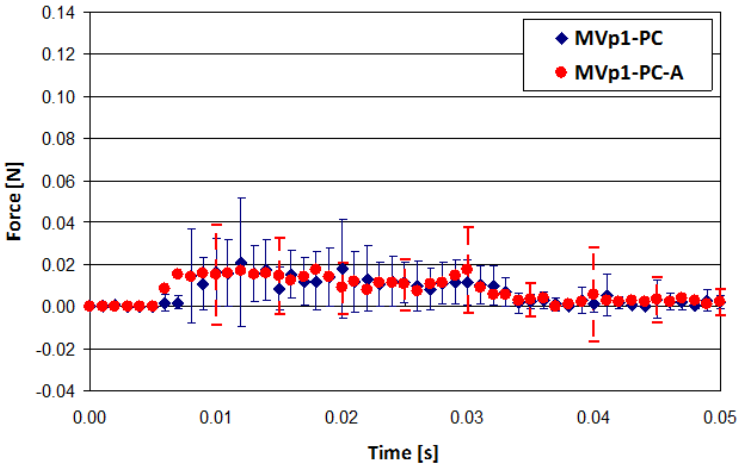

(b)

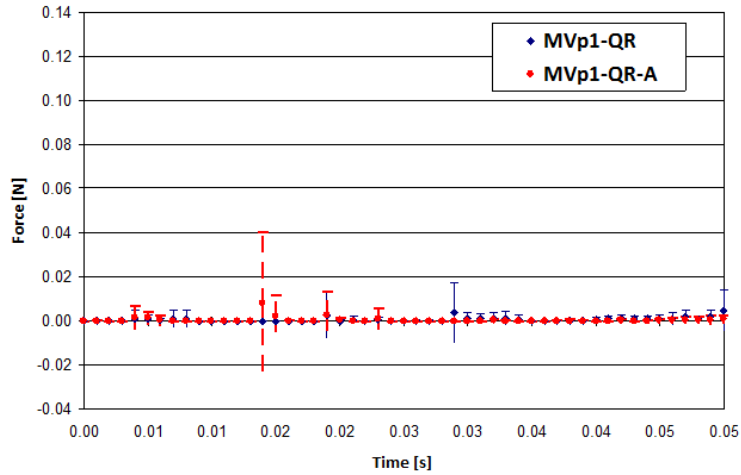

(c)

Figure 81 - Average suture forces found in the mitral valve repair analyses: (a) double-orifice Alfieri stitch models; (b) paracommissural Alfieri stitch models; and (c) quadrangular resection models.

Chapter 7

Discussion and Conclusions

7 Discussion and Conclusions

7.1 Discussion of Results

In chapters three to five of this study, the methods used for constructing three dimensional solid models of the mitral valve and mitral valve repair techniques were presented. In chapter six, the results of a dynamic finite element analysis were given, showing in particular the dynamics of the mitral valve. In this chapter, the results of these analyses are discussed, with attention to both qualitative and quantitative results.

7.1.1 Dynamics

The primary goal of this study was to simulate the dynamics of the mitral valve, which can be difficult to quantify. Qualitatively, the views of the models at peak pressure show folds in the leaflets at the commissures and nearby in the posterior leaflet. These were expected, as they are common features in a normal functioning mitral valve (Figure 82) and have been found in previous work [23]. At the commissures, the anterior and posterior leaflets fold over to form a seal. In the posterior leaflets, three regions, called scallops, exist, and folds typically form between the three scallops.

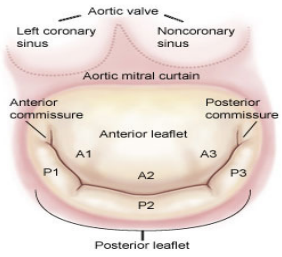

Figure 82 - Artist rendering of normal mitral valve coaptation, showing folds at the commissures and between the three regions of the posterior leaflet (P1, P2, and P3 on the diagram) [55].

Recalling the figures in section 6.1, coaptation and opening were successful for the subject model (MVs1) and partially successful for the patient model (MVp1), with a small hole between the leaflets. It is known that coaptation of the mitral valve leaflets occurs rapidly at the beginning of the systolic phase of the cardiac cycle, during the initial, sharp ramp up in pressure from approximately zero and is completed by the time the pressure reaches 130 kPa [56]. This behaviour was exhibited in these two models, with coaptation occurring at the expected time and pressures of the load curve. This result indicates that the dynamics of these two models corresponds well with the physiologic coaptation behaviour of the mitral valve [56].

As with coaptation, the subject and patient models showed similar behaviour with regards to opening, however opening occurred over a larger time period for both models. As expected, the valves began to open when the pressure dropped to 130 kPa and leaflet separation occurred at the end, as the pressure approached zero [56], [57]. The timing of valve opening and leaflet separation is a key aspect in validating the dynamics of the model, as it has been found that the leaflets edges separate at this point of the cardiac cycle [57]. The valves are partially open when the pressure curve reaches zero, which correlates well with literature indicating valve opening at this point [56]. Considering the coaptation and opening behaviours of these two models, their correlation with the physiological dynamics of the mitral valve validates these two models for simulating the dynamics of the natural mitral valve.

In the mitral valve repair models, coaptation did not appear to be affected by the alterations in the models. The delayed opening of the Alfieri stitch models is attributable to the restraint of the sutures, limiting the movement of the leaflets away from each other. This explanation for the delay is bolstered by the fact that the quadrangular resection model exhibited the same opening dynamics as the unrepaired model.

An interesting feature of the unrepaired patient model is the large fold in the posterior leaflet and the small hole between the fold and the anterior leaflet (Figure 52). As shown in Figure 53, there appears to be a hole, at the centre of the valve when the leaflets are closed, in the 3D TEE images that the geometric data was acquired from. The hole is an indication of dysfunction in the mitral valve, probably causing regurgitation. As the fold and hole in the patient model correlates with the hole in the ultrasound images, this provides additional validation of this modeling technique. The repair techniques affected this feature differently. The Alfieri stitches, with and without the annuloplasty ring, did not fully eliminate the fold, but the hole was absent. Alternatively, the quadrangular resection, in particular when combined with the annuloplasty ring, completely eliminated this dysfunction in the patient model.

7.1.2 Leaflet Stresses

The stress distribution in the leaflets was as expected, with a concentration of relatively higher stresses at the centre of the anterior leaflet and lower stresses in the posterior leaflet. This pattern of stress distribution is consistent with previous studies of the mitral valve, with the highest stresses at the centre of the anterior leaflet [22], [28], [41]. The

peak stresses at mid-systole in both leaflets are in agreement with those found in previous mitral valve models [22], [27] which used similar material properties, which provides validation for the models.

The Alfieri stitch mitral valve repairs did not have a significant effect on the principal stresses in the leaflets, following the same distribution as seen in the other models. One effect was a reduction in the 2nd principal stresses with the paracommissural stitch, in the side of the leaflet that had been sutured. Another result was the change in direction of the principal stress vectors in the anterior leaflet, with the longer vectors angled toward the unstitched side of the anterior leaflet. Unfortunately, previous work [16], [26], [27], [39] did not examine these techniques during the systolic phase, making validation difficult. In the diastolic phase, the stresses in the leaflets were lower than those found in prior studies of the double-orifice Alfieri stitch [27], [39]. This is likely due to the lack of modeling of the systolic phase, as it does not take into account the relaxation of the leaflets as the valve opens, which is evident in this study with the presence of compressive stresses in the diastolic phase.

In the quadrangular resection models, a small increase in stress was observed in the leaflets at the suture location, as expected. However, in diastole there was a large stress concentration in the anterior leaflet along the annulus in the annuloplasty ring model of the quadrangular resection. This is not an expected result, as the stresses in diastole should be minimal, and may be a result of the interaction between the two repair types modeled, the quadrangular resection and the annuloplasty ring.

An interesting observation from the principal stress plots is the low stress regions at the annulus and at the folds in the leaflets. At the annulus, the stresses were generally near zero or compressive in nature, likely as a result of the shrinking annulus from the beginning to the middle of the systolic phase of the cardiac cycle. The low stresses at the leaflet folds indicate these areas are not carrying the high pressure load from the contraction of the heart, which is as expected.

The few areas of the annulus where higher stresses were observed are possibly a result of the no-rotation boundary condition applied to the annulus nodes, which may cause undue bending in those elements. This was a necessary boundary condition, however, as allowing rotation at the annulus resulted in the leaflets wrapping around the annulus nodes during analysis. A possible solution to this would be to restrict rotation to only a set angle.

In examining the vector plots of the principal stresses, it is seen that the principal stresses are higher in the radial direction of the leaflets. Previous studies with idealized leaflet geometry have found that the principal stress vectors correlated with the collagen fibre directions in the anterior leaflet, i.e. oriented radially at the commissures and following the anterior leaflet free margin towards the opposite free margin in a circumferential fashion [22]. However, the principal stress directions in the posterior leaflet have been found in the past to be mostly radial, as they are in this study [22]. A possible reason for this discrepancy in the anterior leaflet is that the radial direction is simply stretched more along the radial direction at the centre of the leaflet. Also, it is possible that the

equibiaxial material testing used to determine the leaflets' mechanical behaviour may not fully describe their stress-strain properties when not under equibiaxial conditions. More testing would be needed, in different directions and at different deformation rates, to more accurately understand the properties of the leaflet tissue and their complex fibrous structure.

7.1.3 Chordae Tendinae Forces

In each model, the forces in the chordae tendinae fluctuated throughout the cardiac cycle, but the trend they followed was as expected. A study by Nielsen *et al*. found average forces of approximately 0.46 N in the chordae tendinae [58], based on measurements of normal porcine mitral valves, which is higher than those found in this study, as shown in Table 5. A possible reason for this is if the chordae tendinae forces in this model are spread over more chordae than in the Nielsen study, which would lower the force per chordae. Also, other studies have shown that the papillary muscle heads carry a load of 2.5 N at mid-systole [59]. When spread over twelve chordae per papillary muscle, this gives an average chordae force of 0.21 N, which is closer to those seen in the subject and patient models. Since the measurement of chordae forces in vivo is very difficult, with the possibility of a wide margin of error, it is not unreasonable to assume that the chordae tendinae forces found in this study agree with experimental data.

Table 5 - Average chordae tendinae forces at mid-systole (t = 0.02 s), and their percent errors, in the subject model and the patient model. Average chordae tendinae forces at mid-systole in the repair models included for comparison.

Model	Force [N ± N]	Percent Error (Nielsen [58])	Percent Error (Jensen [59])
MVs1	0.24 ± 0.17	-48 %	14 %
MVp1	0.18 ± 0.09	-61 %	-15 %
MVp1-DO	0.12 ± 0.09		
MVp1-DO-A	0.14 ± 0.1		
MVp1-PC	0.1 ± 0.06		
MVp1-PC-A	0.14 ± 0. 8		
MVp1-QR	0.16 ± 0.09		
MVp1-QR-A	0.15 ± 0.08		

The chordae tendinae forces in the repair models betray a limitation of the method of stitching the leaflets together in the models. As the chordae tendinae had to initially be removed from the model, to operate the leaflet stitching, to prevent excessive deformation in the brick elements, their reintroduction after stitching resulted in new, longer chordae tendinae. This in turn results in a lower tension within the chordae. However, the quadrangular resection models, which did not involve removing the chordae, also show a reduction in chordae tension as a result of the repair procedure.

7.1.4 Leaflet Bulging and Coaptation Length

Physiologically, normal mitral valve leaflets are typically flat when the valve is closed, showing a little amount of doming or bulging toward the atrium. The results in this study show some variation in bulging, particularly with the various repair techniques. The four Alfieri stitch models resulted in increases in the anterior leaflet bulging of 221% to 336%, with the annuloplasty models showing the largest increase. Increases in bulging of the posterior leaflet ranged from 140% to 308%, with the paracommissural Alfieri stitch models showing the greatest increases. The increase in bulging in the annuloplasty

models is most likely due to the smaller annulus forced on the valve by the annuloplasty ring, resulting in more leaflet material being available to fill the orifice. Another possible reason for the increase in all four models is the position of the leaflets at the start of the simulation, which is closer to the annulus plane. In the quadrangular resection models, the amount of bulging decreased in the anterior leaflet, which is a result of decreasing the posterior leaflet size and the annulus length: the anterior leaflet has to extend further across the valve to contact the posterior leaflet, resulting in the same pressure acting on a larger area of leaflet. However, the annuloplasty ring increased this bulging to just above the levels of the unrepaired valve, as a result of the reduced annulus size.

The coaptation lengths found for each model are indicative of differences in valve function. The low coaptation length in the patient model compared to that of the normal model correlates well with the differences in function between the normal and dysfunction valves, with the lower length indicating diminished coaptation. Each Alfieri stitch model increased coaptation length, with increases of approximately 680 % and 510 % in the double-orifice and paracommissural models, respectively. The addition of the annuloplasty ring further increased coaptation length by approximately 35 % for both Alfieri stitch models. These increases in coaptation length, to approximately the same length as in the normal valve model, show quantitatively the improvement in function in these models, as noted previously. The quadrangular resection model, without the annuloplasty ring, failed to increase coaptation length. However, the addition of the annuloplasty ring increased coaptation length by approximately 370 %, indicating thering may be very important in this type of repair, more so than in the Alfieri stitch models.

7.1.5 Suture Forces

The suture forces determined in this study varied considerably between repair techniques. Suture loads were highest in the double-orifice Alfieri stitch, with similar results in the paracommissural Alfieri stitch, while the loads were nearly zero in the quadrangular resection model. According to experiments by Nielsen *et al*., which measured the suture tension of double-orifice Alfieri stitches in ovine hearts over the cardiac cycle, peak suture loads should occur at the end of systole [60], as the valve is opening, reaching loads of 0.2 N to 0.3 N [60], [61]. This is inconsistent with the results of this study, wherein loads unexpectedly tended to diminish at the end of systole. However, during systole, Nielsen found suture loads averaging less then 0.1 N [60], which agrees well with the systolic suture loads found in the double-orifice Alfieri stitch. A possible reason for this discrepancy is the large coaptation lengths found in the Alfieri stitch models. As the pressure on the leaflets drops after mid-systole, the leaflets start separating, with the coaptation length gradually shortening until separation occurs at the free margin. In these models, by the time the leaflets separate, at which the suture load would be expected to climb, the pressure load is at or near zero and the leaflets are moving freely. Therefore, the leaflets and sutures may find an equilibrium, moving in such a way that the suture forces are minimized.

The suture loads in the quadrangular resection model were lower than expected. However, there is a reasonable explanation for the negligible forces in the sutures. In a quadrangular resection procedure, one goal is to minimize the tension in the sutures connecting the two leaflet edges together by modifying the geometry of the posterior

leaflet in such a way that the two edges are not pulling away from each other [5], [62], [63]. This is the case in this study, wherein the two leaflet edges are under zero stress when the leaflets are stitched and do not tend to pull away from each other throughout the cardiac cycle.

7.2 Conclusions

7.2.1 Outcomes

The objectives of this study were to develop methods for constructing finite element models of the mitral valve and mitral valve repair from patient-specific data. Firstly, a method was described for processing geometric data extracted from 3D TEE and 3D TTE images into three dimensional models of the mitral valve, based on the data of a subject and a patient, for finite element analysis. The non-linear, transversely isotropic material properties of the mitral valve tissues were implemented using strain energy theory for hyperelastic materials. The implementation of the material properties in the dynamic finite element solver LS-DYNA was verified. Analysis of the two models showed normal function in the subject's mitral valve and dysfunctional behaviour in the patient's mitral valve, which was evident in the 3D TEE images. The dynamics of the valve and principal stresses agreed with the literature, validating these models as tools for simulating mitral valve dynamics.

Secondly, four types of mitral valve repair were successfully simulated using the patient model: annuloplasty ring, double-orifice and paracommissural Alfieri stitches, and

quadrangular resection. The quadrangular resection model is the first such model developed and was the most successful in eliminating the valve dysfunction found in the initial patient model. Each repair model was simulated through the entire cardiac cycle, a change from prior studies of the Alfieri stitch which only looked at the diastolic phase. This is important for modeling mitral valve repair, as the systolic phase of the cardiac cycle exerts stresses on the leaflets which affect valve behaviour leading into the diastolic phase. The Alfieri stitch models showed similar results as those of prior studies, with low stresses in diastole and a marginal increase in stress near the sutures. Each repair technique did not affect coaptation, but the Alfieri stitch models delayed the opening of the valve at the end of the systolic phase. These first generation models of mitral valve repair could be further studied and developed to examine the effects of various parameters on valve function.

7.2.2 Possibilities for Future Work

There are a few avenues for future work using the models of this study. The mitral valve repair models could be used to help cardiac surgeons find the effects of various iterations of a repair technique and to optimize those repairs. Using the annuloplasty model it would be possible to investigate the effects of different ring sizes on valve function and the success of mitral valve repairs. This could give surgeons a tool for determining what ring size relative to the annulus size would be best for certain degrees of coaptation. Additionally, the method used in applying the annuloplasty ring to the annulus could be used to test the many types of annuloplasty rings available to a surgeon and could even help in the development of newer, better rings.

Similar studies could be done with the other types of repair, such as finding the optimum leaflet length over which to apply the Alfieri stitch, the optimum location for stitching the leaflets together, and examining the effects of resection in different sections of the leaflets. The same methods used for implementing the repairs in this study could be used for studying many different iterations of these repairs, as well as in the development of new techniques.

Another possibility is the inclusion of fluid flow in the models, using fluid-structure interaction methods. Including fluid flow could be useful in optimizing the Alfieri stitch repairs by finding the length and location of stitch that facilitates the refilling of the left ventricle the best, during the diastolic phase of the cardiac cycle.

The patient-specific nature of the model could be improved by investigating the use of patient-specific load curves and disease specific material properties. Everyone's heart is different, so a method of obtaining the transvalvular pressure gradient at the same time as acquiring the ultrasound images would improve the accuracy of the model. Also, some mitral valve diseases affect the material properties of the valve tissues, so material testing of diseased mitral valves could also help improve the validity of the models.

These are just some of the many possibilities for future work based on this study. There are many different studies that could be performed using the models herein and perhaps in the future some of these will be undertaken.

References

References

[1] E. Pierce, "Diagram of the human heart.," *Wikipedia*, 2006. [Online]. Available: http://en.wikipedia.org/wiki/File:Diagram_of_the_human_heart.svg. [Accessed: 31-Jan-2010].

[2] A. Pick, "'What is the mitral valve annulus?'," *The Patient's Guide to Heart Valve Surgery*, 2008. [Online]. Available: http://www.heart-valve-surgery.com/heart-surgery-blog/2008/09/02/mitral-valve-annulus-definition-diagrams-prolapse-calcification-treatment/. [Accessed: 11-Dec-2001].

[3] Z. G. Turi, "Mitral Valve Disease ," *Circulation* , vol. 109, no. 6, p. e38-e41, Feb. 2004.

[4] J. Fann, N. Ingels Jr., and D. Miller, *Cardiac Surgery in the Adult*. New York: McGraw-Hill, 2003.

[5] L. M. Gazoni et al., "A Simplified Approach to Degenerative Disease: Triangular Resections of the Mitral Valve," *The Annals of Thoracic Surgery*, vol. 83, no. 5, pp. 1658-1665, May. 2007.

[6] A. M. Gillinov et al., "Is prosthetic anuloplasty necessary for durable mitral valve repair?," *The Annals of thoracic surgery*, vol. 88, no. 1, pp. 76-82, Jul. 2009.

[7] "Posterior Leaflet Prolapse," *Mitral Valve Repair Center at The Mount Sinai Hospital*, 2010. [Online]. Available: http://www.mitralvalverepair.org/content/view/66/. [Accessed: 11-Dec-2011].

[8] O. Alfieri, F. Maisano, and M. De Bonis, "The edge-to-edge repair," *Multimedia Manual of Cardiothoracic Surgery*, vol. 2005, no. 809, p. 869, Aug. 2005.

[9] P. Perier, "Quadrangular resection for repair of posterior leaflet prolapse," *Multimedia Manual of Cardiothoracic Surgery*, vol. 2005, no. 1129, p. 893, Nov. 2005.

[10] K. S. Kunzelman, R. P. Cochran, C. Chuong, W. S. Ring, E. D. Verrier, and R. D. Eberhart, "Finite element analysis of the mitral valve.," *The Journal of heart valve disease*, vol. 2, no. 3, pp. 326-340, 1993.

[11] M. S. Reimink, K. S. Kunzelman, E. D. Verrier, and R. P. Cochran, "The effect of anterior chordal replacement on mitral valve function and stresses. A finite element study," *ASAIO Journal*, vol. 41, no. 3, 1995.

[12] K. Kunzelman, M. S. Reimink, E. D. Verrier, and R. P. Cochran, “Replacement of Mitral Valve Posterior Chordae Tendineae with Expanded Polytetrafluoroethylene Suture: A Finite Element Study,” *Journal of Cardiac Surgery*, vol. 11, no. 2, pp. 136-145, 1996.

[13] K. S. Kunzelman, M. S. Reimink, and R. P. Cochran, “Annular dilatation increases stress in the mitral valve and delays coaptation: A finite element computer model,” *Cardiovascular Surgery*, vol. 5, no. 4, pp. 427-434, 1997.

[14] F. Maisano, A. Redaelli, G. Pennati, R. Fumero, L. Torracca, and O. Alfieri, “The hemodynamic effects of double-orifice valve repair for mitral regurgitation: A 3D computational model,” *European Journal of Cardio-thoracic Surgery*, vol. 15, no. 4, pp. 419-425, 1999.

[15] A. Redaelli, G. Guadagni, R. Fumero, F. Maisano, and O. Alfieri, “A computational study of the hemodynamics after ‘edge-to-edge’ mitral valve repair,” *Journal of Biomechanical Engineering*, vol. 123, no. 6, pp. 565-570, 2001.

[16] E. Votta et al., “3-D computational analysis of the stress distribution on the leaflets after edge-to-edge repair of mitral regurgitation.,” *The Journal of heart valve disease*, vol. 11, no. 6, p. 810, 2002.

[17] F. Maisano, A. Redaelli, M. Soncini, E. Votta, L. Arcobasso, and O. Alfieri, “An annular prosthesis for the treatment of functional mitral regurgitation: Finite element model analysis of a dog bone-shaped ring prosthesis,” *Annals of Thoracic Surgery*, vol. 79, no. 4, pp. 1268-1275, 2005.

[18] E. Votta, F. Maisano, S. F. Bolling, O. Alfieri, F. M. Montevecchi, and A. Redaelli, “The Geoform Disease-Specific Annuloplasty System: A Finite Element Study,” *Annals of Thoracic Surgery*, vol. 84, no. 1, pp. 92-101, 2007.

[19] E. Votta, E. Caiani, F. Veronesi, M. Soncini, F. M. Montevecchi, and A. Redaelli, “Mitral valve finite-element modelling from ultrasound data: A pilot study for a new approach to understand mitral function and clinical scenarios,” *Philosophical Transactions of the Royal Society A: Mathematical, Physical and Engineering Sciences*, vol. 366, no. 1879, pp. 3411-3434, 2008.

[20] M. Stevanella, G. Krishnamurthy, E. Votta, J. C. Swanson, A. Redaelli, and N. B. Ingels, “Mitral leaflet modeling: Importance of in vivo shape and material properties.,” *Journal of biomechanics*, vol. 44, no. 12, pp. 2229-2235, Aug. 2011.

[21] C. A. Conti et al., “Mitral Valve Modelling in Ischemic Patients : Finite Element Analysis from Cardiac Magnetic Resonance Imaging CNR Institute of Clinical Physiology , Pisa , Italy,” *Cardiology*, vol. 37, pp. 1059-1062, 2010.

[22] V. Prot, R. Haaverstad, and B. Skallerud, “Finite element analysis of the mitral apparatus: Annulus shape effect and chordal force distribution,” *Biomechanics and Modeling in Mechanobiology*, vol. 8, no. 1, pp. 43-55, 2009.

[23] V. Prot and B. Skallerud, “Nonlinear solid finite element analysis of mitral valves with heterogeneous leaflet layers,” *Computational Mechanics*, vol. 43, no. 3, pp. 353-368, Jul. 2008.

[24] K. Kunzelman, R. Cochran, S. Murphree, W. Ring, E. Verrier, and R. Eberhart, “Differential collagen distribution in the mitral valve and its influence on biomechanical behaviour.,” *Journal of Heart Valve Disease*, vol. 2, no. 2, pp. 236-244, 1993.

[25] I. S. Salgo et al., “Effect of annular shape on leaflet curvature in reducing mitral leaflet stress,” *Circulation*, vol. 106, no. 6, pp. 711-717, 2002.

[26] A. Avanzini, “A computational procedure for prediction of structural effects of edge-to-edge repair on mitral valve,” *Journal of Biomechanical Engineering*, vol. 130, no. 3, 2008.

[27] F. Dal Pan, G. Donzella, C. Fucci, and M. Schreiber, “Structural effects of an innovative surgical technique to repair heart valve defects,” *Journal of Biomechanics*, vol. 38, no. 12, pp. 2460-2471, 2005.

[28] K. Lau, V. Diaz, P. Scambler, and G. Burriesci, “Mitral valve dynamics in structural and fluid-structure interaction models,” *Medical Engineering and Physics*, vol. 32, no. 9, pp. 1057-1064, 2010.

[29] K. May-Newman and F. C. Yin, “A constitutive law for mitral valve tissue.,” *Journal of biomechanical engineering*, vol. 120, no. 1, pp. 38-47, Feb. 1998.

[30] L. Chen, F. C.-P. Yin, and K. May-Newman, “The Structure and Mechanical Properties of the Mitral Valve Leaflet-Strut Chordae Transition Zone,” *Journal of Biomechanical Engineering*, vol. 126, no. 2, p. 244, 2004.

[31] K. May-Newman and F. C. Yin, “Biaxial mechanical behavior of excised porcine mitral valve leaflets,” *American Journal of Physiology - Heart and Circulatory Physiology*, vol. 269, no. 4, p. H1319-H1327, Oct. 1995.

[32] J. E. Barber, F. K. Kasper, N. B. Ratliff, D. M. Cosgrove, B. P. Griffin, and I. Vesely, “Mechanical properties of myxomatous mitral valves,” *The Journal of Thoracic and Cardiovascular Surgery*, vol. 122, no. 5, pp. 955-962, Nov. 2001.

[33] Y. C. Fung, K. Fronek, and P. Patitucci, “Pseudoelasticity of arteries and the choice of its mathematical expression ,” *American Journal of Physiology - Heart and Circulatory Physiology* , vol. 237, no. 5, p. H620-H631, Nov. 1979.

[34] D. R. Einstein, P. Reinhall, M. Nicosia, R. P. Cochran, and K. Kunzelman, "Dynamic finite element implementation of nonlinear, anisotropic hyperelastic biological membranes.," *Computer methods in biomechanics and biomedical engineering*, vol. 6, no. 1, pp. 33-44, 2003.

[35] D. R. Einstein, K. S. Kunzelman, P. G. Reinhall, M. A. Nicosia, and R. P. Cochran, "Haemodynamic determinants of the mitral valve closure sound: A finite element study," *Medical and Biological Engineering and Computing*, vol. 42, no. 6, pp. 832-846, 2004.

[36] D. R. Einstein, K. S. Kunzelman, P. G. Reinhall, M. A. Nicosia, and R. P. Cochran, "The relationship of normal and abnormal microstructural proliferation to the mitral valve closure sound," *Journal of Biomechanical Engineering*, vol. 127, no. 1, pp. 134-147, 2005.

[37] V. Prot, B. Skallerud, and G. A. Holzapfel, "Transversely isotropic membrane shells with application to mitral valve mechanics. Constitutive modelling and finite element implementation," *International Journal for Numerical Methods in Engineering*, vol. 71, no. 8, pp. 987-1008, 2007.

[38] G. A. Holzapfel, G. Sommer, C. T. Gasser, and P. Regitnig, "Determination of layer-specific mechanical properties of human coronary arteries with nonatherosclerotic intimal thickening and related constitutive modeling ," *American Journal of Physiology - Heart and Circulatory Physiology* , vol. 289, no. 5, p. H2048-H2058, Nov. 2005.

[39] K. D. Lau, V. Díaz-Zuccarini, P. Scambler, and G. Burriesci, "Fluid-structure interaction study of the edge-to-edge repair technique on the mitral valve.," *Journal of biomechanics*, vol. 44, pp. 2409-2417, Jul. 2011.

[40] B. Skallerud, V. Prot, and I. Nordrum, "Modeling active muscle contraction in mitral valve leaflets during systole: A first approach," *Biomechanics and Modeling in Mechanobiology*, vol. 10, no. 1, pp. 11-26, 2011.

[41] K. S. Kunzelman, D. R. Einstein, and R. P. Cochran, "Fluid-structure interaction models of the mitral valve: function in normal and pathological states.," *Philosophical transactions of the Royal Society of London. Series B, Biological sciences*, vol. 362, no. 1484, pp. 1393-406, Aug. 2007.

[42] O. Alfieri et al., "The double-orifice technique in mitral valve repair: a simple solution for complex problems.," *The Journal of thoracic and cardiovascular surgery*, vol. 122, no. 4, pp. 674-81, Oct. 2001.

[43] J. D. Humphrey, *Cardiovascular Solid Mechanics: Cells, Tissues, and Organs*. New York: Springer-Verlag, 2002.

[44] J. M. Guccione, A. D. McCulloch, and L. K. Waldman, “Passive material properties of intact ventricular myocardium determined from a cylindrical model,” *Journal of Biomechanical Engineering*, vol. 113, no. 1, pp. 42-55, 1991.

[45] M. R. Labrosse, C. J. Beller, T. Mesana, and J. P. Veinot, “Mechanical behavior of human aortas: Experiments, material constants and 3-D finite element modeling including residual stress.,” *Journal of biomechanics*, vol. 42, no. 8, pp. 996-1004, May. 2009.

[46] M. R. Labrosse, K. Lobo, and C. J. Beller, “Structural analysis of the natural aortic valve in dynamics: from unpressurized to physiologically loaded.,” *Journal of biomechanics*, vol. 43, no. 10, pp. 1916-22, Jul. 2010.

[47] C. Millington-Sanders, A. Meir, L. Lawrence, and C. Stolinski, “Structure of chordae tendineae in the left ventricle of the human heart.,” *Journal of anatomy*, vol. 192, pp. 573-81, May. 1998.

[48] J. Ritchie, J. Jimenez, Z. He, M. S. Sacks, and A. P. Yoganathan, “The material properties of the native porcine mitral valve chordae tendineae: an in vitro investigation.,” *Journal of biomechanics*, vol. 39, no. 6, pp. 1129-1135, Jan. 2006.

[49] P. Dagum et al., “Coordinate-free analysis of mitral valve dynamics in normal and ischemic hearts.,” *Circulation*, vol. 102, no. 19 Suppl 3, pp. III62-9, Nov. 2000.

[50] D. Ozbag, Y. Gumusalan, and A. Demirant, “The comparative investigation of morphology of papillary muscles of left ventricle in different species,” *International Journal*, no. May, pp. 529-536, 2005.

[51] F. Musyoki, “The EKG Waveform,” *Molson Medical Informatics Project*, 2000. [Online]. Available: http://sprojects.mmi.mcgill.ca/cardiophysio/EKGwiggers.htm. [Accessed: 16-Dec-2010].

[52] P. B. Dobrin, “Some mechanical properties of polypropylene sutures: relationship to the use of polypropylene in vascular surgery,” *Journal of Surgical Research*, vol. 45, no. 6, pp. 568–573, 1988.

[53] M. Deng and J. Zhou, “Density Determination of Medical Sutures by Pycnometry,” *International Journal of Polymer Analysis and Characterization*, vol. 8, no. 6, pp. 411-415, 2003.

[54] “Mitral Valve Surgery: Mitral Repair - Our Grand Experience,” *German Hospital Tirana*, 2011. [Online]. Available: http://www.german-hospital-tirana.com/index-MED5.html. [Accessed: 20-Apr-2011].

[55] "Mitral Annulus," *Mitral Valve Repair Center at The Mount Sinai Hospital*, 2010. [Online]. Available: http://www.mitralvalverepair.org/content/view/54/. [Accessed: 13-Dec-2011].

[56] T. Barker and I. Wilson, *Mitral Valve Surgery*. New York: Springer-Verlag, 2011, p. 11.

[57] M. O. Karlsson et al., "Mitral valve opening in the ovine heart," *American Journal of Physiology - Heart and Circulatory Physiology*, vol. 274, no. 2, p. H552-H563, Feb. 1998.

[58] S. L. Nielsen et al., "Chordal force distribution determines systolic mitral leaflet configuration and severity of functional mitral regurgitation," *Journal of the American College of Cardiology*, vol. 33, no. 3, pp. 843-853, Mar. 1999.

[59] M. Jensen, A. Fontaine, and A. Yoganathan, "Improved In Vitro Quantification of the Force Exerted by the Papillary Muscle on the Left Ventricular Wall: Three-Dimensional Force Vector Measurement System," *Annals of Biomedical Engineering*, vol. 29, no. 5, pp. 406-413, May. 2001.

[60] S. L. Nielsen et al., "Edge-to-Edge Mitral Repair: Tension on the Approximating Suture and Leaflet Deformation During Acute Ischemic Mitral Regurgitation in the Ovine Heart," *Circulation*, vol. 104, no. 1, p. I-29-I-35, Sep. 2001.

[61] T. Timek et al., "Mitral annular size predicts Alfieri stitch tension in mitral edge-to-edge repair.," *J Heart Valve Dis.*, vol. 13, no. 2, pp. 165-173, 2004.

[62] P. Perier, "Quadrangular resection for repair of posterior leaflet prolapse," *Multimedia Manual of Cardiothoracic Surgery*, 2005.

[63] A. M. Gillinov and D. M. Cosgrove III, "Modified quadrangular resection for mitral valve repair," *The Annals of Thoracic Surgery*, vol. 72, no. 6, pp. 2153-2154, Dec. 2001.

Appendices

A MATLAB Programs

A.1 Ultrasound Image Processing

This program is used to select points identifying the mitral valve structures from the ultrasound images.

```
clear;

user_entry = input('File name ? :','s');

if strncmp(user_entry, '000', 3) == 1
    theta = 0;
    savefile = '000.txt';
    n = 1;
end
if strncmp(user_entry, '010', 3) == 1
    theta = 10;
    savefile = '010.txt';
    n = 2;
end
if strncmp(user_entry, '020', 3) == 1
    theta = 20;
    savefile = '020.txt';
    n = 3;
end
if strncmp(user_entry, '030', 3) == 1
    theta = 30;
    savefile = '030.txt';
    n = 4;
end
if strncmp(user_entry, '040', 3) == 1
    theta = 40;
    savefile = '040.txt';
    n = 5;
end
if strncmp(user_entry, '050', 3) == 1
    theta = 50;
    savefile = '050.txt';
    n = 6;
end
if strncmp(user_entry, '060', 3) == 1
    theta = 60;
    savefile = '060.txt';
    n = 7;
end
if strncmp(user_entry, '070', 3) == 1
    theta = 70;
    savefile = '070.txt';
    n = 8;
end
if strncmp(user_entry, '080', 3) == 1
    theta = 80;
    savefile = '080.txt';
    n = 9;
end
if strncmp(user_entry, '090', 3) == 1
```

```
    theta = 90;
    savefile = '090.txt';
    n = 10;
end
if strncmp(user_entry, '100', 3) == 1
    theta = 100;
    savefile = '100.txt';
    n = 11;
end
if strncmp(user_entry, '110', 3) == 1
    theta = 110;
    savefile = '110.txt';
    n = 12;
end
if strncmp(user_entry, '120', 3) == 1
    theta = 120;
    savefile = '120.txt';
    n = 13;
end
if strncmp(user_entry, '130', 3) == 1
    theta = 130;
    savefile = '130.txt';
    n = 14;
end
if strncmp(user_entry, '140', 3) == 1
    theta = 140;
    savefile = '140.txt';
    n = 15;
end
if strncmp(user_entry, '150', 3) == 1
    theta = 150;
    savefile = '150.txt';
    n = 16;
end
if strncmp(user_entry, '160', 3) == 1
    theta = 160;
    savefile = '160.txt';
    n = 17;
end
if strncmp(user_entry, '170', 3) == 1
    theta = 170;
    savefile = '170.txt';
    n = 18;
end

mitral=imshow(user_entry, 'InitialMagnification', 67);

h8 = impoint(gca,250,100);
api8 = iptgetapi(h8);
api8.setString('8')

h7 = impoint(gca,220,100);
api7 = iptgetapi(h7);
api7.setString('7')

h6 = impoint(gca,190,100);
api6 = iptgetapi(h6);
api6.setString('6')

h5 = impoint(gca,160,100);
api5 = iptgetapi(h5);
api5.setString('5')
```

```
h4 = impoint(gca,130,100);
api4 = iptgetapi(h4);
api4.setString('4')

h3 = impoint(gca,100,100);
api3 = iptgetapi(h3);
api3.setString('3')

h2 = impoint(gca,70,100);
api2 = iptgetapi(h2);
api2.setString('2')

h1 = impoint(gca,40,100);
api1 = iptgetapi(h1);
api1.setString('1')

api1.addNewPositionCallback(@(a) save('data.dat', 'a', '-ASCII'));
pause;
load data.dat;
xy1=data;
clear a data;

api2.addNewPositionCallback(@(a) save('data.dat', 'a', '-ASCII'));
pause;
load data.dat;
xy2=data;
clear a data;

api3.addNewPositionCallback(@(a) save('data.dat', 'a', '-ASCII'));
pause;
load data.dat;
xy3=data;
clear a data;

api4.addNewPositionCallback(@(a) save('data.dat', 'a', '-ASCII'));
pause;
load data.dat;
xy4=data;
clear a data;

api5.addNewPositionCallback(@(a) save('data.dat', 'a', '-ASCII'));
pause;
load data.dat;
xy5=data;
clear a data;

api6.addNewPositionCallback(@(a) save('data.dat', 'a', '-ASCII'));
pause;
load data.dat;
xy6=data;
clear a data;

api7.addNewPositionCallback(@(a) save('data.dat', 'a', '-ASCII'));
pause;
load data.dat;
xy7=data;
clear a data;

api8.addNewPositionCallback(@(a) save('data.dat', 'a', '-ASCII'));
pause;
load data.dat;
xy8=data;
clear a data;
```

```
if (xy7(1,1) < 100) & (xy7(1,2) < 100)
    xy7 = xy1;
end
if (xy8(1,1) < 100) & (xy8(1,2) < 100)
    xy8 = xy1;
end

alpha = (atan((xy2(1,2)-xy1(1,2))/(xy2(1,1)-xy1(1,1))));

fid = fopen(savefile, 'wt');

rtz1(1,1)=-cos(alpha)*(xy3(1,1)-xy1(1,1))-sin(alpha)*(xy3(1,2)-xy1(1,2));
rtz1(1,2)=theta;
rtz1(1,3)=sin(alpha)*(xy3(1,1)-xy1(1,1))-cos(alpha)*(xy3(1,2)-xy1(1,2));
fprintf(fid, 'tnrz( %g, 1, 1)= %6.2f\n', n, rtz1(1,2));
fprintf(fid, 'tnrz( %g, 1, 2)= %g\n', n, 1);
fprintf(fid, 'tnrz( %g, 1, 3)= %10.2f\n', n, rtz1(1,1));
fprintf(fid, 'tnrz( %g, 1, 4)= %10.2f\n', n, rtz1(1,3));

rtz2(1,1)=-cos(alpha)*(xy4(1,1)-xy1(1,1))-sin(alpha)*(xy4(1,2)-xy1(1,2));
rtz2(1,2)=theta;
rtz2(1,3)=sin(alpha)*(xy4(1,1)-xy1(1,1))-cos(alpha)*(xy4(1,2)-xy1(1,2));
fprintf(fid, 'tnrz( %g, 2, 1)= %6.2f\n', n, rtz2(1,2));
fprintf(fid, 'tnrz( %g, 2, 2)= %g\n', n, 2);
fprintf(fid, 'tnrz( %g, 2, 3)= %10.2f\n', n, rtz2(1,1));
fprintf(fid, 'tnrz( %g, 2, 4)= %10.2f\n', n, rtz2(1,3));

rtz3(1,1)=-cos(alpha)*(xy5(1,1)-xy1(1,1))-sin(alpha)*(xy5(1,2)-xy1(1,2));
rtz3(1,2)=theta;
rtz3(1,3)=sin(alpha)*(xy5(1,1)-xy1(1,1))-cos(alpha)*(xy5(1,2)-xy1(1,2));
fprintf(fid, 'tnrz( %g, 3, 1)= %6.2f\n', n, rtz3(1,2));
fprintf(fid, 'tnrz( %g, 3, 2)= %g\n', n, 3);
fprintf(fid, 'tnrz( %g, 3, 3)= %10.2f\n', n, rtz3(1,1));
fprintf(fid, 'tnrz( %g, 3, 4)= %10.2f\n', n, rtz3(1,3));

rtz4(1,1)=-cos(alpha)*(xy6(1,1)-xy1(1,1))-sin(alpha)*(xy6(1,2)-xy1(1,2));
rtz4(1,2)=theta;
rtz4(1,3)=sin(alpha)*(xy6(1,1)-xy1(1,1))-cos(alpha)*(xy6(1,2)-xy1(1,2));
fprintf(fid, 'tnrz( %g, 4, 1)= %6.2f\n', n, rtz4(1,2));
fprintf(fid, 'tnrz( %g, 4, 2)= %g\n', n, 4);
fprintf(fid, 'tnrz( %g, 4, 3)= %10.2f\n', n, rtz4(1,1));
fprintf(fid, 'tnrz( %g, 4, 4)= %10.2f\n', n, rtz4(1,3));

rtz5(1,1)=-cos(alpha)*(xy7(1,1)-xy1(1,1))-sin(alpha)*(xy7(1,2)-xy1(1,2));
rtz5(1,2)=theta;
rtz5(1,3)=sin(alpha)*(xy7(1,1)-xy1(1,1))-cos(alpha)*(xy7(1,2)-xy1(1,2));
fprintf(fid, 'tnrz( %g, 5, 1)= %6.2f\n', n, rtz5(1,2));
fprintf(fid, 'tnrz( %g, 5, 2)= %g\n', n, 5);
fprintf(fid, 'tnrz( %g, 5, 3)= %10.2f\n', n, rtz5(1,1));
fprintf(fid, 'tnrz( %g, 5, 4)= %10.2f\n', n, rtz5(1,3));

rtz6(1,1)=-cos(alpha)*(xy8(1,1)-xy1(1,1))-sin(alpha)*(xy8(1,2)-xy1(1,2));
rtz6(1,2)=theta;
rtz6(1,3)=sin(alpha)*(xy8(1,1)-xy1(1,1))-cos(alpha)*(xy8(1,2)-xy1(1,2));
fprintf(fid, 'tnrz( %g, 6, 1)= %6.2f\n', n, rtz6(1,2));
fprintf(fid, 'tnrz( %g, 6, 2)= %g\n', n, 6);
fprintf(fid, 'tnrz( %g, 6 ,3)= %10.2f\n', n, rtz6(1,1));
fprintf(fid, 'tnrz( %g, 6, 4)= %10.2f\n', n, rtz6(1,3));

fclose(fid);
```

A.2 Geometric Reconstruction and FE Model Construction

A.2.1 Main Program

This program creates the geometric reconstruction of the mitral valve, converts it into a finite element model, and creates an input file for analysis in LS-DYNA.

```
function geobrick
clear
clc

%MITRAL VALVE FINITE ELEMENT MODEL
%
% This file generates the nodes and brick elements for a FE model of the Mitral
Valve.
% A LS-DYNA input file is then created containing the nodes and elements.

global a fm ap pp p1 p4
        % creates global variables for the coordinates
        % a = annulus coordinates
        % fm = free margin coordinates
        % ap = anterior papillary muscle coordinates
        % pp = posterior papillary muscle coordinates

importdata;    %imports the coordinates to a, fm, apm, and ppm

esize=1.4;  %element size along circumference of annulus
ndivr=14; %# divisions along radius
t=0.55;   % leaflet thickness

%-------------------------------------------------------------------------------
%----------- GENERATE MITRAL VALVE LEAFLETS ------------------------------------

%create annulus and free margin splines from the data
a=spline(a,36,3600);
fm=spline(fm,36,3600);

%smooth the splines
a=smooth(a,3,3600,80);
fm=smooth(fm,6,3600,80);

%create new splines
a=spline(a,80,8000);
fm=spline(fm,80,8000);

%create the anterior and posterior leaflets
max_norml=0;
for i=1:10:8000
    for j=1:10:8000
        p11(1,:)=a(i,:);
        p22(1,:)=a(j,:);
        l(1,:)=p22(1,:)-p11(1,:);
        norml=norm(l);
        if norml>max_norml
            i1=i;
            i2=j;
            max_norml=norml;
        end
```

```
    end
end

%split_nodes=split(a,fm,i1,i2); %#ok<NASGU>
if i2>i1
    max_i=i2-200;
    min_i=i1-500;
else
    max_i=i1-200;
    min_i=i2-500;
end
postsize=max_i-min_i;
antsize=(8000-max_i)+min_i;
a_post=zeros(postsize,3);
a_ant=zeros(antsize,3);
fm_post=zeros(postsize,3);
fm_ant=zeros(antsize,3);

%1=posterior leaflet
%2=anterior leaflet
for i=1:1:postsize+1
    a_post(i,:)=a(i+(min_i-1),1:3);
    fm_post(i,:)=fm(i+(min_i-1),1:3);
    a(i+(min_i-1),4)=1;
    fm(i+(min_i-1),4)=1;
end
for i=1:1:(antsize-min_i)+1
    a_ant(i,:)=a(i+(max_i-1),1:3);
    fm_ant(i,:)=fm(i+(max_i-1),1:3);
    a(i+(max_i-1),4)=2;
    fm(i+(max_i-1),4)=2;
end
for i=((antsize-min_i)+1):1:antsize
    a_ant(i,:)=a(i-(antsize-min_i),1:3);
    fm_ant(i,:)=fm(i-(antsize-min_i),1:3);
    a(i-(antsize-min_i),4)=2;
    fm(i-(antsize-min_i),4)=2;
end
%anterior and posterior leaflets created

%--- Create the papillary muscle heads.
%--- Clean the input data to eliminate '0' values.
apm=zeros(1,3);
ppm=zeros(1,3);
for j=1:1:2
    if j==1
        k=0;
        for i=1:1:18
            if ap(i,:)==0
                k=k+1;
            else
                apm(i-k,:)=ap(i,:);
            end
        end
    else
        k=0;
        for i=1:1:18
            if pp(i,:)==0
                k=k+1;
            else
                ppm(i-k,:)=pp(i,:);
            end
        end
```

```
    end
end

%--- Create the papillary muscle heads using the spline tool.
sa=size(apm);
sp=size(ppm);
apm=pm_spline(apm,sa(1,1),(sa(1,1)-1)*100);
p1apm=p1;
p4apm=p4;
ppm=pm_spline(ppm,sp(1,1),(sp(1,1)-1)*100);
p1ppm=p1;
p4ppm=p4;
% ----------- END ---------------------------------------------------------
%-------------------------------------------------------------------------
%----------- GENERATE BRICK ELEMENTS ---------------------------------------

%Create splines along annulus, just inside and outside the current spline
% for the brick elements
ai=zeros(8000,4);
am=a;
ao=zeros(8000,4);

for i=1:1:8000
    if i==1
        r1=am(2,1:3)-am(8000,1:3);
    elseif i==8000
        r1=am(1,1:3)-am(i-1,1:3);
    else
        r1=am(i+1,1:3)-am(i-1,1:3);
    end
    r2=fm(i,1:3)-am(i,1:3);
    r3o=cross(r2,r1);
    r3i=cross(r1,r2);
    uo=r3o/norm(r3o);
    ui=r3i/norm(r3i);
    ao(i,1:3)=(t/2)*uo+am(i,1:3);
    ai(i,1:3)=(t/2)*ui+am(i,1:3);
    ao(i,4)=am(i,4);
    ai(i,4)=am(i,4);
end

%Create splines along free margin, just inside and outside the current spline
% for the brick elements
fmi=zeros(8000,4);
fmm=fm;
fmo=zeros(8000,4);

for i=1:1:8000
    if i==1
        r1=fmm(2,1:3)-fmm(8000,1:3);
    elseif i==8000
        r1=fmm(1,1:3)-fmm(i-1,1:3);
    else
        r1=fmm(i+1,1:3)-fmm(i-1,1:3);
    end
    r2=fmm(i,1:3)-am(i,1:3);
    r3o=cross(r2,r1);
    r3i=cross(r1,r2);
    uo=r3o/norm(r3o);
    ui=r3i/norm(r3i);
    fmo(i,1:3)=(t/2)*uo+fmm(i,1:3);
    fmi(i,1:3)=(t/2)*ui+fmm(i,1:3);
    fmo(i,4)=fmm(i,4);
```

```
    fmi(i,4)=fmm(i,4);
end

%determine number of nodes along annulus based on the element size 'esize'
length=0;
for i=1:1:7999
    l(1,:)=am(i+1,1:3)-am(i,1:3);
    length=length+norm(l);
end
ndiv=floor(length/esize);
ndiv_ant=floor((antsize/8000)*ndiv);
ndiv_post=ndiv-ndiv_ant;

%create nodes along the annulus and free margin of the posterior leaflet
post_h=floor(postsize/ndiv_post);
ant_h=floor(antsize/ndiv_ant);
b=1;
n_ao=zeros(1,4);
n_am=zeros(1,4);
n_ai=zeros(1,4);
n_fmo=zeros(1,4);
n_fmm=zeros(1,4);
n_fmi=zeros(1,4);
for i=min_i:post_h:max_i
    if (max_i-i)<post_h
        i=max_i;
    end
    n_ao(b,:)=ao(i,:);
    n_am(b,:)=am(i,:);
    n_ai(b,:)=ai(i,:);
    n_fmo(b,:)=fmo(i,:);
    n_fmm(b,:)=fmm(i,:);
    n_fmi(b,:)=fmi(i,:);
    b=b+1;
end
for i=max_i+ant_h:ant_h:8000
        if (8000-i)<ant_h
            r=ant_h-(8000-i);
            n_ao(b,:)=ao(i,:);
            n_am(b,:)=am(i,:);
            n_ai(b,:)=ai(i,:);
            n_fmo(b,:)=fmo(i,:);
            n_fmm(b,:)=fmm(i,:);
            n_fmi(b,:)=fmi(i,:);
            b=b+1;
        else
            n_ao(b,:)=ao(i,:);
            n_am(b,:)=am(i,:);
            n_ai(b,:)=ai(i,:);
            n_fmo(b,:)=fmo(i,:);
            n_fmm(b,:)=fmm(i,:);
            n_fmi(b,:)=fmi(i,:);
            b=b+1;
        end
end
for i=r:ant_h:min_i
    if (min_i-i)>ant_h
        n_ao(b,:)=ao(i,:);
        n_am(b,:)=am(i,:);
        n_ai(b,:)=ai(i,:);
        n_fmo(b,:)=fmo(i,:);
        n_fmm(b,:)=fmm(i,:);
        n_fmi(b,:)=fmi(i,:);
```

```
        b=b+1;
    end
end

%create nodes across leaflets
n_ro=zeros(1,4);
n_rm=zeros(1,4);
n_ri=zeros(1,4);
b=b-1
for i=1:1:ndivr
    for j=1:1:b
        li(1,:)=n_fmi(j,1:3)-n_ai(j,1:3);
        lm(1,:)=n_fmm(j,1:3)-n_am(j,1:3);
        lo(1,:)=n_fmo(j,1:3)-n_ao(j,1:3);
        r=i/(ndivr+1);
        n_ri(j+((i-1)*b),1:3)=(li(1,:)*r)+n_ai(j,1:3);
        n_rm(j+((i-1)*b),1:3)=(lm(1,:)*r)+n_am(j,1:3);
        n_ro(j+((i-1)*b),1:3)=(lo(1,:)*r)+n_ao(j,1:3);
        n_ri(j+((i-1)*b),4)=n_ai(j,4);
        n_rm(j+((i-1)*b),4)=n_am(j,4);
        n_ro(j+((i-1)*b),4)=n_ao(j,4);
    end
end

%create brick elements
e=zeros(1,10);
n=zeros(1,3);
size_a=size(n_am);
size_fm=size(n_fmm);
size_r=size(n_rm);
total_size=size_a(1,1)+size_fm(1,1)+size_r(1,1);
x=1;

for j=0:1:ndivr+1
    for i=1:1:b
        if j==0 %first row of elements
            n(i,:)=n_ai(i,1:3);
            n(i+total_size,:)=n_am(i,1:3);
            n(i+(2*total_size),:)=n_ao(i,1:3);
        elseif j==ndivr+1
            n((j*b)+i,:)=n_fmi(i,1:3);
            n((j*b)+i+total_size,:)=n_fmm(i,1:3);
            n((j*b)+i+(2*total_size),:)=n_fmo(i,1:3);
        else %remaining rows of elements
            n((j*b)+i,:)=n_ri(i+((j-1)*b),1:3);
            n((j*b)+i+total_size,:)=n_rm(i+((j-1)*b),1:3);
            n((j*b)+i+(2*total_size),:)=n_ro(i+((j-1)*b),1:3);
        end
        x=x+1;
    end
end

size_elayer=(ndivr+1)*b;
size_nlayer=(ndivr+2)*b;
x=1;
for j=0:1:ndivr
    for i=1:1:b
        if j==0 %first row of elements
            e(x,2)=n_ai(i,4);                % leaflet id
            e(x+size_elayer,2)=n_am(i,4);
            x=x+1;
        else %remaining rows of elements
            e(x,2)=n_ri(i+((j-1)*b),4);      % leaflet id
```

```
            e(x+size_elayer,2)=n_rm(i+((j-1)*b),4);
            x=x+1;
        end

    end
end
x=1;
for j=0:1:ndivr
    for i=1:1:b
        if i==b
            %inner element layer
            e(x,1)=x;                           % element #
            e(x,3)=(j*b)+i;                     % node 1
            e(x,4)=(j*b)+1;                     % node 2
            e(x,5)=(j*b)+1+size_nlayer;         % node 3
            e(x,6)=(j*b)+i+size_nlayer;         % node 4
            e(x,7)=((j+1)*b)+i;                 % node 5
            e(x,8)=((j+1)*b)+1;                 % node 6
            e(x,9)=((j+1)*b)+1+size_nlayer;     % node 7
            e(x,10)=((j+1)*b)+i+size_nlayer;    % node 8
            % outer layer
            e(x+size_elayer,1)=x+size_elayer;                       % element #
            e(x+size_elayer,3)=(j*b)+i+size_nlayer;                   % node 1
            e(x+size_elayer,4)=(j*b)+1+size_nlayer;                   % node 2
            e(x+size_elayer,5)=(j*b)+1+size_nlayer+size_nlayer;       % node 3
            e(x+size_elayer,6)=(j*b)+i+size_nlayer+size_nlayer;       % node 4
            e(x+size_elayer,7)=((j+1)*b)+i+size_nlayer;               % node 5
            e(x+size_elayer,8)=((j+1)*b)+1+size_nlayer;               % node 6
            e(x+size_elayer,9)=((j+1)*b)+1+size_nlayer+size_nlayer;   % node 7
            e(x+size_elayer,10)=((j+1)*b)+i+size_nlayer+size_nlayer;  % node 8
            x=x+1;
            j;
        else
            %inner layer
            e(x,1)=x;                                                 % element #
            e(x,3)=(j*b)+i;                                           % node 1
            e(x,4)=(j*b)+(i+1);                                       % node 2
            e(x,5)=(j*b)+(i+1)+size_nlayer;                           % node 3
            e(x,6)=(j*b)+i+size_nlayer;                               % node 4
            e(x,7)=((j+1)*b)+i;                                       % node 5
            e(x,8)=((j+1)*b)+(i+1);                                   % node 6
            e(x,9)=((j+1)*b)+(i+1)+size_nlayer;                       % node 7
            e(x,10)=((j+1)*b)+i+size_nlayer;                          % node 8
            % outer layer
            e(x+size_elayer,1)=x+size_elayer;                         % element #
            e(x+size_elayer,3)=(j*b)+i+size_nlayer;                     % node 1
            e(x+size_elayer,4)=(j*b)+(i+1)+size_nlayer;                  % node 2
            e(x+size_elayer,5)=(j*b)+(i+1)+size_nlayer+size_nlayer;     % node 3
            e(x+size_elayer,6)=(j*b)+i+size_nlayer+size_nlayer;         % node 4
            e(x+size_elayer,7)=((j+1)*b)+i+size_nlayer;                 % node 5
            e(x+size_elayer,8)=((j+1)*b)+(i+1)+size_nlayer;             % node 6
            e(x+size_elayer,9)=((j+1)*b)+(i+1)+size_nlayer+size_nlayer;% node 7
            e(x+size_elayer,10)=((j+1)*b)+i+size_nlayer+size_nlayer;   % node 8
            x=x+1;
            j;

        end
    end
end
nodes=n;
%---------- END ---------------------------------------------------------------
%------------------------------------------------------------------------------
%---------- GENERATE CHORDAE TENDINEAE ----------------------------------------
```

```
%--- LENGTH OF PAPILLARY MUSCLE HEADS
length1=0;
length2=0;
% ANTERIOR PM
for i=1:1:(((sa(1,1)-1)*100)-1)
    l(1,:)=apm(i+1,:)-apm(i,:);
    length1=length1+norm(l);
end
% POSTERIOR PM
for i=1:1:(((sp(1,1)-1)*100)-1)
    l(1,:)=ppm(i+1,:)-ppm(i,:);
    length2=length2+norm(l);
end

%--- Number of chordae
nc=12;

%--- CREATE NODES ALONG APM AND PPM
apm_div=length1/nc;
ppm_div=length2/nc;
npm=zeros(nc*2,3);
a=1;
b=1;
length=0;
for i=1:1:nc
    if i==1
        npm(1,:)=apm(a,:);
        npm(nc+1,:)=ppm(a,:);
    elseif i==nc
        npm(nc,:)=apm((sa(1,1)-1)*100,:);
        npm(nc*2,:)=ppm((sp(1,1)-1)*100,:);
    else
        j=0;
        while j==0
            l(1,:)=apm(a+1,:)-apm(a,:);
            length=length+norm(l);
            if length==apm_div
                npm(i,:)=apm(a+1);
                diffl=0;
                length=0;
                a=a+1;
                j=1;
            elseif length<apm_div
                diffl=apm_div-length;
                k=a+1;
                a=a+1;
            elseif length>apm_div
                diffg=length-apm_div;
                if diffg>diffl
                    a=k;
                    npm(i,:)=apm(a,:);
                    diffl=0;
                    diffg=0;
                    length=0;
                    j=1;
                elseif diffg<diffl
                    a=a+1;
                    npm(i,:)=apm(a,:);
                    diffl=0;
                    diffg=0;
                    length=0;
                    j=1;
```

```
                end
            end
        end
        j=0;
        while j==0
            l(1,:)=ppm(b+1,:)-ppm(b,:);
            length=length+norm(l);
            if length==ppm_div
                npm(i+nc,:)=ppm(b+1);
                diffl=0;
                length=0;
                b=b+1;
                j=1;
            elseif length<ppm_div
                diffl=ppm_div-length;
                k=b+1;
                b=b+1;
            elseif length>ppm_div
                diffg=length-ppm_div;
                if diffg>diffl
                    b=k;
                    npm(i+nc,:)=ppm(b,:);
                    diffl=0;
                    diffg=0;
                    length=0;
                    j=1;
                elseif diffg<diffl
                    b=b+1;
                    npm(i+nc,:)=ppm(b,:);
                    diffl=0;
                    diffg=0;
                    length=0;
                    j=1;
                end
            end
        end
    end
end

%Find nodes along free margin
p=n_fmi(1,4);
j=0;
a(1,1)=0;
x=size(n_fmi);
x=x(1,1);

for i=2:1:x(1,1)
    nfmi=n_fmi(i,4);
    if n_fmi(i,4)>p || n_fmi(i,4)<p && a(1,1)==0
        a(j+1,1)=i;
        j=1;
        p=n_fmi(i,4);
    end
    if n_fmi(i,4)>p || n_fmi(i,4)<p && a(2,1)==0
         a(j+1,1)=i;
    end
end

s_apm=a(1,1);
s_ppm=a(2,1);
n_c=zeros(1,3);

for i=1:1:(nc*3)
```

```
    if (i+(s_apm-((nc*3/2)+1)))>x
        n_c(i,:)=n_fmm(i+((s_apm-((nc*3/2)+1)))-x,1:3);
    elseif (i+(s_apm-((nc*3/2)+1)))>0
        n_c(i,:)=n_fmm(i+(s_apm-((nc*3/2)+1)),1:3);
    elseif (i+(s_apm-((nc*3/2)+1)))<1
        n_c(i,:)=n_fmm(i+(s_apm-((nc*3/2)+1))+x,1:3);
    end
end
n_c2=zeros(1,3);
for i=1:1:(nc*3)
    if (i+(s_ppm-((nc*3/2)+1)))>x
        n_c2(i,:)=n_fmm(i+((s_ppm-((nc*3/2)+1)))-x,1:3);
    elseif (i+(s_ppm-((nc*3/2)+1)))>0
        n_c2(i,:)=n_fmm(i+(s_ppm-((nc*3/2)+1)),1:3);
    elseif (i+(s_ppm-((nc*3/2)+1)))<1
        n_c2(i,:)=n_fmm(i+(s_ppm-((nc*3/2)+1))+x,1:3);
    end
end
for i=1:1:(nc*3)
    n_c(i+(nc*3),:)=n_c2(i,:);
end

x=size(n);
for i=1:1:(nc*6)
    for j=1:1:x(1,1)
        if n_c(i,1:3)==n(j,:)
            n_c(i,4)=j;
        end
    end
end
n_c_split=zeros(nc*2,3);
j=1;

for i=1:3:(nc*6)
       l(1,:)=(n_c(i+1,1:3)-npm(j,1:3));
       n_c_split(j,:)=(l(1,:)*0.5)+npm(j,1:3);
       j=j+1;
end

n_leaflets=x(1,1);
for i=1:1:(nc*2)
    n(x(1,1)+i,:)=npm(i,:);
    n(x(1,1)+(nc*2)+i,:)=n_c_split(i,:);
end

%create beam elements
ec=zeros(nc*8,3);
for i=1:1:(nc*2)
    ec(i,1)=i;
    ec(i,2)=x(1,1)+i;
    ec(i,3)=x(1,1)+(nc*2)+i;
end
for i=1:1:(nc*6)
    ec(i+(nc*2),1)=i+(nc*2);
    ec(i+(nc*2),2)=n_c(i,4);
end
j=1;
for i=3:3:(nc*6)
    ec(i+(nc*2),3)=x(1,1)+(nc*2)+j;
    ec(i-1+(nc*2),3)=x(1,1)+(nc*2)+j;
    ec(i-2+(nc*2),3)=x(1,1)+(nc*2)+j;
    j=j+1;
end
```

```
%---------- END ---------------------------------------------------------------
%------------------------------------------------------------------------------
%---------- GENERATE LS-DYNA INPUT --------------------------------------------
part(1) = cellstr('PLeaflet');
part(2) = cellstr('ALeaflet');
part(3) = cellstr('PChordae');
part(4) = cellstr('AChordae');
date=datestr(now,'dd-mmm-yyyy HHMMSS');
savefile = ['LSDynaInput MVs1 ',date,'.dyn'];
fid = fopen(savefile, 'wt');
fprintf(fid, '$ Date : %s\n', datestr(clock));
fprintf(fid, '*KEYWORD\n');
fprintf(fid, '$---+----1----+----2----+----3----+----4----+----5----+----6----
+----7----+----8\n');
fprintf(fid, '$                     (1) TITLE CARD\n');
fprintf(fid, '$---+----1----+----2----+----3----+----4----+----5----+----6----
+----7----+----8\n');
fprintf(fid, '*TITLE\n');
fprintf(fid, 'MVs1\n');
fprintf(fid, '$---+----1----+----2----+----3----+----4----+----5----+----6----
+----7----+----8\n');
fprintf(fid, '$                     (2) CONTROL CARDS\n');
fprintf(fid, '$---+----1----+----2----+----3----+----4----+----5----+----6----
+----7----+----8\n');
fprintf(fid, '*CONTROL_TERMINATION\n');
fprintf(fid, '$   ENDTIM    ENDCYC     DTMIN    ENDNEG    ENDMAS\n');
fprintf(fid, ' 0.500E-01         0 0.000E+00 0.000E+00 0.000E+00\n');
fprintf(fid, '*CONTROL_TIMESTEP\n');
fprintf(fid, '$   DTINIT      SCFT      ISDO    TSLIMT      DTMS      LCTM
ERODE     MS1ST\n');
fprintf(fid, ' 0.000E+00 0.500E+00         0\n');
fprintf(fid, '*CONTROL_HOURGLASS\n');
fprintf(fid, '$      IHQ        QH\n');
fprintf(fid, '         1 0.100E+00\n');
fprintf(fid, '*CONTROL_BULK_VISCOSITY\n');
fprintf(fid, '$       Q2        Q1\n');
fprintf(fid, ' 0.150E+01 0.600E-01\n');
fprintf(fid, '*CONTROL_ENERGY\n');
fprintf(fid, '$     HGEN      RWEN    SLNTEN     RYLEN\n');
fprintf(fid, '         1         2         1         1\n');
fprintf(fid, '*CONTROL_OUTPUT\n');
fprintf(fid, '$    NPOPT    NEECHO    NREFUP    IACCOP     OPIFS    IPNINT
IKEDIT\n');
fprintf(fid, '         0         0         0         0 0.000E+00         0
0\n');
fprintf(fid, '$---+----1----+----2----+----3----+----4----+----5----+----6----
+----7----+----8\n');
fprintf(fid, '$                   (3) DATABASE CONTROL CARDS - ASCII HISTORY
FILE\n');
fprintf(fid, '$---+----1----+----2----+----3----+----4----+----5----+----6----
+----7----+----8\n');
fprintf(fid, '$*DATABASE_HISTORY_OPTION\n');
fprintf(fid, '$      ID1       ID2       ID3       ID4       ID5       ID6
ID7       ID8\n');
fprintf(fid, '$OPTION : BEAM    BEAM_SET   NODE   NODE_SET\n');
fprintf(fid, '$         SHELL   SHELL_SET  SOLID  SOLID_SET\n');
fprintf(fid, '$         TSHELL  TSHELL_SET\n');
fprintf(fid, '$---+----1----+----2----+----3----+----4----+----5----+----6----
+----7----+----8\n');
fprintf(fid, '$                     (4) DATABASE CONTROL CARDS FOR ASCII
FILE\n');
fprintf(fid, '$---+----1----+----2----+----3----+----4----+----5----+----6----
+----7----+----8\n');
```

```
fprintf(fid, '$*DATABASE_OPTION\n');
fprintf(fid, '$       DT\n');
fprintf(fid, '$OPTION : SECFORC RWFORC NODOUT ELOUT  GLSTAT\n');
fprintf(fid, '$         DEFORC  MATSUM NCFORC RCFORC DEFGEO\n');
fprintf(fid, '$         SPCFORC SWFORC ABSTAT NODFOR BNDOUT\n');
fprintf(fid, '$         RBDOUT  GCEOUT SLEOUT MPGS   SBTOUT\n');
fprintf(fid, '$         JNTFORC AVSFLT MOVIE\n');
fprintf(fid, '*DATABASE_GLSTAT\n');
fprintf(fid, ' 0.120E-03\n');
fprintf(fid, '*DATABASE_RCFORC\n');
fprintf(fid, ' 0.120E-03\n');
fprintf(fid, '$---+----1----+----2----+----3----+----4----+----5----+----6----
+----7----+----8\n');
fprintf(fid, '$                   (5) DATABASE CONTROL CARDS FOR BINARY
FILE\n');
fprintf(fid, '$---+----1----+----2----+----3----+----4----+----5----+----6----
+----7----+----8\n');
fprintf(fid, '*DATABASE_BINARY_D3PLOT\n');
fprintf(fid, '$  DT/CYCL      LCDT    NOBEAM\n');
fprintf(fid, ' 0.100E-02\n');
fprintf(fid, '*DATABASE_BINARY_D3THDT\n');
fprintf(fid, '$  DT/CYCL      LCDT    NOBEAM\n');
fprintf(fid, ' 0.100E-02\n');
fprintf(fid, '$*DATABASE_BINARY_OPTION\n');
fprintf(fid, '$  DT/CYCL      LCDT    NOBEAM\n');
fprintf(fid, '$OPTION : D3DRFL D3DUMP RUNRSF INTFOR\n');
fprintf(fid, '*DATABASE_EXTENT_BINARY\n');
fprintf(fid, '         0         0         3         0         1         1
1         1\n');
fprintf(fid, '         0         0         0         0         0         0\n');
fprintf(fid, '$---+----1----+----2----+----3----+----4----+----5----+----6----
+----7----+----8\n');
fprintf(fid, '$                     (6) DEFINE PARTS CARDS\n');
fprintf(fid, '$---+----1----+----2----+----3----+----4----+----5----+----6----
+----7----+----8\n');
for i = 1:4
   fprintf(fid, '*PART\n');
   fprintf(fid, '$ HEADING\n');
   fprintf(fid, ' PART PID =      %2i PART NAME : %s\n', i,char(part(i)));
   fprintf(fid, '$      PID       SID       MID     EOSID      HGID      GRAV
ADPOPT      TMID\n');
   fprintf(fid, '%10i %9i %9i\n', i,i,i);
end
fprintf(fid, '$---+----1----+----2----+----3----+----4----+----5----+----6----
+----7----+----8\n');
fprintf(fid, '$                     (7) MATERIAL CARDS\n');
fprintf(fid, '$---+----1----+----2----+----3----+----4----+----5----+----6----
+----7----+----8\n');
fprintf(fid, '*MAT_HEART_TISSUE\n');
fprintf(fid, '$MATERIAL NAME:PLeaflet    \n');
fprintf(fid, '$      MID        RO         C        B1        B2        B3
P\n');
fprintf(fid, '         1 0.100E-08 0.100E-02 0.151E+02 4.599E+00 0.100E+03
0.800E+04\n');
fprintf(fid, '$     AOPT\n');
fprintf(fid, '         0\n');
fprintf(fid, '$       XP        YP        ZP        A1        A2        A3\n');
fprintf(fid, '\n');
fprintf(fid, '$       V1        V2        V3        D1        D2        D3
BETA\n');
fprintf(fid, '\n');
fprintf(fid, '*MAT_HEART_TISSUE\n');
fprintf(fid, '$MATERIAL NAME:ALeaflet\n');
```

```
fprintf(fid, '$      MID        RO         C        B1        B2        B3
P\n');
fprintf(fid, '         2 0.100E-08 0.150E-02 38.831E+0 8.8941E+0 0.100E+03
0.950E+04\n');
fprintf(fid, '$     AOPT\n');
fprintf(fid, '         0\n');
fprintf(fid, '$       XP        YP        ZP        A1        A2        A3\n');
fprintf(fid, '\n');
fprintf(fid, '$       V1        V2        V3        D1        D2        D3
BETA\n');
fprintf(fid, '\n');
fprintf(fid, '*MAT_CABLE_DISCRETE_BEAM\n');
fprintf(fid, '$MATERIAL NAME:PChordae     \n');
fprintf(fid, '$      MID        RO         E      LCID       F0\n');
fprintf(fid, '         3 0.100E-08 173.3E+00\n');
fprintf(fid, '*MAT_CABLE_DISCRETE_BEAM\n');
fprintf(fid, '$MATERIAL NAME:AChordae     \n');
fprintf(fid, '$      MID        RO         E      LCID       F0\n');
fprintf(fid, '         4 0.100E-08 173.3E+00\n');
fprintf(fid, '$---+----1----+----2----+----3----+----4----+----5----+----6----
+----7----+----8\n');
fprintf(fid, '$                     (7.1) SECTION CARDS\n');
fprintf(fid, '$---+----1----+----2----+----3----+----4----+----5----+----6----
+----7----+----8\n');
fprintf(fid, '*SECTION_SOLID\n');
fprintf(fid, '$    SECID    ELFORM       AET\n');
fprintf(fid, '         1         1\n');
fprintf(fid, '*SECTION_SOLID\n');
fprintf(fid, '$    SECID    ELFORM       AET\n');
fprintf(fid, '         2         1\n');
fprintf(fid, '*SECTION_BEAM\n');
fprintf(fid, '$    SECID    ELFORM      SHRF   QR/IRID       CST     SCOOR
NSM\n');
fprintf(fid, '         3         6\n');
fprintf(fid, '$      VOL      INER       CID        CA    OFFSET\n');
fprintf(fid, ' 0.342E+02 0.640E+00         0 1.951E+00        -5\n');
fprintf(fid, '*SECTION_BEAM\n');
fprintf(fid, '$    SECID    ELFORM      SHRF   QR/IRID       CST     SCOOR
NSM\n');
fprintf(fid, '         4         6\n');
fprintf(fid, '$      VOL      INER       CID        CA    OFFSET\n');
fprintf(fid, ' 0.342E+02 0.640E+00         0 1.951E+00       -10\n');
fprintf(fid, '$---+----1----+----2----+----3----+----4----+----5----+----6----
+----7----+----8\n');
fprintf(fid, '$                    (8) NODAL POINT CARDS\n');
fprintf(fid, '$---+----1----+----2----+----3----+----4----+----5----+----6----
+----7----+----8\n');
fprintf(fid, '*NODE\n');
fprintf(fid, '$   NODE              X               Y               Z      TC
RC\n');
size_n=size(n);
for i = 1:size_n(1,1)
    fprintf(fid, '%8i %15.9f %15.9f %15.9f\n',i,n(i,1),n(i,2),n(i,3));
end
fprintf(fid, '$---+----1----+----2----+----3----+----4----+----5----+----6----
+----7----+----8\n');
fprintf(fid, '$                    (10) BEAM ELEMENT CARDS\n');
fprintf(fid, '$---+----1----+----2----+----3----+----4----+----5----+----6----
+----7----+----8\n');
fprintf(fid, '*ELEMENT_BEAM\n');
fprintf(fid, '$    EID     PID      N1      N2      N3\n');
size_ec=size(ec);
for i = 1:1:size_ec(1,1)
```

```
    fprintf(fid, '%8i %7i %7i %7i\n',ec(i,1),3,ec(i,2),ec(i,3));
end
fprintf(fid, '$---+----1----+----2----+----3----+----4----+----5----+----6----
+----7----+----8\n');
fprintf(fid, '$                    (12) SOLID ELEMENT CARDS\n');
fprintf(fid, '$---+----1----+----2----+----3----+----4----+----5----+----6----
+----7----+----8\n');
fprintf(fid, '*ELEMENT_SOLID\n');
fprintf(fid, '$    EID     PID\n');
fprintf(fid, '$     N1      N2      N3      N4      N5      N6      N7
N8\n');
size_e=size(e);
for i = 1:size_e(1,1)
    fprintf(fid, '%8i %7i\n %7i %7i %7i %7i %7i %7i %7i
%7i\n',e(i,1),e(i,2),e(i,3),e(i,4),e(i,5),e(i,6),e(i,7),e(i,8),e(i,9),e(i,10));
end
fprintf(fid, '*LOAD_SEGMENT\n');
fprintf(fid, '$     LCID        SF        AT        N1        N2        N3
N4\n');
for i = 1:size_elayer
    fprintf(fid, '%10i %9.1i %9.1i %9i %9i %9i
%9i\n',1,1,0,e(i,3),e(i,4),e(i,8),e(i,7));
end
fprintf(fid, '$---+----1----+----2----+----3----+----4----+----5----+----6----
+----7----+----8\n');
fprintf(fid, '$                    (16) BOUNDARY CONDITION CARDS\n');
fprintf(fid, '$---+----1----+----2----+----3----+----4----+----5----+----6----
+----7----+----8\n');
fprintf(fid, '*BOUNDARY_PRESCRIBED_MOTION_NODE\n');
fprintf(fid, '$      NID       DOF       VAD      LCID        SF       VID
DEATH     BIRTH\n');
size_ai=size(n_ai);
for i = 1:size_ai(1,1)
    fprintf(fid, '%10i %9i %9i %9i %9f %9i\n',i,-4,2,2,0.100E+01,i);
end
for i = 1201:(size_ai(1,1)+1200)
    fprintf(fid, '%10i %9i %9i %9i %9f %9i\n',i,-4,2,2,0.100E+01,i-1200);
end
for i = 2401:(size_ai(1,1)+2400)
    fprintf(fid, '%10i %9i %9i %9i %9f %9i\n',i,-4,2,2,0.100E+01,i-2400);
end
%Define radial vectors for each node of the annulus.
fprintf(fid, '*DEFINE_VECTOR\n');
fprintf(fid, '$      VID        XT        YT        ZT        XH        YH
ZH\n');
for i = 1:size_ai(1,1)
    fprintf(fid, '%10i %9.4f %9.4f %9.4f %9.4f %9.4f
%9.4f\n',i,n(i,1),n(i,2),n(i,3), 0.0, 0.0,n(i,3));
end
%Define annulus displacements
fprintf(fid, '*DEFINE_CURVE\n');
fprintf(fid, '$     LCID      SIDR      SCLA      SCLO      OFFA      OFFO\n');
fprintf(fid, '%10i %9i\n',2,0);
fprintf(fid, '$                  A1                  O1\n');
fprintf(fid, '       .000000000E+00      0.00000000E+00\n');
fprintf(fid, '       .270000007E-02      0.00000000E+00\n');
fprintf(fid, '       .199999996E-01      0.17500000E+01\n');
fprintf(fid, '       .368999988E-01      0.00000000E+00\n');
fprintf(fid, '       .500000007E-01      0.00000000E+00\n');
fprintf(fid, '*DEFINE_CURVE\n');
fprintf(fid, '$     LCID      SIDR      SCLA      SCLO      OFFA      OFFO\n');
fprintf(fid, '%10i %9i\n',1,0);
fprintf(fid, '$                  A1                  O1\n');
```

```
fprintf(fid, '      .000000000E+00      -.00000000E+00\n');
fprintf(fid, '      .500000024E-03      -.66499997E-04\n');
fprintf(fid, '      .130000000E-02      -.00000000E+00\n');
fprintf(fid, '      .270000007E-02      0.11969999E-03\n');
fprintf(fid, '      .439999998E-02      0.12236000E-02\n');
fprintf(fid, '      .620000018E-02      0.60913996E-02\n');
fprintf(fid, '      .800000038E-02      0.10600099E-01\n');
fprintf(fid, '      .980000012E-02      0.13100500E-01\n');
fprintf(fid, '      .147000002E-01      0.15228499E-01\n');
fprintf(fid, '      .199999996E-01      0.16079700E-01\n');
fprintf(fid, '      .256999992E-01      0.15228499E-01\n');
fprintf(fid, '      .302000009E-01      0.13526100E-01\n');
fprintf(fid, '      .315999985E-01      0.11145400E-01\n');
fprintf(fid, '      .368999988E-01      -.30590000E-03\n');
fprintf(fid, '      .399999991E-01      -.35910000E-03\n');
fprintf(fid, '      .430999994E-01      -.66499997E-04\n');
fprintf(fid, '      .500000007E-01      -.66499997E-04\n');
fprintf(fid, '*BOUNDARY_PRESCRIBED_MOTION_NODE\n');
fprintf(fid, '$      NID       DOF       VAD      LCID        SF       VID
DEATH     BIRTH\n');
for i=3601:1:3624
fprintf(fid, '%10i %9i %9i %9i %9f %9i\n',i,-4,2,77,0.100E+01,76);
end
fprintf(fid, '*DEFINE_VECTOR\n');
fprintf(fid, '$      VID        XT        YT        ZT        XH        YH
ZH\n');
fprintf(fid, '%10i %9f %9f %9f %9f %9f %9f\n',76,0,0,0,0,0,-1);
fprintf(fid, '*DEFINE_CURVE\n');
fprintf(fid, '$     LCID      SIDR      SCLA      SCLO      OFFA      OFFO\n');
fprintf(fid, '%10i %9i\n',77,0);
fprintf(fid, '$                A1                  O1\n');
fprintf(fid, '                  0                   0\n');
fprintf(fid, '               0.01                   0\n');
fprintf(fid, '               0.03                   8\n');
fprintf(fid, '               0.05                   0\n');
fprintf(fid, '*SET_PART_LIST\n');
fprintf(fid, '         1\n');
fprintf(fid, '         1         2\n');
fprintf(fid, '*CONTACT_AUTOMATIC_GENERAL\n');
fprintf(fid, '         1         0         2\n');
fprintf(fid, ' 0.000E+00 0.000E+00 0.000E+00 0.000E+00 0.200E+02         0
0.000E+00 0.100E+21\n');
fprintf(fid, '\n*END\n');
%---------- END ------------------------------------------------------------
```

A.2.2 Main Geometric Data Import Program

This program is a subroutine of the geometric reconstruction program. It imports the data outputs of the image processing program into MATLAB for the geometric reconstruction.

```
function x = importdata

global a fm ap pp
a=zeros(36,3);
fm=zeros(36,3);
ap=zeros(18,3);
pp=zeros(18,3);
scale=0.146;

for i=1:18
```

```
    if i==1
        readfile='DATA\000.txt';
    elseif i>1 && i<11
        readfile=['DATA\0',num2str(10*(i-1)),'.txt'];
    else
        readfile=['DATA\',num2str(10*(i-1)),'.txt'];
    end;
fid = fopen(readfile, 'r');
c = textscan(fid, '%*s %*s %*s %*s %f');
a(i,1) = c{1}(1);   % theta
a(i,2) = scale*c{1}(3);   % r
a(i,3) = scale*c{1}(4);   % z
a(i+18,1) = c{1}(9);
a(i+18,2) = scale*c{1}(11);
a(i+18,3) = scale*c{1}(12);
fm(i,1) = c{1}(5);
fm(i,2) = scale*c{1}(7);
fm(i,3) = scale*c{1}(8);
fm(i+18,1) = c{1}(13);
fm(i+18,2) = scale*c{1}(15);
fm(i+18,3) = scale*c{1}(16);
ap(i,1) = c{1}(17);
ap(i,2) = scale*c{1}(19);
ap(i,3) = scale*c{1}(20);
pp(i,1) = c{1}(21);
pp(i,2) = scale*c{1}(23);
pp(i,3) = scale*c{1}(24);
fclose(fid);
end;

%convert annulus coordinates to cartesian system
for i=0:17
a(i+1,1)=a(i+1,2)*cos((i*10)*pi()/180);
a(i+1,2)=a(i+1,2)*sin((i*10)*pi()/180);
end;
for i=18:35
a(i+1,1)=a(i+1,2)*cos(((i-18)*10)*pi()/180);
a(i+1,2)=a(i+1,2)*sin(((i-18)*10)*pi()/180);
end;

%convert free margin coordinates to cartesian system
for i=0:17
fm(i+1,1)=fm(i+1,2)*cos((i*10)*pi()/180);
fm(i+1,2)=fm(i+1,2)*sin((i*10)*pi()/180);
end;
for i=18:35
fm(i+1,1)=fm(i+1,2)*cos(((i-18)*10)*pi()/180);
fm(i+1,2)=fm(i+1,2)*sin(((i-18)*10)*pi()/180);
end;

%convert apm coordinates to cartesian system
for i=0:17
ap(i+1,1)=ap(i+1,2)*cos((i*10)*pi()/180);
ap(i+1,2)=ap(i+1,2)*sin((i*10)*pi()/180);
end;

%convert ppm coordinates to cartesian system
for i=0:17
pp(i+1,1)=pp(i+1,2)*cos((i*10)*pi()/180);
pp(i+1,2)=pp(i+1,2)*sin((i*10)*pi()/180);
end;
x=0;
```

A.2.3 Cubic Cardinal Spline Function

This program is a subroutine of the geometric reconstruction program. It applies the cubic cardinal spline to a set of input data, the annulus and free margin geometric data.

```
function c = spline(p,n,cn)

c=zeros(cn,3);
h=0.9;
for i=1:1:n
for t=0:1:99
    if i==1
        j1=n;
        j2=1;
        j3=2;
        j4=3;
    elseif i==n-1
        j1=n-2;
        j2=n-1;
        j3=n;
        j4=1;
    elseif i==n
        j1=n-1;
        j2=n;
        j3=1;
        j4=2;
    else
        j1=i-1;
        j2=i;
        j3=i+1;
        j4=i+2;
    end
    if i==1
    x=t+1;
    t=t/100;
    c(x,1)=((-h*t^3)+(2*h*t^2)-h*t)*p(j1,1)+(((2-h)*t^3)+((h-
3)*t^2)+1)*p(j2,1)+(((h-2)*t^3)+((3-(2*h))*t^2)+(h*t))*p(j3,1)+((h*t^3)-
(h*t^2))*p(j4,1);
    c(x,2)=((-h*t^3)+(2*h*t^2)-h*t)*p(j1,2)+(((2-h)*t^3)+((h-
3)*t^2)+1)*p(j2,2)+(((h-2)*t^3)+((3-(2*h))*t^2)+(h*t))*p(j3,2)+((h*t^3)-
(h*t^2))*p(j4,2);
    c(x,3)=((-h*t^3)+(2*h*t^2)-h*t)*p(j1,3)+(((2-h)*t^3)+((h-
3)*t^2)+1)*p(j2,3)+(((h-2)*t^3)+((3-(2*h))*t^2)+(h*t))*p(j3,3)+((h*t^3)-
(h*t^2))*p(j4,3);
    else
    x=t+1+(i-1)*100;
    t=t/100;
    c(x,1)=((-h*t^3)+(2*h*t^2)-h*t)*p(j1,1)+(((2-h)*t^3)+((h-
3)*t^2)+1)*p(j2,1)+(((h-2)*t^3)+((3-(2*h))*t^2)+(h*t))*p(j3,1)+((h*t^3)-
(h*t^2))*p(j4,1);
    c(x,2)=((-h*t^3)+(2*h*t^2)-h*t)*p(j1,2)+(((2-h)*t^3)+((h-
3)*t^2)+1)*p(j2,2)+(((h-2)*t^3)+((3-(2*h))*t^2)+(h*t))*p(j3,2)+((h*t^3)-
(h*t^2))*p(j4,2);
    c(x,3)=((-h*t^3)+(2*h*t^2)-h*t)*p(j1,3)+(((2-h)*t^3)+((h-
3)*t^2)+1)*p(j2,3)+(((h-2)*t^3)+((3-(2*h))*t^2)+(h*t))*p(j3,3)+((h*t^3)-
(h*t^2))*p(j4,3);
    end
end
end
```

A.2.4 Data Smoothing Function

This program is a subroutine of the geometric reconstruction program. It is used to smooth the geometric data in the reconstruction process.

```
function s = smooth(x,h,n,sn)
%x=input data
%h=moving average size
%n=number of points in x
%sn=number of points in s
raw=zeros(sn,3);
for i=1:1:sn
    raw(i,:)=x(i*(n/sn),:);
end
s=zeros(sn,3);

for i=h+1:1:sn-h
 totalx=0;
 totaly=0;
 totalz=0;
 for j=i-h:1:i+h
  totalx=totalx+raw(j,1);
  totaly=totaly+raw(j,2);
  totalz=totalz+raw(j,3);
 end
 s(i,1)=totalx/(2*h+1);
 s(i,2)=totaly/(2*h+1);
 s(i,3)=totalz/(2*h+1);
end

for i=sn-h+1:1:sn
 dif=h-(sn-i);
 totalx=0;
 totaly=0;
 totalz=0;
 for j=1:1:dif
  totalx=totalx+raw(j,1);
  totaly=totaly+raw(j,2);
  totalz=totalz+raw(j,3);
 end
 for j=i-h:1:i+h-dif
  totalx=totalx+raw(j,1);
  totaly=totaly+raw(j,2);
  totalz=totalz+raw(j,3);
 end
 s(i,1)=totalx/(2*h+1);
 s(i,2)=totaly/(2*h+1);
 s(i,3)=totalz/(2*h+1);
end

for i=1:1:h
 dif=h-i+1;
 totalx=0;
 totaly=0;
 totalz=0;
 for j=1:1:dif
  totalx=totalx+raw(sn-j+1,1);
  totaly=totaly+raw(sn-j+1,2);
  totalz=totalz+raw(sn-j+1,3);
 end
 for j=i-(h-dif):1:h+i
```

```
  totalx=totalx+raw(j,1);
  totaly=totaly+raw(j,2);
  totalz=totalz+raw(j,3);
 end
 s(i,1)=totalx/(2*h+1);
 s(i,2)=totaly/(2*h+1);
 s(i,3)=totalz/(2*h+1);
end
```

A.2.5 Papillary Muscle Head Spline Function

This program is a subroutine of the geometric reconstruction program. It applies the cubic cardinal spline to the papillary muscle head geometric data.

```
function c = pm_spline(p,n,cn)
% p = input data
% n = number of data points in p
% cn = number of data points in spline
global p1 p4
c=zeros(cn,3);
h=0.5;
for i=1:1:n-1
    if i==1
        j1=0;
        j2=1;
        j3=2;
        j4=3;
        l(1,:)=p(1,1:3)-p(2,1:3);
        p1(1,1:3)=(l(1,:)*1.1)+p(2,1:3);
    elseif i==n-1
        j1=n-2;
        j2=n-1;
        j3=n;
        j4=0;
        l(1,:)=p(n,1:3)-p(n-1,1:3);
        p4(1,1:3)=(l(1,:)*1.1)+p(n-1,1:3);
    else
        j1=i-1;
        j2=i;
        j3=i+1;
        j4=i+2;
    end
    for t=0:1:99
        if i==1
            x=t+1;
            t=t/100;
            c(x,1)=((-h*t^3)+(2*h*t^2)-h*t)*p1(1,1)+(((2-h)*t^3)+((h-
3)*t^2)+1)*p(j2,1)+(((h-2)*t^3)+((3-(2*h))*t^2)+(h*t))*p(j3,1)+((h*t^3)-
(h*t^2))*p(j4,1);
            c(x,2)=((-h*t^3)+(2*h*t^2)-h*t)*p1(1,2)+(((2-h)*t^3)+((h-
3)*t^2)+1)*p(j2,2)+(((h-2)*t^3)+((3-(2*h))*t^2)+(h*t))*p(j3,2)+((h*t^3)-
(h*t^2))*p(j4,2);
            c(x,3)=((-h*t^3)+(2*h*t^2)-h*t)*p1(1,3)+(((2-h)*t^3)+((h-
3)*t^2)+1)*p(j2,3)+(((h-2)*t^3)+((3-(2*h))*t^2)+(h*t))*p(j3,3)+((h*t^3)-
(h*t^2))*p(j4,3);
        elseif i==n-1
            x=t+1+(i-1)*100;
            t=t/100;
            c(x,1)=((-h*t^3)+(2*h*t^2)-h*t)*p(j1,1)+(((2-h)*t^3)+((h-
3)*t^2)+1)*p(j2,1)+(((h-2)*t^3)+((3-(2*h))*t^2)+(h*t))*p(j3,1)+((h*t^3)-
(h*t^2))*p4(1,1);
```

```
            c(x,2)=((-h*t^3)+(2*h*t^2)-h*t)*p(j1,2)+(((2-h)*t^3)+((h-
3)*t^2)+1)*p(j2,2)+(((h-2)*t^3)+((3-(2*h))*t^2)+(h*t))*p(j3,2)+((h*t^3)-
(h*t^2))*p4(1,2);
            c(x,3)=((-h*t^3)+(2*h*t^2)-h*t)*p(j1,3)+(((2-h)*t^3)+((h-
3)*t^2)+1)*p(j2,3)+(((h-2)*t^3)+((3-(2*h))*t^2)+(h*t))*p(j3,3)+((h*t^3)-
(h*t^2))*p4(1,3);
        else
            x=t+1+(i-1)*100;
            t=t/100;
            c(x,1)=((-h*t^3)+(2*h*t^2)-h*t)*p(j1,1)+(((2-h)*t^3)+((h-
3)*t^2)+1)*p(j2,1)+(((h-2)*t^3)+((3-(2*h))*t^2)+(h*t))*p(j3,1)+((h*t^3)-
(h*t^2))*p(j4,1);
            c(x,2)=((-h*t^3)+(2*h*t^2)-h*t)*p(j1,2)+(((2-h)*t^3)+((h-
3)*t^2)+1)*p(j2,2)+(((h-2)*t^3)+((3-(2*h))*t^2)+(h*t))*p(j3,2)+((h*t^3)-
(h*t^2))*p(j4,2);
            c(x,3)=((-h*t^3)+(2*h*t^2)-h*t)*p(j1,3)+(((2-h)*t^3)+((h-
3)*t^2)+1)*p(j2,3)+(((h-2)*t^3)+((3-(2*h))*t^2)+(h*t))*p(j3,3)+((h*t^3)-
(h*t^2))*p(j4,3);
        end
    end
end
```

A.3 Material Constant Optimization

A.3.1 Main Program

This program is used to determine the optimal material constants to fit the Guccione material model to the experimental data of May-Newman *et al.*

```
% The Guccione material constants are determined using the LSQNONLIN
% function.
% method. Data from May-Newman and Yin.
clc
clear % clears all variables
format long
load data.dat; % loads the experimental data file for the anterior leaflet

global sig11exp sig22exp E11exp E22exp sig11t sig22t Psig11exp Psig22exp
PE11exp PE22exp Psig11t Psig22t
       % declares constants shared with other m-files

sig11exp=data(:,1); % experimental circumferential Cauchy stress (Nmm-2)
sig22exp=data(:,3); % experimental radial Cauchy stress (Nmm-2)
E11exp=data(:,2); % experimental circumferential Green strain
E22exp=data(:,4); % experimental radial Green strain

options=optimset('largescale','on','MaxFunEvals',1e100,'tolFun',...
    1e-10,'TolX',1e-30,'MaxIter',5e3); % turns on
% Levenberg-Marquardt method of solution
iniconstants=[0.015 0.1 0.1]; % initial guesses for material constants
lb=[0.0015; 0.1; 0.1];
ub=[10; 20000; 20000];
[Constants]=lsqnonlin(@errSC,iniconstants,lb,ub,options)
%[Constants]=lsqnonlin(@errSC,iniconstants,[],[],options)
% the optimizer calls the @errSC m-file

Asig11exp=sig11exp;
```

```
Asig11t=sig11t;
Asig22exp=sig22exp;
Asig22t=sig22t;
AE11exp=E11exp;
AE22exp=E22exp;

load Pdata.dat; % loads the experimental data file for the posterior leaflet
       % declares constants shared with other m-files
Psig11exp=Pdata(:,1); % experimental circumferential Cauchy stress (Nmm-2)
Psig22exp=Pdata(:,3); % experimental radial Cauchy stress (Nmm-2)
PE11exp=Pdata(:,2); % experimental circumferential Green strain
PE22exp=Pdata(:,4); % experimental radial Green strain

options=optimset('largescale','on','MaxFunEvals',1e100,'tolFun',...
    1e-10,'TolX',1e-30,'MaxIter',5e3); % turns on
% Levenberg-Marquardt method of solution
iniconstants=[0.01 0.1 0.1]; % initial guesses for material constants
lb=[0.001; 0.1; 0.1];
ub=[10; 20000; 20000];
[Constants2]=lsqnonlin(@PerrSC,iniconstants,lb,ub,options)

% the optimizer calls the @errSC m-file


a(:,1)=Asig11exp-mean(Asig11exp);
a(:,2)=Asig22exp-mean(Asig22exp);
b(:,1)=Asig11t-mean(Asig11t);
b(:,2)=Asig22t-mean(Asig22t);
sum1=zeros(1,4);
sum2=zeros(1,4);
sum3=zeros(1,4);
for i=1:16
    for j=1:2
        sum1(j)=sum1(j)+a(i,j)*b(i,j);
        sum2(j)=sum2(j)+a(i,j)*a(i,j);
        sum3(j)=sum3(j)+b(i,j)*b(i,j);
    end
end
RA=[sum1(1)/(sqrt(sum2(1))*sqrt(sum3(1))),...
    sum1(2)/(sqrt(sum2(2))*sqrt(sum3(2)))]

a(:,1)=Psig11exp-mean(Psig11exp);
a(:,2)=Psig22exp-mean(Psig22exp);
b(:,1)=Psig11t-mean(Psig11t);
b(:,2)=Psig22t-mean(Psig22t);
sum1=zeros(1,4);
sum2=zeros(1,4);
sum3=zeros(1,4);
for i=1:16
    for j=1:2
        sum1(j)=sum1(j)+a(i,j)*b(i,j);
        sum2(j)=sum2(j)+a(i,j)*a(i,j);
        sum3(j)=sum3(j)+b(i,j)*b(i,j);
    end
end
RP=[sum1(1)/(sqrt(sum2(1))*sqrt(sum3(1))),...
    sum1(2)/(sqrt(sum2(2))*sqrt(sum3(2)))]
```

A.3.2 Optimizer Program

This program is a subroutine of the material constant optimization main program. It calculates the Cauchy stresses for the given experimental Green strains based on the constants c1, c2, and c3. The optimization algorithm finds the constants that minimize the error output.

```
function error=errSC(C)

global sig11exp sig22exp E11exp E22exp sig11t sig22t
c1=C(1);
c2=C(2);
c3=C(3);

E11=E11exp;
E22=E22exp;

delta=(1+2.*E11).*(1+2.*E22);
q=c2.*E11.^2+c3.*(E22.^2+(0.5.*(1./delta-1)).^2);
dW11=2.*c2.*E11-c3.*(1./delta-1)./(delta.*(1+2.*E11));
dW11=0.5.*c1.*dW11.*exp(q);
dW22=2.*c3.*E22-c3.*(1./delta-1)./(delta.*(1+2.*E22));
dW22=0.5.*c1.*dW22.*exp(q);

sig11t=(2.*E11+1).*dW11; % theoretical s11
sig22t=(2.*E22+1).*dW22; % theoretical s22
errs11=(sig11t-sig11exp);
errs22=(sig22t-sig22exp);
error=[errs11;errs22]; % combines errs11 and errs22 into one vector
```

B Leaflet Bulging and Coaptation Length Data

Table 6 – Leaflet Bulging and Coaptation Length Data

	MVs1	MVp1	MVp1-DO	MVp1-DO-A	MVp1-PC	MVp1-PC-A	MVp1-QR	MVp1-QR-A
Annulus Length [mm]	25.24	19.75	19.68	16.39	19.964	16.87	19.259	16.696
Annulus Length [pixels]	742.04	619.45	599.52	433.45	575.45	604.83	485.58	437.43
Scale Factor	0.0340	0.0319	0.0328	0.0378	0.0347	0.0279	0.0397	0.0382
Anterior Bulge [pixels]	77.16	30.15	79.4	85.48	61.29	103.59	7.07	33.24
Posterior Bulge [pixels]	51.16	23.09	42.19	27.17	65.38	71.45	34.23	26.31
Coaptation Length [pixels]	179.3	29.5	185.3	219.5	132.6	223.4	22.2	85.5
Anterior Bulge [mm]	2.6	0.96	2.61	3.23	2.13	2.9	0.3	1.3
Posterior Bulge [mm]	1.7	0.7	1.4	1.0	2.3	2.0	1.4	1.0
Coaptation Length [mm]	6.1	0.9	6.1	8.3	4.6	6.2	0.9	3.3